AN INTERFACIAL AREA TRANSPORT MODELING FOR TWO-PHASE FLOW IN SMALL AND LARGE CIRCULAR PIPES

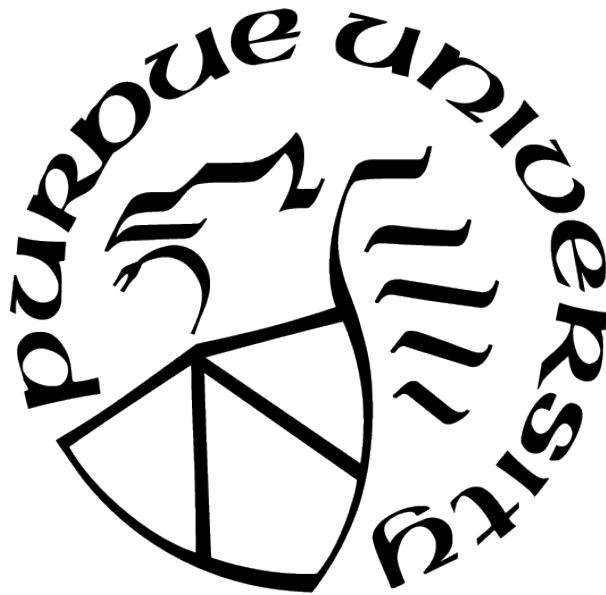by

Zhuoran Dang

A Dissertation

Submitted to the Faculty of Purdue University

In Partial Fulfillment of the Requirements for the degree of

Doctor of Philosophy

School of Nuclear Engineering

West Lafayette, Indiana

August 2021

THE PURDUE UNIVERSITY GRADUATE SCHOOL
STATEMENT OF COMMITTEE APPROVAL

Dr. Mamoru Ishii, Chair

School of Nuclear Engineering

Dr. Seungjin Kim

School of Nuclear Engineering

Dr. Martin Lopez-De-Bertodano

School of Nuclear Engineering

Dr. Steven T. Wereley

School of Mechanical Engineering

Approved by:

Dr. Seungjin Kim

To my family.

ACKNOWLEDGMENTS

TABLE OF CONTENTS

7

LIST OF TABLES

LIST OF FIGURES

9

NOMENCLATURE

Latin

a	transition function relaxation parameter
A	surface area; matrix of probe geometry
A_p	leading bubble projected area
a_i	interfacial area concentration, IAC
C	adjustable coefficient
C_D	drag coefficient
D_b	bubble diameter
D_c	maximum distorted bubble diameter
D_{cap}	cap bubble diameter
$D_{d,max}$	maximum stable bubble diameter
D_{dp}	departure diameter
D_h	flow channel hydraulic diameter
D_m	bubble motion cross-sectional diameter
D_{re}	critical bubble diameter determined by Reynolds number
D_{sm}	Sauter mean diameter
D_{slug}	slug bubble diameter
D_{tr}	critical bubble diameter determined from geometry
F	Force
f	particle distribution function; friction factor
f_d	departure frequency
f_{os}	bubble oscillation frequency
g	gravitational acceleration
h	height
j	superficial velocity
Ja	Jacob number
j	superficial velocity
La	Laplace length scale

L	length
L_w	wake region length
L_w^*	dimensionless wake region length
M_{ig}, M_{if}	generalized interfacial momentum term
n	number density
$\boldsymbol{n}_i$	interfacial unit normal vector
N	number of bubbles
N_n	active nucleation site density
P, p	pressure
p_c	probability of bubble in inertia-controlled region
q	heat flux
Q	volumetric flow rate
r	radial position
R	pipe inner radius
Re	Reynolds number
Sr	Strouhal number
t	time
T	transition function
u_t	turbulent fluctuation velocity
u_r	relative velocity
$\bar{u}_{rw}$	average relative velocity between leading and trailing bubble
v	bubble velocity
V_b	bubble volume
V_{we}	wake volume
We	Weber number
z/D_h	length to diameter ratio

Greek

α	void fraction
β	relaxation parameter; dimensionless bubble boundary diameter

χ	intergroup expansion/contraction transfer coefficient
η_j	void fraction source/sink rate due to the jth-type particle interaction mechanism; direction angle of probe sensors
Γ_g	mass generation rate of gas phase
λ	flow channel area factor
μ	kinematic viscosity
ψ	bubble shape factor
φ	interaction rate
ε	turbulent kinetic energy dissipation rate
ρ	density
σ	surface tension
θ_b	inclination angle
θ_w	cap or slug wake angle

Subscripts

atm	atmospheric
b	bubble
$body$	slug body
cap	cap bubble
cr	critical value
e	equivalent
eff	effective
1	Group-1
2	Group-2
f	liquid phase
g	gas phase
k	index of phase
exp	experiment
m	mixture
$model$	model

0	atmospheric
head	slug head
slug, sl	slug bubble
WE	wake entrainment
SO	shearing-off

Mathematical symbols

$\langle \ \rangle$	area-averaged quantity
$\langle\langle \ \rangle\rangle$	void fraction weighted-mean quantity

ABSTRACT

With the rapid development of the advanced two-phase flow experimental technologies, more experimental databases with extended measurement ranges have been established to support the two-phase flow model development. The advantage of the Two Fluid model in modeling the complex two-phase flow phenomena over the mixture models stands out. One key aspect in the Two Fluid model development is the accurate modeling of the interfacial area between phases, which is strongly related to the interfacial mass, momentum, and energy transfer. As a closure relation of interfacial area concentration (interfacial area per unit volume) for the Two Fluid model, the Interfacial Area Transport Equation (IATE) provides dynamic predictions on the interfacial area change. It substantially solves the shortcoming of using flow-regime-dependent empirical correlations that can introduce numerical discontinuities between flow regimes.

The IATE has been extensively developed over the past twenty-five years. Many studies targeted on improving its prediction capability by developing bubble interaction source terms based on their experimental data. The existing models are usually based on medium and large flow channels, yet the models may not be physically fit the small flow channels. The major reason is that the wall effect can have a larger influence on the two-phase flow in a small flow channel, as the surface area to volume ratio greatly increases. Therefore, the primary objectives of this study are to physically investigate the wall effect on two-phase flow and develop a generalized IATE by extending the application range of existing IATE from large and medium flow channels to small flow channel.

To achieve the objective, this study established a rigorous database of air-water two-phase flows in a small diameter pipe with its inner diameter of 12.7 mm, focusing on the bubbly-to-slug transition regime. The experimental analysis was performed on the pipe wall effect on the interfacial characteristics, based on the current experimental database and the existing experimental database collected on vertical pipes of different sizes. It is observed that 1) the pipe wall effect can alter the non-uniform radial two-phase distribution; 2) the bubbly-to-slug flow regime transition in a small diameter pipe happens in a smaller void fraction than in a large diameter pipe; 3) the bubble coalescence phenomenon can be more dominant for

small pipe flow, and an intensive intergroup transfer can happen for the two-group interfacial area transport in two-phase flows. As the interfacial area transport is directly related to the two-phase geometrical configuration, the two-phase geometrical parameters, void fraction and relative bubble size, are identified as the key parameters for modeling.

In the modeling of IATE source terms, the high geometrical scalability of the model is realized by properly including the wall effect into the modeling consideration. The following major improvements on the existing models are: 1) the inertia subrange assumption on the turbulent-driven interaction is properly improved; 2) the bubble-induced turbulent-driven interactions such as wake entrainment is revised by considering the wall effect on the wake region. In summary, models of bubble interaction due to random collision, wake entrainment, turbulent impact, and shearing-off are revised based on the existing studies on the IATE source terms development. The newly proposed interfacial area transport models are evaluated against an experimental database with 112 test conditions in total from a wide range of experimental pipe diameters from 12.7 mm to 304.8 mm. The new models can accurately capture the drastic intergroup transfer of void fraction and interfacial area concentration between two groups in transition flows. Overall, the relative error of void fraction and interfacial area concentration comparing with the experimental data are within $\pm 15\%$ and $\pm 10\%$, respectively.

1. INTRODUCTION

1.1 Research Background

Multi-phase flow phenomena can exist in many modern industrial systems, such as nuclear reactors. The analysis of the two-phase flow problem is essential to system safety and design optimization. To meet the rapidly increasing industrial system capability, the analysis and accurate modeling of the multi-phase flows are of considerable importance. On the other hand, an accurate prediction for the behaviors of the two-phase flows is challenging because the two-phase flows are complex and are developing dynamically. Besides, two-phase flows are strongly geometrical-related, thus, it can be difficult to use universal models to describe its behaviors. In the development of two-phase flow models, there are two fundamentally different formulations of macroscopic field equations for two-phase flow systems [1], the mixture model and the two-fluid model. The mixture model is formulated by considering the two-phase flow as a whole unit, while considers the relative motions between the phases. The accuracy of this model is largely based on the degree of phase mixing. Therefore, the mixture model is not suitable for separated two-phase flows such as annular flow. The two-fluid model considers each phase separately by formulating the balance of mass, momentum, and energy equation using separate governing equations. At the same time, the phase interactions are described using interfacial transfer terms included in the governing equations. Compared with the mixture model, the two-fluid model has a higher development ceiling and potential, as it includes more constitutive relations and models describing the two-phase flow behaviors. This is a two-sided coin that unless these constitutive models, especially the interfacial transfer terms, are properly modeled, the advantage of the two-fluid model over the mixture model is not realized. The success of a two-fluid model requires more supports from experimental observations. Fortunately, with the advancement of the experimental techniques, the experimental capability is increasing over the past decades and experimental data with a broad range are now available.

The interfacial transfer between phases is critically important and largely affects the two-fluid model performance. The interfacial transfer terms are strongly related to interfacial area concentration, which is defined as the amount of interfacial area per unit mixture

volume. Successful modeling of the interfacial transfer requires a complete understanding of the two-phase interfacial structure and interfacial area change. One typical method to estimate the interfacial area concentration is to use flow-regime-dependent empirical correlations formulated based on experimental data. With static experimental correlations and flow regime maps, large prediction errors and oscillations caused by using multiple correlations for continuously changing flow may exist. In this sense, a transport model that can predict the dynamic behaviors of the interfacial structure is necessary. Based on this understanding, the interfacial area transport equation (IATE) was developed [2]. It can predict the change of two-phase flow structure dynamically and mechanistically, which essentially improves the accuracy and robustness of the predictions.

Previous researches have successfully developed the foundation of the IATE (Kocamustafaogullari and Ishii, 1995 [2]; Wu, 1998 [3]; Kim, 1999 [4]; Hibiki, 2000 [5]; Sun, 2004 [6]; Smith, 2002 [7]; Fu, 2003b [8]) and the experimental techniques needed for the measurement of interfacial area, bubble diameters and velocities (Kataoaka, 1986 [9]; Ishii and Revankar, 1992 [10]; Kim, 2000 [11]). In the model development of the interfacial area source terms, for adiabatic air-water conditions, an extensive database was generated for various geometries and experimental range (Fu, 2003a[8]; Smith, 2002 [7]; Revankar, 1992 [10]; Hibiki, 1999 [5]; Goda, 2002[12]). Using this database, mechanistic models for the source (bubble disintegration) and sink (bubble coalescence) of interfacial area were developed that can be applied to the bubbly, slug, and churn turbulent flows (Wu, 1998 [3]; Fu, 2003b [8]; Sun, 2004 [6]; Ishii, 2004 [13]; Hibiki, 2000 [5]; Smith, 2002 [7]; Worosz, 2015 [14]). For boiling steam-water conditions, the available database is much smaller. Ozar (2009) [15] performed experiment in an vertical annulus geometry and developed the two-group IATE framework with phase change included. With all these studies on the development of IATE, both the foundation of IATE and the methodologies for further development of IATE constitutive models have been established.

1.2 Importance of the Problem

The most important part in the modeling of two-phase flow is to determine the interface between phases in the temporal and spacial domains. The interface is where the mass, momentum, and energy transfers between phases happen, thus, the prediction to it directly determines the accuracy of the modeling of the two-phase flow. Meanwhile, interfacial modeling can be complex because it is continuously moving. It is impossible to to formulate the two-phase flow problem with multiple boundaries with their position unknown [1]. Therefore, two-phase flow problem in the macroscopic scale usually involves in averaging methods and proper approximations. For example, the modeling of interfacial structure can be modeled using empirical or semi-empirical correlations based on the flow regimes. These correlations are usually developed based on experimental databases with various flow conditions and flow channel geometries. In this sense, the accuracy of these correlations are strongly related to the experimental data range and geometries. What may also be important to know that for different flow regime, the correlations used can be different. Since the flow regime is determined in a subjective manner, and the boundaries, namely flow regime transitions, are quite ambiguous, it leads to large uncertainties and artificial discontinuities when using multiple correlations in a continuously changing two-phase flow systems. Therefore, a continuous model without relying on flow regimes that can dynamically predict the change of two-phase flows is of vital importance. The Interfacial Area Transport Equation (IATE) [2] is a satisfying solution to this problem. It has been well proved that the IATE can give good predictions from dispersed two-phase flows in vertical medium and large pipes.[3], [13], [14], [16] However, the constitutive models in the existing IATE requires improvements in small diameter pipe flows. In this sense, more rigorous experimental data with various flow conditions and channel geometries is required as support for the IATE modeling.

1.3 Literature Survey

1.3.1 Theoretical Background and Model Development

The Two-fluid model includes six field equations that treat each phase separately in terms of mass, momentum, and energy (Vernier and Delhaye, 1968 [17]; Ishii, 1975 [18]; Ishii and Mishima, 1984 [19]). The field equations are given as,

$$\frac{\partial (\alpha_k \rho_k)}{\partial t} + \nabla \cdot (\alpha_k \rho_k \vec{v}_k) = \Gamma_k \tag{1.1}$$

$$\frac{\partial \alpha_k \rho_k \vec{v}_k}{\partial t} + \nabla \cdot (\rho_k \alpha_k \vec{v}_k \vec{v}_k) = -\alpha_k \nabla p_k + \nabla \cdot \alpha_k \left(\overline{\tau} + \tau_k^t \right) + \alpha_k \rho_k \vec{g}$$
$$+ \vec{v}_{ki} \Gamma_k + \vec{M}_{ik} - \nabla \alpha_k \cdot \tau_i \tag{1.2}$$

$$\frac{\partial \alpha_k \rho_k i_k}{\partial t} + \nabla \cdot (\rho_k \alpha_k \vec{v}_k h_k) = -\nabla \cdot \alpha_k \left(\overline{q} + q_k^T \right) + \alpha_k \frac{D_k p_k}{Dt} + i_{ki} \Gamma_k + a_i q_{ik}'' + \phi_k \tag{1.3}$$

where the subscript k denotes the phases index. α, ρ, $\vec{v}$, $\vec{g}$, τ, τ^t, $\vec{i}$, $\overline{q}$. q^T, and ϕ are void fraction, density, velocity, pressure, gravitational constant, viscous stress, turbulent stress, internal energy, averaged heat flux, and turbulent heat flux, respectively. Γ, $\vec{M}_i$, and q_{ik}'' are the terms related to the interfacial mass, momentum, and energy transfer: mass generation, generalized interfacial drag, and interfacial heat flux, respectively. The jump conditions for the interfacial transfers were given as (Ishii 1975),

$$\begin{aligned} \Gamma_g + \Gamma_f &= 0 \\ \vec{M}_{ig} + \vec{M}_{if} &= 0 \\ \left(a_i q_{gi}'' + \Gamma_g i_g \right) + \left(a_i q_{fi}'' + \Gamma_{ff} \right) &= 0 \end{aligned} \tag{1.4}$$

The interfacial area concentration is defined the amount of interfacial area per unit mixture volume, expressed as (Ishii, 1975),

$$a_i = \frac{1}{L_s} = \frac{\text{interfacial area}}{\text{unit mixture volume}} \tag{1.5}$$

20

where L_s is the length scale for the interface. From Ishii and Chawla (1979), the interfacial transfer due to standard drag was given as

$$\frac{\alpha \vec{F}_g}{B_g} = -a_i \left[\frac{C_D}{4} \left(\frac{r_{sm}}{r_d} \right) \frac{\rho_f \vec{v}_r |\vec{v}_r|}{2} \right] \tag{1.6}$$

where C_D, $\vec{v}_r$, r_{sm}, r_d are drag coefficient, relative velocity, Sauter mean radius, and bubble drag radius, respectively. It can be seen from the equation that the interfacial transfer terms in the equations is proportional to the product of interfacial area concentration, a_i, and the corresponding driving force. Ishii and Mishima [19] expressed the relation between the interfacial transfer terms and the interfacial area concentration as follows,

$$Interfacial\ transfer\ terms \sim a_i \times Driving\ potential \tag{1.7}$$

From the above relation, an accurate prediction of interfacial area concentration is important for the interfacial transfer terms as well as the two-phase flow modeling. As discussed in the previous section, the state-of-art method for interfacial area concentration modeling is to use the Interfacial Area Transport Equation.

1.3.2 Interfacial Area Transport Equation

The formulation of interfacial area transport equation is developed analogous to the Boltzman transport equation. [2] The state of fluid particles in a continuous medium is described using particle number density distribution function, $f(V, \vec{x}, \vec{v}, t)$. The function states that the particle with a volume V, is moving with a velocity of $\vec{v}$ at a given time t and spatial position s. Similar to the Boltzmann transport equation, the particle movement is described using the following equation [13],

$$f(V + \delta V, \vec{x} + \vec{v}\delta t, \vec{v} + \vec{F}\delta t, t + \delta t)\delta\mu - f(V, \vec{x}, \vec{v}, t)\delta\mu$$
$$= \left[\sum_j S_j + S_{ph} \right] \delta\mu\delta t \tag{1.8}$$

where $\delta\mu$, $\delta t, \vec{F}$ are the volume element in μ space and a time range, the force applied per unit mass,respectively. S_j and S_{ph} are the particle source rates per unit mixture due to the j-th particle interactions and particle source rates for phase change, respectively. The LHS of Eq.1.8 can be expanded with a Taylor series in δt, and the following form is obtained,

$$\frac{\partial f}{\partial t} + \nabla \cdot (f\vec{v}) + \frac{\partial}{\partial V}\left(f\frac{dV}{dt}\right) = \sum_j S_j + S_{ph} \tag{1.9}$$

Kocamustafaogullari and Ishii [2] followed this approach and derived the interfacial area and void fraction transport equation and its closure relations,

$$\frac{\partial \alpha \rho_g}{\partial t} + \nabla \cdot \alpha \rho_g \vec{v}_g = \Gamma_g \tag{1.10}$$

$$\frac{\partial a_i}{\partial t} + \nabla \cdot a_i \vec{v}_i = \sum_j \phi_j + \phi_{ph} \tag{1.11}$$

where $\vec{v}_i$ is the interfacial velocity, ϕ_j is the rate of change of the interfacial area concentration due to the particle interactions, ϕ_{ph} is the rate of change of interfacial area concentration due to the phase change, and Γ is the amount of phase change per unit volume of the mixture.

The one-group interfacial area transport equation was further derived by Wu et al. [3], Kim [4] and Hibiki and Ishii [20], expressed as,

$$\begin{aligned}\frac{\partial a_i}{\partial t} + \nabla \cdot (a_i \vec{v}_i) = \frac{2}{3}\left(\frac{a_i}{\alpha}\right)\left(\frac{\partial \alpha}{\partial t} + \nabla \cdot (\alpha \vec{v}_g) - \eta_{ph}\right) \\ + \sum_j \phi_j + \phi_{ph}\end{aligned} \tag{1.12}$$

where ϕ_j, ϕ_{ph} are the rate of change of interfacial area concentration due to j-th bubble interaction, and the rate of change of interfacial area concentration due to phase change, respectively. This equation is only applicable for bubbly flow systems that the bubbles are considered to be in spherical or elliptical shape. As bubble size becomes large, the bubble shape cannot sustain spherical, and become distorted. The size and shape differences of the bubble lead to different drag and interaction behaviours. Therefore, small and large bubbles should be separately modeled. Specifically, Hibiki and Ishii [16], Smith [7], Fu and Ishii [8],

Ishii et al. [13] and Sun et al.[6] developed two-group IATEs that separately formulated the small spherical bubbles and large distorted bubbles,

$$\frac{\partial a_{i1}}{\partial t} + \nabla \cdot (a_{i1}\vec{v}_{i1}) = \left[\frac{2}{3} - \chi^2\right] \left(\frac{a_{i1}}{\alpha_1}\right) \left[\frac{\partial \alpha_1}{\partial t} + \nabla \cdot (\alpha_1 \vec{v}_{g_1}) - \eta_{ph1}\right]$$
$$+ \sum_j \phi_{j1} + \phi_{ph1} \tag{1.13}$$

$$\frac{\partial a_{i2}}{\partial t} + \nabla \cdot (a_{i2}\vec{v}_{i2}) = \frac{2}{3}\left(\frac{a_{i2}}{\alpha_2}\right) \left[\frac{\partial \alpha_2}{\partial t} + \nabla \cdot (\alpha_2 \hat{v}_{g2}) - \eta_{ph2}\right]$$
$$+ \chi^2\left(\frac{a_{i1}}{\alpha_1}\right) \left[\frac{\partial \alpha_1}{\partial t} + \nabla \cdot (\alpha_1 \vec{v}_{g_1}) - \eta_{ph1}\right] + \sum_j \phi_{j2} + \phi_{ph2} \tag{1.14}$$

where the subscripts 1 and 2 denote the group-1 spherical bubble and group-2 large distorted bubble (cap, slug, and churn bubbles). χ is the inter-group transfer coefficient due to expansion, compression, and/or phase change at the group boundary (Ishii et al, [13]; Sun et al. [21]). It is defined as,

$$\chi = \frac{f_c V_c}{\int_{V_{\min}}^{V_c} f \mathrm{d}V} = \frac{f_c V_c}{n_1} \tag{1.15}$$

where n_1, f_c and V_c are the bubble number density for group-1 bubbles, bubble number density distribution, and bubble volume at the group boundary between two groups, respectively.

In the two-group interfacial area transport equation, the boundary of the two group bubbles is defined using a critical bubble size/diameter,

$$D_c = 4\sqrt{\frac{\sigma}{g\Delta\rho}} \quad for \ round \ pipes \tag{1.16}$$

$$D_c = 1.7 G^{1/3} \left(\frac{\sigma}{g\Delta\rho}\right)^{1/3} \quad for \ rectangular \ channels \tag{1.17}$$

where G is the length of the short side of the rectangular channel.

From the general formulation of IATEs, bubble interactions and phase change source terms are not explicitly formulated in terms of the experimental measurements, such as pressure drop and velocities. Rather, the bubble interaction modeling should physically

consider the bubble dynamics. Therefore, the major developing effort for the IATE is to develop source terms of the bubble interactions and phase change. The modelings of these mechanisms mentioned are discussed below.

1.3.3 Modeling of Bubble Interactions

In the existing IATE models, the bubble interaction phenomena consist of bubble coalescence and bubble disintegration. These two phenomena are further divided into several sub-categories, which are summarized as

- coalescence of bubbles due to random collision, driven by the turbulent fluctuation in the liquid phase.

- bubbles accelerate driven by the turbulent wake formed by the preceding bubbles and coalesce with the preceding bubbles.

- disintegration of bubbles due to the impact of turbulent eddy in liquid phase

- disintegration of large, irregular shape bubbles that small bubbles are sheared off from the rim of the large bubbles.

- disintegration of large bubbles due to the surface instability

Based on the review by Besagni et al. [22], the existing models of bubble interaction phenomena are generally developed following two approaches. One approach is to empirically model the interaction rate by fitting selected functions in terms of related parameters using experimental data. Similar to other experimental-based empirical correlations, these models are highly dependent on the experiments including the configuration and test conditions. With the increasing number of engineering systems design, these existing empirical correlations may not be able to apply to the new systems that can have different geometrical configurations or a broader range of operating conditions. [22] Another approach to consider the interaction rate is to separately model the interaction frequency and the interaction efficiency, which allows the modeling to be more physical-based. This approach was used in many studies on the bubble interaction model development, including those

for IATE development. For the IATE bubble interaction source terms, the model development for one-group and two-group IATE differs in terms of the bubble shape and size, as well as the intergroup transfer phenomenon. Table 1.1 summarizes the currently available bubble interaction models for one-group interfacial area transport equations. Table 1.2 to 1.4 summarize the currently available bubble interaction models for one-group interfacial area transport equations, developed by Fu and Ishii [8], Smith [7], and Sun [6], respectively. These models are for different experimental configurations, but they provide good references to other similar studies on model development for other flow configurations.

1.3.4   Modeling of Phase Change

The effect of phase change on the interfacial area concentration and void fraction should be considered in a heated two-phase flow system. The phase change effects on interfacial area transport occur along with the hydrodynamic effects discussed above. In the macroscopic two-phase flow, the mechanisms due to phase change are summarized as follows,

- wall nucleation that new vapor generated in form of small spherical bubbles due to super-heated surfaces

- flashing in the super-heated bulk liquid and significant amount of vapor is generated

- bulk evaporation that vapor bubbles grow through evaporation in the super-heated bulk fluid

- bulk condensation that vapor bubbles shrink and collapse in the sub-cooled bulk liquid.

The consideration of each mechanism is highly related to the flow condition. For example, in a sub-cooled boiling steam-water flow, the effect of wall nucleation and bulk condensation should be more significant than that of flashing and bulk evaporation.

Kocamustafaogullari and Ishii [23] proposed a wall nucleation bubble number source term along with the bubble number density transport equation. Sun [6] further stated that the wall nucleation in the interfacial area transport equation can be modeled as,

$$\phi_{WN} = \pi N_n f_{dp} D_{dp}^2 \xi_h / A_c \qquad (1.18)$$

where D_{dp}, N_n, and f_{dp} are the bubble departure diameter, active nucleation site density, and the bubble departure frequency, respectively. Many studies were performed on these parameters and many empirical and semi-empirical correlations were developed. Some of the models are summarized in Table 1.5.

Park et al. [24] developed models for the interfacial area change due to the bulk condensation. The mechanism of the bulk condensation due to the interfacial heat transfer can be explained in the two aspects: bubble shrinking or thermal-controlled region ϕ_{PC}, and bubble collapsing or inertia-controlled region ϕ_{CO}. The change of bubble size due to bubble shrinking is governed by the interfacial heat transfer between the phases, while bubble collapsing is strongly related to pressure force. From the experimental observation, one of these two phenomena can be dominant over the others in certain states, and Park et al. consider the condensing bubble size can be the key parameter. The collapsing of small bubbles is generally caused by inertia-driven condensation, while the shrinking of large bubbles is due to the interfacial heat transfer. In this sense, the dominance of the two mechanisms can be regarded as two regions with the bubble size as the metric. To separate these two regions in a two-phase flow system, the fraction/probability of the bubbles in the system that belongs to one of the two regions (e.g. inertia-controlled region) is defined,

$$p_c = probability\,(D < D_b) \tag{1.19}$$

where p_c is the fraction of the bubbles in the system that belong to the inertia-controlled region. D_b is the bubble diameter at the region boundary, which is calculated based on force balance and Clausius-Clapeyron approximation,

$$D_b = \frac{4\sigma}{P_f} \cdot \left(e^{\frac{i_{fg}}{R} \cdot \frac{T_g - T_f}{T_g T_f}} - 1 \right)^{-1} \tag{1.20}$$

where T_g, T_f, and R are steam temperature, liquid temperature, and gas constant, respectively.

The ϕ_{PC} and ϕ_{CO} are modeled by considering the residence time that bubbles remain in either thermal-controlled region or inertia-controlled region. The two mechanisms are modeled as,

$$\phi_{PC} = -4\pi \cdot (1 - p_c) \cdot \psi \cdot \frac{a_i^3}{\alpha^2} \cdot Nu_c \cdot Ja \cdot \alpha_f \tag{1.21}$$

$$\phi_{CO} = R_{ph} \cdot \pi D_b^2 = -\pi D_b^2 \cdot \psi \cdot \frac{a_i^3}{\alpha^2} \cdot \frac{1}{t_c} \tag{1.22}$$

where Nu_c, Ja, α_f, ψ are condensation Nusselt number, Jacob number, fluid thermal diffusivity, and the bubble shape factor, respectively. t_c is the residence time of the bubbles that stay in the thermal-controlled region, calculated as,

$$t_c = \frac{D_{sm}^2 - D_b^2}{4} \frac{\rho_g i_{fg}}{Nu_c \cdot k_f \Delta T_{sub}} \tag{1.23}$$

p_c is the probability of bubbles in inertia-controlled region and is calculated as,

$$p_c = \frac{\Delta t_{c,in}}{\Delta t_{c,th} + \Delta t_{c,in}} = \frac{f(0) - f(\beta_b)}{f(0)} \tag{1.24}$$

where $\Delta t_{c,th}$ and $\Delta t_{c,in}$ are the residence time of bubbles in thermal-controlled region and inertia controlled region. β_b is the dimensionless bubble diameter at the boundary,

$$\beta_b = D_b/D_{sm} \tag{1.25}$$

β_b is treated as a constant and equal to 0.4 by Park et al. and the following studies who utilize this model. However, a recent study by Dang et al. [25] found that Eq. 1.25 may result in an artificial error when treating β_b as a constant, since it makes the ratio of ϕ_{PC} and ϕ_{CO} a constant. However, the dominance of the thermal-controlled or inertia-controlled condensation depends on the initial bubble size and the flow conditions, thus, the ratio of these two mechanisms should not be always a constant. Therefore, an alternative approach in determining the value of β_b is proposed by Dang et al. [25] that a dimensionless number B [26] is used.

1.3.5   Experimental Studies and Database

Due to the complexity of two-phase flows, the development of two-phase flow models relies on some extent of proper phenomenological strategy. The characteristic mechanisms of two-phase flow are usually analyzed based on reliable experimental databases. Over the past several decades, the advancements of the experimental analysis on two-phase flow are realized by the development of the experimental instrumentations such as the local multi-sensor conductivity probe [10], [11], the multi-sensor optical fiber probe [27], and the wire-mesh sensor [28]. With these measurement tools, high quality local two-phase flow parameters can be obtained, usually including the void fraction and interfacial area concentration (IAC). Specifically for the electrical and optical multi-sensor probe, the methodology of measuring IAC was proposed by Ishii [18],

$$a_i = \frac{1}{\Delta T} \sum_j \left(\frac{1}{|\vec{v}_i \cdot \vec{n}_i|} \right)_j \tag{1.26}$$

where $\vec{v}_i$ and $\vec{n}_i$ are the interfacial velocity and the normal direction to the interface, respectively. ΔT is the total elapsed measurement time, and j indicates the j-th bubble interface. Later on, Kataoka et al. [9] developed multi-sensor conductivity probe algorithms (two-senor and four-sensor) for IAC. The four-sensor probe can be regarded as consisting of three pairs of two-sensor probe in a three-dimensional arrangement. This allows the four-sensor probe to measure the interfacial velocity in three normal directions. The IAC can be calculated from the four-sensor probe measurement using the following expression,

$$a_i = \frac{1}{\Delta T} \sum_j \left(\frac{1}{|\vec{v}_i \cdot \vec{n}_i|} \right)_j = \frac{1}{\Delta T} \sum_j \frac{\sqrt{|A_{1j}|^2 + |A_{2j}|^2 + |A_{3j}|^2}}{|A_0|} \tag{1.27}$$

where A_0, A_{1j}, A_{2j}, and A_{3j} are the matrices formed based on the probe configuration, and they are given as

$$|A_{1j}| = \begin{vmatrix} 1/v_{j01} & \cos\eta_{y1} & \cos\eta_{z1} \\ 1/v_{j02} & \cos\eta_{y2} & \cos\eta_{z2} \\ 1/v_{j03} & \cos\eta_{y3} & \cos\eta_{z3} \end{vmatrix}$$

$$|A_{2j}| = \begin{vmatrix} \cos\eta_{x1} & 1/v_{j01} & \cos\eta_{z1} \\ \cos\eta_{x2} & 1/v_{j02} & \cos\eta_{z2} \\ \cos\eta_{x3} & 1/v_{j03} & \cos\eta_{z3} \end{vmatrix} \tag{1.28}$$

$$|A_{3j}| = \begin{vmatrix} \cos\eta_{x1} & \cos\eta_{y1} & 1/v_{j01} \\ \cos\eta_{x2} & \cos\eta_{y2} & 1/v_{j01} \\ \cos\eta_{x3} & \cos\eta_{y3} & 1/v_{j01} \end{vmatrix}$$

$$|A_0| = \begin{vmatrix} \cos\eta_{x1} & \cos\eta_{y1} & \cos\eta_{z1} \\ \cos\eta_{x2} & \cos\eta_{y2} & \cos\eta_{z2} \\ \cos\eta_{x3} & \cos\eta_{y3} & \cos\eta_{z3} \end{vmatrix}$$

where $\cos\eta_{ik}$ is the direction cosine along axis i from sensor 0 to sensor k, and v_{j0k} is the velocity of the j-th bubble surface moving from sensor 0 to sensor k. Other than the multi-sensor conductivity probe, wire-mesh sensor is also a popular measurement technique for two-phase interfacial structure. The detailed information of using wire-mesh sensor as an major instrumentation for interfacial area measurement can refer to a recent study by Dave [29].

Table 1.6 summarizes the experimental databases with detailed local interfacial profiles. These experimental databases generally consist of local time-averaged two-phase flow parameters including void fraction, interfacial area concentration, and bubble velocity obtained through conductivity probe measurements. Besides, the bubble Sauter mean diameter is obtained calculation in terms of void fraction and interfacial area concentration. Additional experimental studies and databases have been summarized in the review of Lin and Hibiki [30] for both adiabatic and heated flows.

Table 1.1. Summary of the interaction terms of the one-group IATE

Investigators	Interaction term	Model
Wu et al. (1998) and Kim (1999)	TI	$\phi_{TI} = \dfrac{C_{TI}\alpha^2\varepsilon^{1/3}}{D_b^{5/3}}\exp\left(-\dfrac{We_{cr}}{We}\right)\sqrt{1-\dfrac{We_{cr}}{We}}$
	RC	$\phi_{RC} = -\dfrac{C_{RC}\alpha^2\varepsilon^{1/3}}{D_b^{5/3}}\left(\dfrac{1}{\frac{1}{\alpha_{max}}\left(\frac{1}{\alpha_{max}-\alpha^{1/3}}\right)}\right)\left[1-\exp\left(-C_T\dfrac{\alpha_{max}^{1/3}\alpha^{1/3}}{\alpha_{max}^{1/3}-\alpha^{1/3}}\right)\right]$
	WE	$\phi_{WE} = -\dfrac{C_{WE}C_D^{1/3}\alpha^2 u_r}{D_b^2}$
Hibiki and Ishii (2000)	RC	$\phi_{RC} = -\dfrac{C_{RC}\alpha^2\varepsilon^{1/3}}{D_b^{5/3}}\left(\dfrac{1}{(\alpha_{max}-\alpha)}\right)\exp\left(-\dfrac{K_c\rho_f^{1/2}D_b^{5/6}\varepsilon^{1/3}}{\sigma^{1/2}}\right)$
	TI	$\phi_{II} = \dfrac{C_{TI}\alpha(1-\alpha)\varepsilon^{1/3}}{D_b^{5/3}(\alpha_{max}-\alpha)}\exp\left(-\dfrac{K_B\sigma}{\rho_f D_b^{5/3}\varepsilon^{2/3}}\right)$
Hibiki et al. (2001)	RC	$\phi_{RC} = -\dfrac{C_{RC}\alpha^2\varepsilon^{1/3}}{D_b^{5/3}}\left(\dfrac{1}{(\alpha_{max}-\alpha)}\right)\exp\left(-\dfrac{K_c\rho_f^{1/2}D_b^{5/6}\varepsilon^{1/3}}{\sigma^{1/2}}\right)$
	WE	$\phi_{WE} = -C_{WE}C_D^{1/3}a_i^2 u_r\exp\left(-\dfrac{K_c\rho_f^{1/2}D_b^{5/6}\varepsilon^{1/3}}{\sigma^{1/2}}\right)$

Table 1.2. Summary of the interaction terms of the two-group IATE by Fu and Ishii (2002)

Interaction term	Model
WE, 2+2→2	$$\phi_{WE}^{(2)} = -10.24 C_{WE2} D^{3/2} \alpha_2 \left[1 - \exp\left(\frac{-2331\alpha_2 V_s^{*2}}{D^5} \right) \right]$$ $$\times \left[\exp\left(\frac{0.06 C_l \left(\alpha_{2,\max}/\alpha_2 - 1 \right)}{V_s^*} \right) - 1 \right]^{-1}$$
WE, 1+2→2	$$\phi_{1,WE}^{(12,2)} = -C_{WE}^{(12,2)} \pi \left(\frac{2g\Delta\rho}{\rho_f} \right)^{1/2} D^{1/2} V_s^{*1/2} \frac{\alpha_1 \alpha_2}{1-\alpha_2} \kappa_{fr} \left(\frac{3}{D_{Sm,1}} \right)$$ $$\phi_{2,WE}^{(12,2)} = C_{WE}^{(12,2)} \pi \left(\frac{2g\Delta\rho}{\rho_f} \right)^{1/2} D^{1/2} V_s^{*1/2} \frac{\alpha_1 \alpha_2}{1-\alpha_2} \kappa_{fr} \left(\frac{2}{\alpha_m^{0.5} D} \right)$$
SO, 2→1+1	$$\left\langle \phi_{1,SO}^{(2,1)} \right\rangle = 0.5257 C_{SO} \alpha_2 v_g^{1/5} \left(\frac{\rho_f}{We_c \sigma D} \right)^{3/5} \left(\frac{2g\Delta\rho}{\rho_f} \right) V_s^{*-4/5} \xi_{SO} \left(1 - 0.667 \kappa_{bl} \right) \kappa_{fr}^2$$
SO, 2→2+1	$$\left\langle \phi_{2,SO}^{(2,1)} \right\rangle = -4.4332 C_{SO} \alpha_2 v_g^{1/5} D^{-9/5} \alpha_{2m}^{1/2} \left(\frac{2g\Delta\rho}{\rho_f} \right)^{2/5} V_s^{*-1/5} \left(1 - 0.66 \kappa_{bl} \right) \kappa_{fr}^{4/5}$$
SO, 2→2+1	$$\left\langle \phi_{2,SO}^{(2,1)} \right\rangle = -4.4332 C_{SO} \alpha_2 v_g^{1/5} D^{-9/5} \alpha_{2m}^{1/2} \left(\frac{2g\Delta\rho}{\rho_f} \right)^{2/5} V_s^{*-1/5} \left(1 - 0.66 \kappa_{bl} \right) \kappa_{fr}^{4/5}$$
TI, 1+1→2	$$\phi_{TI}^{(2)} = C_{TI}^{(2)} \frac{\alpha_2 \varepsilon^{1/3} V_s^*}{D} \left(\frac{1 - \alpha_1 - \alpha_2}{1 - \alpha_2} \right) \left[1 - \left(\frac{D_c}{\alpha_{2,\max}^{0.5} D} \right)^{5/3} \right]$$ $$\times \left[14.38 + 1.57 \alpha_{2,\max}^{-2/3} \left(D_c/D \right)^{4/3} - 15.95 \alpha_{2,\max}^{-1/6} \left(D_c/D \right)^{1/3} \right]$$
TI, 2+2→2	$$\phi_{TI}^{(1)} = C_{TI} \frac{1}{18} \left(\frac{\overline{u}_t' a_{i1}^2}{\alpha_1} \right) \left[1 - \frac{We_{cr}}{We^*} \right]^{1/2} \exp\left(-\frac{We_{cr}}{We^*} \right), We^* > We_{cr}$$
RC, 1+1→1 (Wu et al., 1998)	$$R_{RC}^{(1)} = C_{RC} \left[\frac{u_t n_1^2 D_{sm1}^2}{\alpha_{1,\max}^{1/3} \left(\alpha_{1,\max}^{1/3} - \alpha_1^{1/3} \right)} \right] \left[1 - \exp\left(-C \frac{\alpha_{1,\max}^{1/3} \alpha_1^{1/3}}{\alpha_{1,\max}^{1/3} - \alpha_1^{1/3}} \right) \right]$$ $$\left\langle \delta A_{i1}^{(11,1)} \right\rangle_R = D_{sm1}^2 \left[\begin{array}{c} -3.142 D_1^{*3} + 2.183 D_1^{*5} - 0.395 D_1^{*8} \\ +3.392 \left(0.579 D_1^{*3} - 1 \right)^{8/3} \end{array} \right]$$ $$\phi_{RC}^{(1)} = \left\langle \delta A_{i1}^{(11,1)} \right\rangle_R R_{RC}^{(1)}$$
RC, 1+1→2	$$\left\langle \delta A_{i1}^{(11,2)} \right\rangle_R = D_{sm1}^2 \left[8.82 + 2.035 \left(0.579 D_1^{*3} - 1 \right)^{8/3} - 5.428 D_1^{*3} \right]$$ $$\phi_{1,RC}^{(11,2)} = \left\langle \delta A_{i1}^{(11,2)} \right\rangle_R R_{RC}^{(1)}$$ $$\left\langle \delta A_{i2}^{(11,2)} \right\rangle_R = D_{Sm,1}^2 \left(6.462 - 2.182 D_1^{*5} + 0.395 D_1^{*8} \right)$$ $$\phi_{2,RC}^{(11,2)} = \left\langle \delta A_{i2}^{(11,2)} \right\rangle_R R_{RC}^{(1)}$$

Table 1.3. Summary of the interaction terms of the two-group IATE by Smith (2002)

Interaction term	Model
RC, 1+1→1	$\phi_{RC}^{(1)} = -0.17 C_{RC}^{(1)} \lambda_{RC}^{(1)} \dfrac{\varepsilon^{1/3} \alpha_1 a_{i,1}^{5/3}}{\alpha_{1,\max}^{1/3}\left(\alpha_{1,\max}^{1/3} - \alpha_1^{1/3}\right)} \left[1 - \exp\left(-C_{RC1} \dfrac{\alpha_{1,\max}^{1/3} \alpha_1^{1/3}}{\left(\alpha_{1,\max}^{1/3} - \alpha_1^{1/3}\right)}\right)\right]$
RC, 1+1→2	$\phi_{RC}^{(11,2)} = 4.1 C_{RC}^{(1)} \lambda_{RC}^{(1)} \dfrac{\varepsilon^{1/3} \alpha_1 a_{i,1}^{5/3}}{\alpha_{1,\max}^{2/3}} \left[1 - \exp\left(-C_{RC1} \dfrac{\alpha_{1,\max}^{1/3} \alpha_1^{1/3}}{\left(\alpha_{1,\max}^{1/3} \alpha_1^{1/3}\right)}\right)\right] \left(1 - \tfrac{2}{3} D_{c1}^*\right)$
RC, 1+2→2	$\phi_{RC,l1}^{(12,2)} = -1.14 C_{RC}^{(12,2)} \lambda_{RC}^{(12,2)} \varepsilon^{1/3} \alpha_1^{2/3} \alpha_2^{4/3} a_{i,1} a_{i,2}^{2/3}$ $\times \left[1 - \exp\left(-C_{RC1} \dfrac{\alpha_{1,\max}^{1/3} \alpha_1^{1/3}}{\left(\alpha_{1,\max}^{1/3} - \alpha_1^{1/3}\right)}\right)\right]$ $\phi_{RC,l1}^{(12,2)} = 1.80 C_{RC}^{(12,2)} \lambda_{RC}^{(12,2)} \varepsilon^{1/3} \alpha_1^{5/3} \alpha_2^{1/3} a_{i,1} a_{i,2}^{5/3}$ $\times \left[1 - \exp\left(-C_{RC1} \dfrac{\alpha_{1,\max}^{1/3} \alpha_1^{1/3}}{\left(\alpha_{1,\max}^{1/3} - \alpha_1^{1/3}\right)}\right)\right]$
RC, 2+2→2	$\phi_{RC}^{(2)} = -95.7 C_{RC}^{(2)} \lambda_{RC}^{(2)} \mathcal{E}^{1/3} \dfrac{1}{D_h^2} \dfrac{1}{a_{i,2}^{1/3}} \left[1 - \exp\left(-C_{RC2} \alpha_2^{1/2}\right)\right] \left(1 - 0.37 D_{c2}^{*3}\right)$
WE, 1+1→1	$\phi_{WE}^{(1)} = -0.17 C_{WE}^{(1)} C_{D1}^{1/3} u_{r,1} a_{i1}^2$
WE, 1+1→2	$\phi_{WE,2}^{(11,2)} = 2.57 C_{WE}^{(11,2)} C_{D1}^{13} u_{r,1} a_{i,1}^2 \left(1 - \tfrac{2}{3} D_{c1}^*\right)$
WE, 1+2→2	$\phi_{WE,l_1}^{(12,2)} = -0.33 C_{WE}^{(12,2)} \overline{u}_{w12} a_{i,1} a_{i,2}$
WE, 2+2→2	$\phi_{WE}^{(2)} = -1.02 C_{WE}^{(2)} \left[1 - \exp\left(-0.7 \alpha_2\right)\right] \overline{u}_{rw2} \dfrac{a_{i2}^2}{\alpha_2} \left(1 - 0.10 D_{c2}^{*2}\right)$
TI, 1→1	$\phi_{TI}^{(1)} = 0.12 C_{TI}^{(1)} \varepsilon^{1/3} \left(\dfrac{a_{i,1}^{5/3}}{\alpha_1^{2/3}}\right) (1 - \alpha) \exp\left(-\dfrac{We_{cr,1}}{We_1}\right) \sqrt{1 - \dfrac{We_{cr,1}}{We_1}}$
TI, 2→1	$\phi_{TI,g1}^{(2,1)} = 6.165 C_{TI}^{(2,1)} \varepsilon^{1/3} (1 - \alpha) \left(\dfrac{a_{i,2}^{5/3}}{\alpha_2^{2/3}}\right) \exp\left(-\dfrac{We_{cr,2}}{We_2}\right)$ $\times \sqrt{1 - \dfrac{We_{cr,2}}{We_2}} \left(0.212 D_{c2}^{*13/3} - 0.167 D_{c2}^{*5}\right)$
TI, 2→2	$\phi_{TI,g2}^{(2)} = 0.378 C_{TI}^{(2)} \varepsilon^{1/3} (1 - \alpha) \left(\dfrac{a_{i,2}^{5/3}}{\alpha_2^{2/3}}\right) \exp\left(-\dfrac{We_{cr,2}}{We_2}\right)$ $\times \sqrt{1 - \dfrac{We_{cr,2}}{We_2}} \left(1 - 0.212 D_{c2}^{*13/3}\right)$
SO, 2→1+2	$\phi_{SO,1}^{(2,12)} = 8.0 C_{SO} \dfrac{\rho_f^{3/5} u_{rb}^{1/5} \sigma^{2/5}}{\rho_g D_h^{2/5} We_c^{3/5}} \dfrac{a_{i,2}^2}{\alpha_2} \left[1 - \left(\dfrac{We_{c,SO}}{We_{m2}}\right)^4\right]$ $\phi_{SS,2}^{(2,12)} = -0.36 C_{so} \left(\dfrac{\sigma}{\rho_g v_{rb}}\right) \dfrac{a_{i,2}^3}{\alpha_2^2} \left[1 - \left(\dfrac{We_{c,so}}{We_{m2}}\right)\right]$
SI, 2→2	$\phi_{SI}^{(2)} = \left\{ \begin{array}{l} 2.616 \times 10^{-4} C_{RC}^{(2)} \varepsilon^{1/3} \dfrac{1}{D_h^2} \alpha_2^2 \left(\dfrac{\sigma}{g\Delta\rho}\right)^{1/6} \left[1 - \exp\left(-C_{RC2} \alpha_2^{1/2}\right)\right] + \\ 1.425 \times 10^{-7} C_{WE}^{(2)} P_{WE}^{(2)} \overline{u}_{m2} \alpha_2^2 \left(\dfrac{\sigma}{g\Delta\rho}\right)^{-1} \end{array} \right\}$

Table 1.4. Summary of the interaction terms of the two-group IATE by Sun et al. (2004a)

Interaction term	Model
RC, 1+1→1	$\phi_{RC}^{(1)} = -0.17 C_{RC}^{(1)} \dfrac{\varepsilon^{1/3}\alpha_1^{1/3}a_{i,1}^{5/3}}{\alpha_{1,\max}^{1/3}\left(\alpha_{1,\max}^{1/3}-\alpha_1^{1/3}\right)}\left[1-\exp\left(-C_{RC1}\dfrac{\alpha_{1,\max}^{1/3}\alpha_1^{1/3}}{\alpha_{1,\max}^{1/3}-\alpha_1^{1/3}}\right)\right]$
	$\alpha_{1,\max} = 0.62$
RC, 1+2→2	$\phi_{RC,1}^{(12,2)} = -4.85 C_{RC}^{(12,2)}\mathcal{E}^{1/3}\dfrac{a_{i,1}\alpha_1^{2/3}\alpha_2^2}{R_{m2}^{2/3}}\left[1-\exp\left(-C_{RC1}\dfrac{\alpha_{1,\max}^{1/3}\alpha_1^{1/3}}{\left(\alpha_{1,\max}^{1/3}-\alpha_1^{1/3}\right)}\right)\right]$
RC, 2+2→2	$\phi_{RC}^{(2)} = -13.6 C_{RC}^{(2)}\dfrac{\alpha_2^2\mathcal{E}^{1/3}}{W^2 G}R_{m2}^{4/3}\left(1-2.0R_c^{*2}+\dfrac{9.0G}{R_{m,2}}\right)$ $\left[1-\exp\left(-C_{RC2}\alpha_2^{1/2}\right)\right]$
WE, 1+1→1	$\phi_{WE}^{(1)} = -0.27 C_{WE}^{(1)}u_{r,1}C_{D,1}^{1/3}a_{i,1}^2$
WE, 1+2→2	$\phi_{WE,1}^{(12,2)} = -\displaystyle\int_{V_{\min}}^{V_{m1}}\left[\int_{V'+V_c}^{V'+V_{m2}}2.01\dfrac{C_{v2}\lambda_{WE}^{(12,2)}}{\sqrt{C_L}}f_1 f_2\sqrt{gC_{D2}}G\left(V-V'\right)^{1/2}\mathrm{d}V\right]\overline{A}_{i,1}\mathrm{d}V'$ $= -4.35 C_{WE}^{(12,2)}\sqrt{gC_{D2}}G\dfrac{a_{i,1}\alpha_2}{R_{m,2}}$
WE, 2+2→2	$\phi_{WE}^{(2)} = -15.9 C_{WE}^{(2)}\dfrac{\alpha_2^2}{R_{m,2}^2}\sqrt{C_D g}G\left(1+0.51R_c^*\right),\ \text{and}\ R_c^* = R_c/R_{m,2}, R_c = 0.85G^{1/3}(\sigma/g\Delta\rho)^{1/3}$
TI, 1→1	$\phi_{TI}^{(1)} = 0.12 C_{TI}^{(1)}\varepsilon^{1/3}(1-\alpha)\dfrac{a_{i,1}^{5/3}}{\alpha_1^{2/3}}\exp\left(-\dfrac{We_{c,TI1}}{We_1}\right)\sqrt{1-\dfrac{We_{c,T/1}}{We_1}}$
TI, 2→2	$\phi_{TI,2}^{(2)} = \phi_{TI,l}^{(2)} + \phi_{TI,g}^{(2)} \approx 1.4 C_{TI}^{(2)}\alpha_2\dfrac{\varepsilon^{1/3}G}{R_{m,2}^{8/3}}(1-\alpha)\left(1-2R_c^*\right)\exp\left(-\dfrac{We_{c,TI2}}{We_2}\right)\sqrt{1-\dfrac{We_{c,TI2}}{We_2}}$
SO, 2→2+1	$\phi_{SO,1}^{(2,12)} = R_{SO}^{(2,12)}\overline{A}_i\left(d_s\right) = 64.51 C_{SO}C_d^2\dfrac{\alpha_2 u_{rb}}{GR_{m,2}}\left(1-\left(\dfrac{We_{c,SO}}{We_{m2}}\right)^3\right)$

Table 1.5. Summary of the models for the wall nucleation

Work	Parameter	Model
Fritz (1935)	Departure diameter	$D_d = 0.0208\theta\sqrt{\frac{2\sigma}{g(\rho_l-\rho_g)}}$
Kocamustafaogullari and Ishii (1983)	Departure diameter	$D_d = 0.0012\left(\frac{\Delta\rho}{\rho_g}\right)^{0.9} D_{dF}$
Prodanovic et al. (2002)	Departure diameter	$D_d^+ = AJa^b\theta^c\left(\frac{\rho_l}{\rho_g}\right)^d Bo^\bullet$
Brooks et al. (2015)	Departure diameter	$D_d/\sqrt{\frac{\sigma}{g\Delta\rho}} = C_{Dd}Ja_T^a\rho^{*b}Bo^c\Pr_l^d$
Cole (1960)	Departure frequency	$f_d = \left(\frac{4g(\rho_l-\rho_g)}{3\rho_l C_D D_d}\right)^{0.5}$
Ivey (1967)	Departure frequency	$fD_d^2 = C$
Podowski et al. (1997)	Departure frequency	$t_W = \left[\frac{1}{2C_1}\left(-C_3 + \sqrt{C_3^2 - 4C_1C_2}\right)\right]^2$
Euh et al. (2010)	Departure frequency	$N_{f,Euh} = \frac{f_d D_d^2}{\alpha_l}$ $f_d = \frac{\alpha_i}{D_d^2}N_{f,Ehh}$ $N_{f,Euh} = 1.6N_{q_{NB,C}^{1.3}}$
Brooks (2014)	Departure frequency	$N_{f,Brooks} = \frac{f_d\rho_g h_{fg}D_d}{q''_{NB,L-W}} = 0.667N_A^{-0.117}$
Brooks and Hibiki (2015)	Departure frequency	$f_d^* = C_{fa}Ja_W^a\rho^{*b}Ja_T^c\Pr_{\text{sat}}^d$ $f_d^* = \frac{f_d D_d^2}{\alpha_i}$

Table 1.6. Available experimental databases for interfacial area transport model development

Investigators	Geometry	Flow Direction	Dimension(mm)
Hibiki and Ishii (1999)	Vertical round pipe	Upward	25.4
Fu(2001)	Vertical round pipe	Upward	48.3
Smith(2002)	Vertical round pipe	Upward	101.6, 152.4
Ishii (2004)	Vertical round pipe	Downward	25.4, 50.8
Bernard(2014)	Vertical round pipe	Upward	50.8
Schlegel et al. (2012, 2014)	Vertical round pipe	Upward	152.4, 203.2, 304.8
Worosz(2015)	Vertical round pipe	Upward	50.8
Dang et al. (2017)	Vertical round pipe	Upward	25.4
Wang et al. (2017)	Vertical round pipe	Downward	25.4
Wang et al. (2019)	Vertical round pipe	Upward	25.4
Talley (2012)	Horizontal round pipe	-	38.1
Kong (2018)	Horizontal round pipe	-	38.1, 101.6
Paranjape (2009)	Vertical 8x8 Rod Bundle	Upward	$D_{rod} = 12.7$ Pitch $= 16.7$ $D_{h,subchannel} = 15.3$
Yang (2015)	Vertical 8x8 Rod Bundle	Upward	$D_{rod} = 12.7$ Pitch $= 16.7$ $D_{h,subchannel} = 15.3$
Kim (1999)	Vertical Rectangular Duct	Upward	200×10
Sun (2001)	Vertical Rectangular Duct	Upward	200×10
Liu (2006)	Vertical Rectangular Duct	Upward	200×10
Zhu(2017)	Vertical Rectangular Duct	Upward	200×10
Ozar(2009)	Annulus	Upward	$D_{inner} : 19.1$ $D_{outer} : 38.1$

1.3.6 Required Advancement of Existing IATE Models

Towards finalizing the development of two-group IATE in the dispersed flow system, several efforts need to be made based on the existing IATE development achievements. Although many existing studies have contributed to the IATE development, they vary in both experimental configurations and modeling approaches. The performances of the models are quite different in terms of different experimental configurations. Specifically, the experimental observations are the basis of the modeling. Since the two-phase flows are strongly related to the flow channel geometry, the models based on different experimental configurations can vary either physically or statistically. Therefore, a version of the IATE model developed based on a specific experimental configuration can have completely different performance on a different experimental configuration. In the previous studies, the solution to mitigate this issue is to either revise the constitutive models or change the coefficients in the models to fit their cases. As a result, currently there are multiple versions of IATE models specifically for different two-phase flow configurations. In this sense, the benefit of the IATE in dynamic modeling the two-phase flow in the multiple geometrical configurations disappears. Hence, the efforts to properly unifying the different versions of IATE into a generalized model that can predict over high geometric scalability are essentially needed.

Another remaining work of the IATE development is that the IATE for transition flows. Although the IATE is featured as non-flow-regime-dependent, it is realized by fully considering the interfacial area transport in the full flow regime spectrum. The existing work generally considers the bubble interactions by giving an arbitrary bubble number distribution function, which is determined by referring to the fully developed flows. However, this bubble distribution function can be highly invalid for transition flows. The bubble number distribution function can also be dynamically changed. One possible solution is to develop an empirical model that predicts the dynamic change of bubble number density function for transition flow. However, this approach will introduce additional computational difficulties when coupling with the bubble interaction models. Another approach is to statically average the bubble interaction process in the developing flow based on proper assumptions. A good attempt was made by the study of Worosz [14] that successfully modeled the two-phase

flow under one-group to two-group transition in a medium-sized circular pipe. However, the experimental data used in Worosz's study doesn't fully capture the characteristics of transition flows. For example, Dang et al. [31] and Wang et al. [32] performed an interfacial area transport experiment and both reported a strong intergroup transfer phenomenon during the transition from bubbly to slug flow. Wang et al. [33] also stated that the current IATE models are not able to give satisfying predictions on this phenomenon unless manually adjusting the arbitrary coefficients in one order of magnitude, which is not a feasible solution since the coefficients that are determined experimentally should not be varied in one or more orders of magnitude. This suggests that the existing model needs to be physically reformulated by considering the flow regime transition mechanisms.

1.4 Objective of Research

The objective of this research is to develop a generalized IATE applicable over a wide range of flow channel sizes. One required work to realize the objective is to make applicable the existing IATE models, originally developed for the relatively large flow channel, to the small flow channel. In small flow channels, the wall effects on the interfacial area change and transport are non-negligible. Therefore, a complete understanding of the wall effect on the two-phase flow interfacial structure and interfacial area transport is necessary for IATE the model development.

1.5 Contribution of the Current Work

To realize the objective, the technical approaches and major contribution of this current work are summarized as follows:

- Extend the current interfacial area transport data range by measuring two-group interfacial area parameters on 12.7 mm inner diameter pipes, ranging from bubbly to churn-turbulent flow and focusing on the transition regime

- Analyze the two-phase flow structure and flow regime transition using the newly obtained data in small diameter pipe and the existing data in medium and large diameter pipes

- Analyze the pipe diameter effect on interfacial area transport by considering the wall effect on the bubble dynamics

- Develop interfacial area transport models with high geometrical scalability based on the analysis result of the wall effect on bubble interactions

2. EXPERIMENTAL SETUP

To investigate the pipe size effect on the interfacial characteristics and evaluate the interfacial area transport equation, a reliable database should be developed. In terms of the flow channel size, there is no comprehensive two-phase flow data for small vertical circular pipe in which the bubble diameter is comparable to the pipe diameter. In such a pipe, the two-phase flow can be largely influenced by the pipe wall, especially during the bubbly-to-slug transition flow that the two-phase flow is experiencing a large changing of bubble size. For the adiabatic, air-water flow condition, the hydraulic diameter of the flow channel is approximately equal to the maximum distorted bubble diameter, $D_h \approx D_c = 4\sqrt{\sigma\ g\Delta\rho} = 10.9mm$. [34] Flow channel with its size smaller than D_c can be regarded as capillary pipe. In the engineering design, the flow channel size of 12.7 mm is the closest to the maximum distorted bubble diameter. In this situation, the 12.7 mm diameter pipe can be approximately considered as the boundary size between the capillary pipe and the small diameter pipe. The two-phase flow experiments on this special size of pipes can reveal unique flow characteristics. Therefore, this study proposed an experimental study using the test facility built up with the test section made of 12.7 mm-inner-diameter round pipe and under an adiabatic air-water condition. In this chapter, the setups of the experimental facility are described in detail. The measurement instrumentation including the four-sensor conductivity probe and impedance void meter are introduced. The detailed data processing principles and methods are provided.

2.1 Experimental Facility

The schematics of the current experimental facility is given in Figure 2.1. The design purpose of this experimental facility is to simulate the two-phase flow development along a uniform shape flow channel under steady-state boundary conditions. The two-phase flow at the boundary, namely the inlet of the measurement section, is a finely mixture with the dispersed phase in form of uniform-sized small bubbles. To realize it, a well-designed injection system is utilized, as depicted in Figure 2.3. The most important part of this injection system is the porous surface on a tube that the dispersed phase (air) prior to

entering into the measurement section is pushed through and becomes finely dispersed. Besides, the injection system is able to divide the continuous phase (water) into two steams: the secondary steam with a relatively low and steady flow rate($\approx 0.1 m/s$) serves to shear the air off in a constant rate. Primary water flow is injected into the remaining injector space around the annulus and mixes with the two-phase flow at the test section inlet. The driving force of the water flow is supplied by a 25 hp centrifugal pump, the frequency of which can be preciously controlled. The water flow rate is measured by electromagnetic liquid flow meters. The air is supplied by an external air compressor and measured by rotameters.

In the measurement section, the flow channel is made of acrylic tube that a complete visualization can be realized due to its transparency. Three measurement ports at different elevated locations are arranged on the test section, Their locations can refer to Figure 2.2. To ensure the verticality of the test section, 5 additional support units are mounted evenly along the test section. For each measurement port, A probe traversing system is mounted for traversing of the four-sensor electrical conductivity probe. Additionally, each port also contains an impedance meter for measuring area-averaged void fraction and a pressure tap for measuring local pressure. After exiting the test section, the mixture of water and air goes into the storage tank, where water and air are separated automatically and the cycle is finished.

Liquid flow rate is measured with an electromagnetic flowmeter (Honeywell MagneW 3000). The output signal of the flowmeter is a 4-20 mA current, and it is converted into a voltage signal by passing through a 250 $\pm$ 1-ohm resistor. The voltage is collected by a communicator or recorded by a computer. The final uncertainty of the liquid flowrate measurement is $\pm 1.1\%$. **Air flow rate** is measured by rotameters. Four sets of rotameters (Brooks Instruments) with different maximum flow rates are utilized for the measurement, covering the superficial air flow rate up to 27 m/s. The accuracy of the rotameters is $\pm$ 2% of full scale. **Local pressure** at each measurement port measured using differential pressure gauges (Honeywell). The measured DPs are pressure differences between local pressures and the pressure at the inlet, which is also determined as the system pressure. This allows us to obtain the pressure distribution and change along the axial direction of the test section during the experiment. The measurement uncertainty is $\pm$ 0.025% of the total setup range. **Local**

interfacial parameters are measured using the four-sensor conductivity probe, following the design by Kim [11]. The detailed configuration and measurement principle are provided in the following section. The data acquisition system used for all the parameters mentioned above is consists of data acquisition boards (NI USB-6255, National Instruments, Austin, TX). The measurement frequency is 100 kHz. These boards are connected with a computer for data reading and recording.
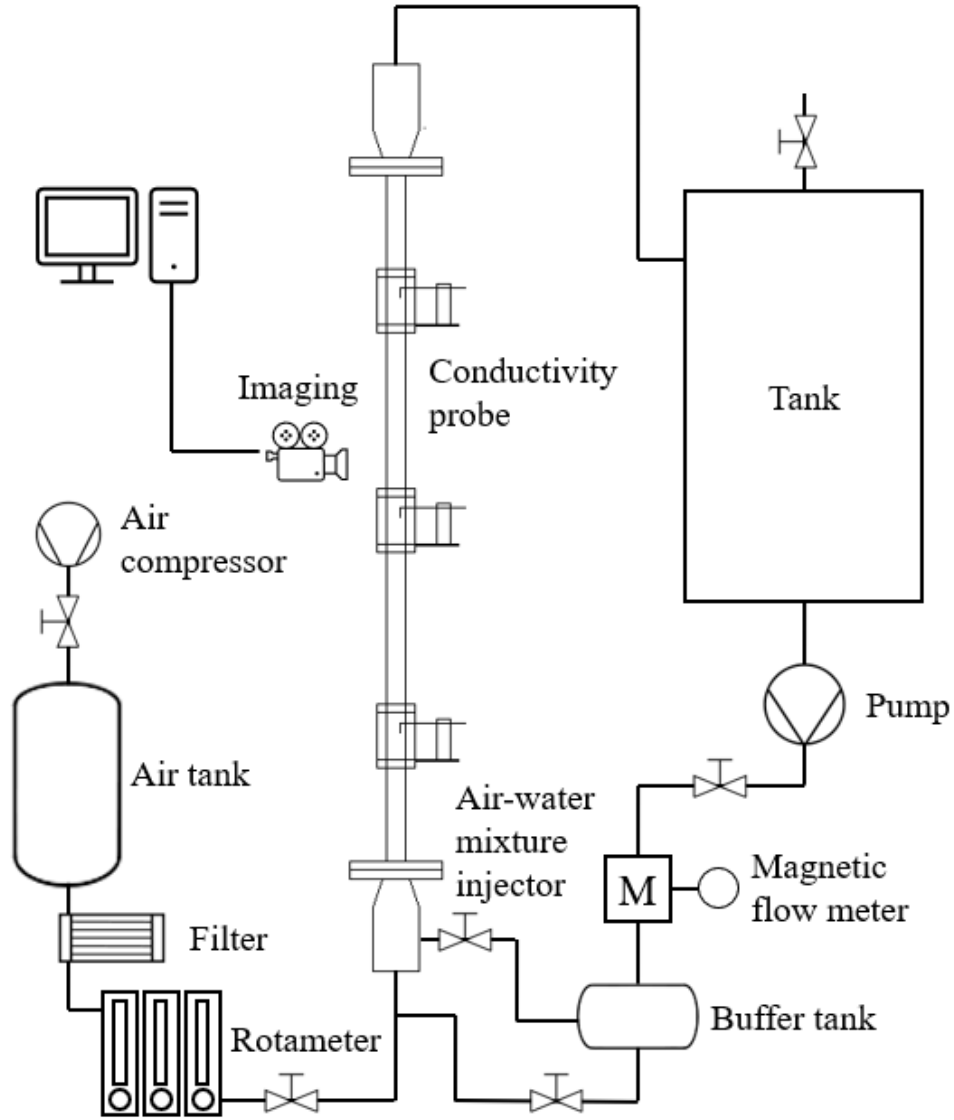
Figure 2.1. Schematic diagram of the experimental facility.

2.2   Instrumentation

2.2.1   Four-sensor Conductivity Probe

The four-sensor electrical conductivity probe is the major instrumentation for the local two-phase parameter measurement. The use of conductivity probe can be dated back to the 1960s by Neal and Bankoff [35]. The basic principle of two-phase flow measurement is based on the electrical conductivity difference between air and water. The design of this probe is
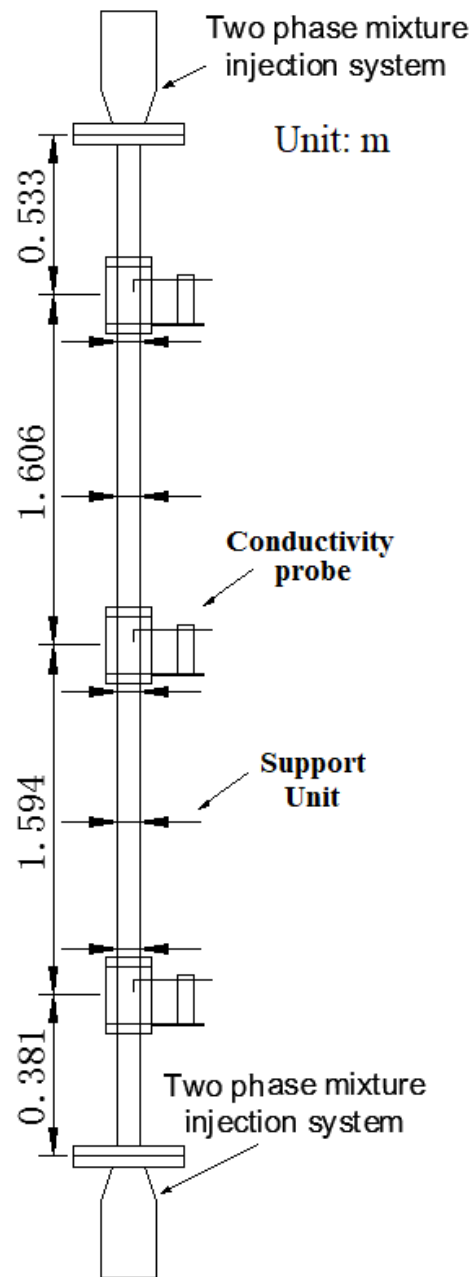
Figure 2.2. Schematic diagram of the test section.

Air

Sec. flow

Pri. flow
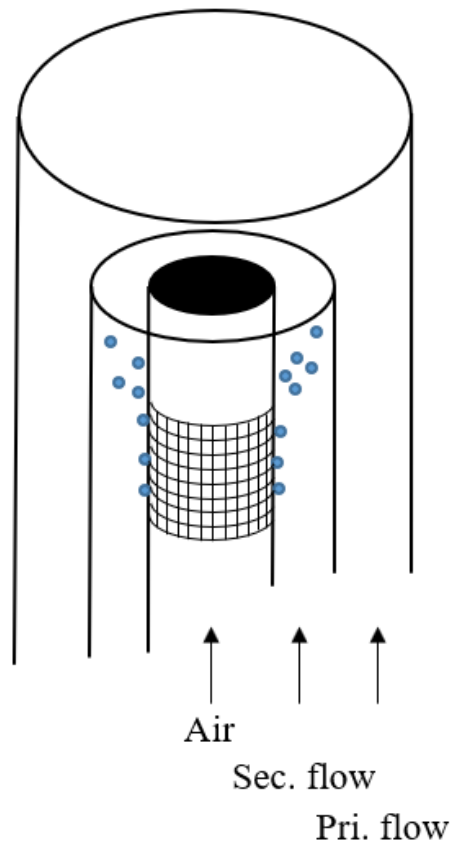
Figure 2.3. Close-Up view of air-water injection annulus.
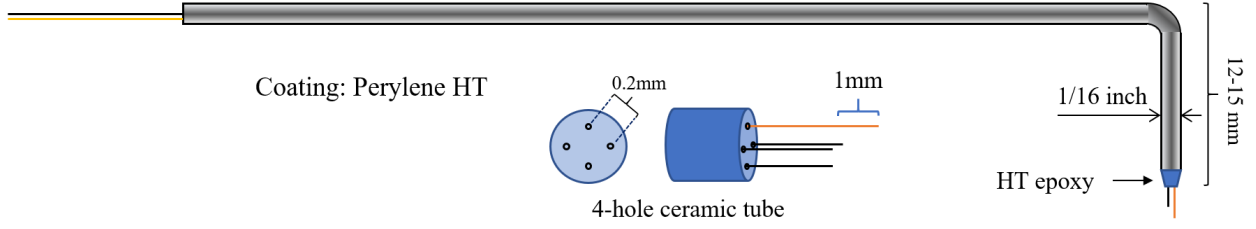
Figure 2.4. Four-sensor conductivity probe design.

based on the study of Kim et al. [11], who developed a miniaturized four-sensor conductivity probe methodology and signal processing scheme that largely extends the application range and measurement capacity. To accommodate the measurement in a small flow channel, the diameter of the probe is set to be 1.58 mm, which is around 1/8 of the pipe diameter. The configuration of the four-sensor conductivity probe is described in Figure 2.4. The two-phase parameters that can be obtained using the four-sensor conductivity probe are: void fraction, interfacial area concentration, bubble velocity, bubble Sauter mean diameter, and bubble frequency. [14] These parameters are calculated using the electrical time-series signals from the probe sensors.

Specifically, the local time-averaged void fraction can be calculated by counting the time that the leading sensor is touching the air over the measurement time interval. The principle of measuring the bubble interfacial velocity can be simply understood as the time needed for the interface passing the sensors. [34] A detailed discussion of the interfacial velocity measurement principle can be found in Shen et al. [36]. The basic principle for interfacial area concentration measurement was first proposed by Ishii [18], who showed that interfacial area concentration is related to interfacial velocity as

$$\overline{a}_i = \frac{1}{\Delta T} \sum_j \left(\frac{1}{|\vec{v}_i \cdot \vec{n}_i|} \right)_j \tag{2.1}$$

where v_i is the interfacial velocity, n_i is the normal direction to the interface, ΔT is the total elapsed measurement time, and j indicates the j-th bubble interface. Kataoka et al. [9] derived formulations to determine the local interfacial area concentration for both dual-sensor and four-sensor conductivity probes. For the dual-sensor probe, some assumptions

need to be made about the bubble shape and the angle of incidence of the bubble. For this reason, the dual-sensor probe is only effective in bubbly flow, where bubbles can be assumed spherical. For other flow conditions, a four-sensor probe is necessary. Later on, Revankar and Ishii [37], Kim et al. [11], and Shen et al. [36] further improved the method for measuring the interfacial area concentration. Among all the parameters, the maximum measurement uncertainty of the conductivity probe goes to the interfacial area concentration. From the study of Kim et al., this uncertainty comes from the design of probe, and the statistical errors for signal processing, and they proposed the overall measurement uncertainty is about 10%.

2.2.2 Impedance Void Meter

In this study, ring-type impedance void meters are used for the area-averaged void fraction measurement. The design of a ring-type impedance meter is shown in Fig. 2.5. The term "ring-type" means the electrodes of the impedance meter are in the form of rings flush-mounted in the pipe wall. In the impedance meter system design, an alternating current is supplied to the electrodes. The electrodes are connected to the electronic circuit, which is specially designed so that the output voltage of the circuit is proportional to the measured impedance between the electrodes. In this situation, the output voltage of the circuit produced by the impedance circuit is proportional to the inverse of the impedance between the electrode pair. The void between the electrode pair can monotonically affect the impedance at ambient conditions. Thus, the measurement principle can be simply understood as measuring the percentage of void in the continuous water based on the differences of their electrical impedance. Specifically, the detailed measurement principle is provided in Schlegel's study [38]. According to Ohm's law:

$$j = \sigma(E + v \times B) \tag{2.2}$$

where σ, E, and v are water conductivity, electric field, and water velocity. B, the magnetic flux density and electric field are assumed to be irrotational. The impedance between two

electrodes G is the ratio of the total current passing through each electrode i, to the potential between electrodes V,

$$G = \frac{i}{V} = \frac{\int_l j \cdot dl}{V} \tag{2.3}$$

From Eq. 2.2 and Eq. 2.3,

$$G = \frac{\sigma}{V} \int_l \frac{\partial U}{\partial n} dl \tag{2.4}$$

where n is the direction normal to the curve l. To predict the impedance value in the flow field, the electric potential is assumed to be uniform. Therefore, the impedance between the two electrodes is linearly proportional to the conductivity. For simplicity and to account for changes in liquid conductivity, it is convenient to define the non-dimensional impedance as

$$G^* = \frac{G_m - G_1}{G_0 - G_1} \tag{2.5}$$

where G_m is the instantaneous two-phase mixture impedance, G_0 is the impedance when the void fraction is zero (i.e., single-phase water) and G_1 is the impedance when the void fraction is unity (i.e., single-phase vapor). Thus, the void fraction measured by the impedance void meter is an instantaneous, area-averaged void fraction.

2.3 Flow Regime Identification Method

The impedance void meter can produce a time-series signal measuring the instantaneous two-phase flow impedance, which is generally proportional to the averaged void fraction between the electrode pair. Other than the void fraction, the void distribution can also be reflected in the impedance void meter signal, meaning that with the same void fraction, two distinctive forms of void distribution can result in different impedance values. This is caused by the non-uniformed distribution of the electric field generated between the electrode pair. In this sense, the signal of the impedance void meter contains information of both void fraction values and macroscopic two-phase flow structure. On the one hand, a relatively accurate void fraction measurement using an impedance void meter can be realized by proper calibration using other void fraction measurement techniques. On the other hand, the impedance
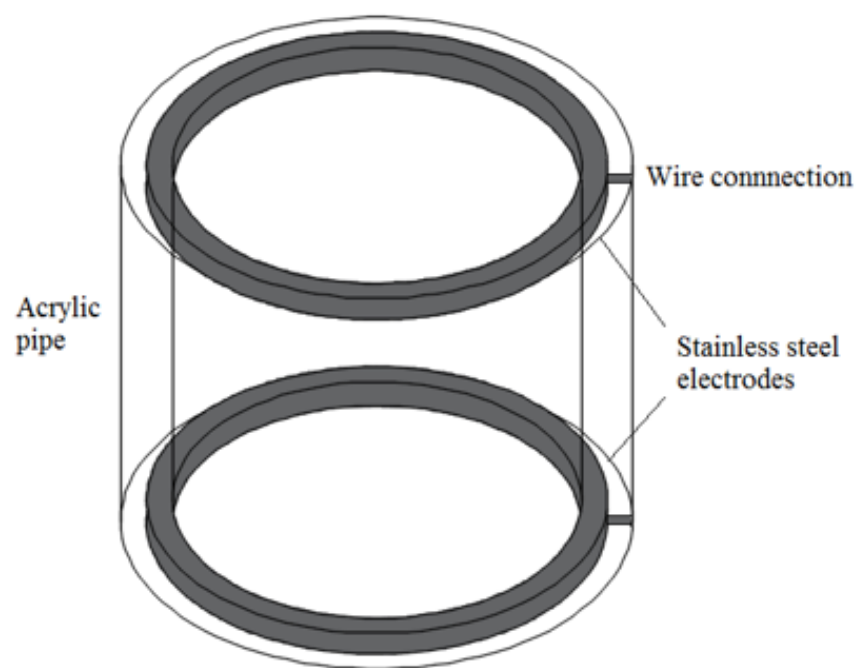
Figure 2.5. Design of ring-type impedance meter.

void signal without calibration can be used for the flow regime identification, since the flow regime characteristics can be largely determined from void fraction and flow structure.

The amount of data obtained from the experiment is relatively small for a supervised learning algorithm with a sufficient scale to analyze the complex two-phase flow characteristics. Therefore, an unsupervised learning algorithm, such as the self-organized map (SOM), is recommended for the flow regime identification problem. For example, Mi et al. [39] provided a multi-layer self-organized neural network for the flow regime identification using the void fraction time-series signal as the input data.

In this study, a Kohonen-typed two-layer SOM network is used, the design of which follows the same configuration used in the study by Schlegel et al. [40]. For the input data, the dimensionless impedance meter signal is converted into cumulative probability density function (CPDF), and fed to the network as vectors. An example of the CPDF for different flow conditions is provided in Figure 2.6. Given the fact that there is no training process for an unsupervised learning algorithm, the flow regime identification process randomly selected 90% of the total number of the dataset as the input, and repeat this process 5 times. The 5 identification results are combined into one flow regime map, in which the possibly uncollected flow conditions (which are hardly exist) are determined based on the neighbors and the flow visualization.
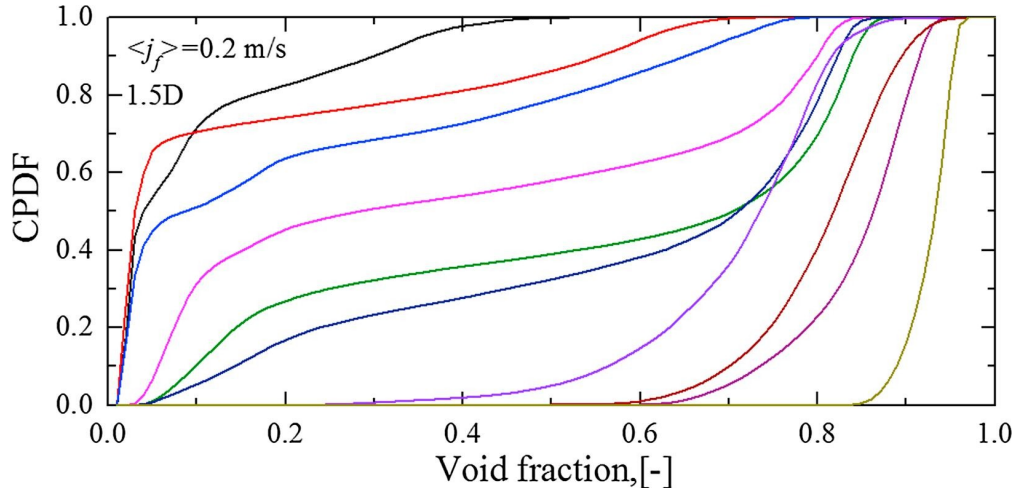
Figure 2.6. CPDF of impedance meter signal with different void fractions. [41]

2.4   Test Conditions

The flow conditions are determined based on the Mishima-Ishii flow regime map.[42], thus, these flow conditions are quantified using superficial gas and liquid velocities at the inlet of the measurement section. In the current study, 23 flow conditions in total were performed and they belong to bubbly-to-slug flow transition region based on the flow regime map, as shown in Fig. 2.7. The void fraction contour lines ($\alpha = 0.15$, 0.2, and 0.25) are also plotted as references. The detailed information about the flow conditions are given in Table 2.1.
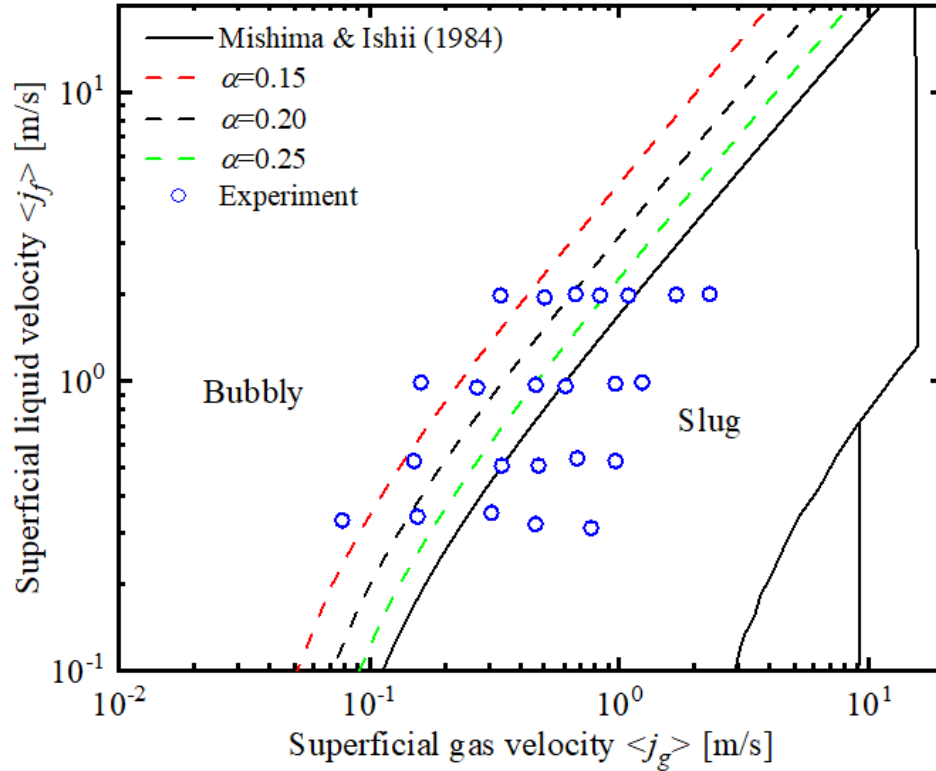
Figure 2.7. Experimental test conditions on Mishima-Ishii flow regime map.

$\langle j_f \rangle$, m/s	$\langle j_{g,0} \rangle$, m/s						
0.3	**0.078**	**0.156**	**0.308**	**0.462**	**0.772**		
$\alpha_{z/D=282}$	0.155	0.329	0.440	0.479	0.591		
0.5	**0.151**	**0.339**	**0.475**	**0.679**	**0.966**		
$\alpha_{z/D=282}$	0.203	0.288	0.403	0.408	0.513		
1.0	**0.161**	**0.270**	**0.463**	**0.610**	**0.966**	**1.235**	
$\alpha_{z/D=282}$	0.126	0.225	0.253	0.346	0.477	0.660	
2.0	**0.335**	**0.502**	**0.669**	**0.837**	**1.088**	**1.689**	**2.301**
$\alpha_{z/D=282}$	0.101	0.176	0.248	0.290	0.330	0.422	0.487

Table 2.1. Flow conditions.

3. EXPERIMENT RESULTS AND DISCUSSIONS

To fully understand the interfacial characteristics and bubble interaction mechanisms in vertical round pipes and the pipe diameter effect, a complete experimental analysis with the aid of data in pipes with different sizes is needed. In this chapter, an experimental analysis is presented focusing on identifying the pipe size effect, namely wall effect, on interfacial structure characteristics and the interfacial area transport mechanism. Specifically, a detailed presentation of the experimental results of the two-phase flow in a 12.7 mm ID vertical round pipe is provided, including the data validation, the local interfacial structure, and interfacial area transport in the axial direction. Besides, the discussion on the pipe size effect is presented in terms of interfacial area transport due to the bubble interaction mechanisms, drift flux analysis, and the flow regime transition. The analysis of the pipe size effect is based on the comparison among the new experimental data for small pipe flow and the existing data for medium size pipe flow.

3.1 Data Validation

To assess the veracity of the conductivity probe measurements, the measured void fractions at the three axial locations are compared with the impedance meter measurements. To compare with the global void fractions, the local void fraction values from conductivity probes are area-weighted averaged,

$$\langle \alpha \rangle = \frac{1}{R^2} \sum_{i=1}^{N-1} \alpha_i (r_{i+1}^2 - r_i^2) \tag{3.1}$$

Besides, the volumetric gas flux calculated from the conductivity probe measurements is benchmarked against the volumetric gas flux obtained from the gas rotameters and pressure measurements. Specifically, the volumetric gas flux calculated from the conductivity probe measurements is obtained by area-weighted averaging the local void fraction times bubble velocity αv_g over the cross-section of the flow channel, similar to Eq. 3.1

$$\langle j_g \rangle = \langle \alpha v_g \rangle \tag{3.2}$$
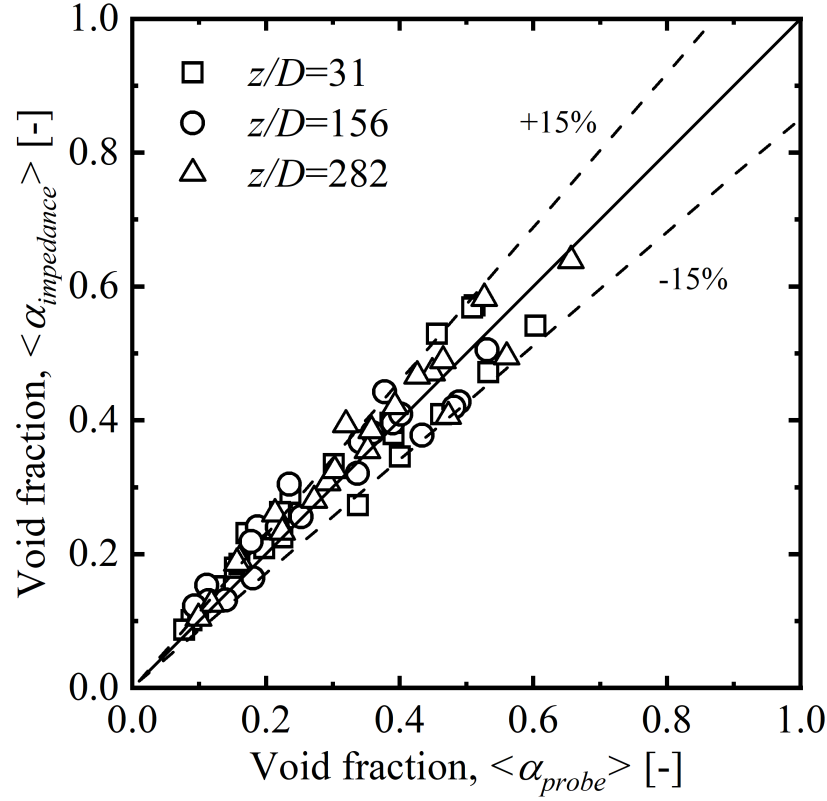
Figure 3.1. Void fraction benchmark of conductivity probe measurements against the impedance meter measurements.

The obtained values can be compared with the superficial gas velocities measured from the rotameters. The superficial gas velocity at each measurement location is obtained by converting the j_g at the rotameters to the local value using the local pressure,

$$\langle j_g \rangle_z = \frac{Q_{g,z}}{A} = \frac{Q_{g,atm}}{A} \left(\frac{p_{atm}}{p_{atm} + p_z} \right) \tag{3.3}$$

The cross-verification results are given in Figure 3.1 and 3.2. The relative difference between the conductivity probe and impedance meter on void fraction measurements is 12.86%. For the superficial gas velocity measurement, the relative difference between the conductivity probe and rotameters is 13.06%.
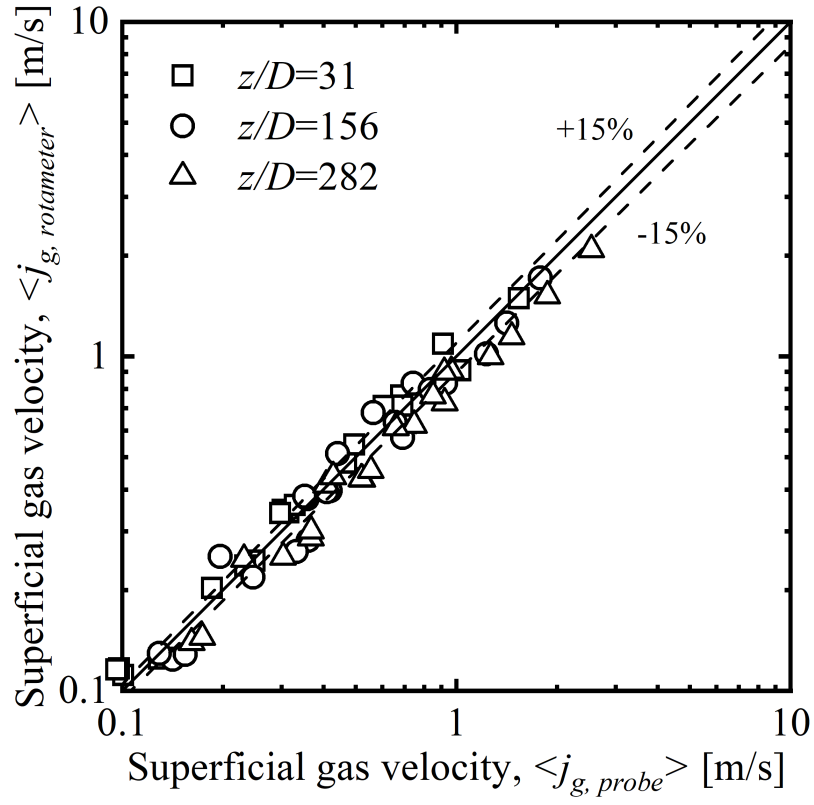
Figure 3.2. Volumetric gas flux benchmark of conductivity probe measurements against the rotameter measurements.

3.2 Interfacial structure for small diameter pipe two-phase flows

It is well known that the interfacial structure of two-phase flow is determined by the fractions of phases and the topological shape of the interface. These geometrical properties are strongly related to the boundary conditions of superficial velocities. The interfacial structure can be analyzed with the experimental results collected by the conductivity probes, which includes void fractions, IACs, and bubble velocities. Figure 3.3 shows the radial distributions of the two-phase flows at each axial measurement location. Three flow conditions with a similar superficial gas velocity $\langle j_{g,0} \rangle \approx 0.15 m/s$ are included. Figure 3.4 also provide measurement results with a similar superficial liquid velocity $\langle j_f \rangle \approx 0.3 m/s$, arranging in the same way as Figure 3.3. The superficial velocities are strongly related to the void fractions and relative velocity between phases, thus, they are clearly related to the local structure of the two-phase flow. For example, at the first measurement position closest to the inlet, $z/D = 31$, the increase of $\langle j_f \rangle$ can alter the void fraction and IAC distribution from a flat distribution to wall-peak distribution. As the flow develops and moves downstream to the other two measurement positions, the distributions shifts to core-peaked. This change of radial distribution during the flow development refers to the increase of bubble size, and large bubbles can migrate radially to the center of the pipe. This phenomenon has been studied and proved in the previous researches. [14], [31], [34] As the size of the bubble getting larger and exceed a critical value, the maximum distorted bubble diameter, the spherical shape of bubble can be deformed. This leads to the substantial change of the drag force and bubble interaction mechanisms. In the IATE, the bubbles with different shape (spherical and distorted) are classified into two groups, and the phenomenon above is named as intergroup transfer. From the results, the IAC drops greatly as two-phase flow develops, indicating that the speed of intergroup transfer can be rather high in a small diameter pipe, in other words, the intergroup transfer can be intensive in a small diameter pipe.

The intergroup transfer phenomenon is very important in modeling of the interfacial area transport and worth being further investigated. Figure 3.5 and 3.6 shows the axial development of the two-phase parameters. In these figures, the high intensity of the intergroup transfer can be clearly observed from the change of void fraction and IAC, as the change

due to pressure and velocity is not significant under the current experimental setup. For instance, the void fractions experience a large amount of transfer between groups that the profiles of the void fractions show an "X" shape. Meanwhile, the IAC of small bubble group drops in a high rate and the IAC of the large bubble group can increase (the rate is not as high as small bubble group due to the surface area to volume ratio is low for large bubbles). Additionally, the axial change of bubble diameter (the Sauter mean diameter $= 6\alpha/a_i$) reveals the characteristics of intergroup transfer: the bubble diameter of small group bubble increases up to a critical value (4 -4.5 mm) and decreases as the larger bubbles in the group transfers to the large bubble group.

Fig. 3.7 and 3.8 further provides the void fraction and IAC change along the axial direction for all the experimental flow conditions. The sub-figures are arranged in the order of the points on Figure 2.7. With these two figures, it can be observed that the flow conditions where the intensive intergroup transfer exists are grouped on the maps. In terms of the superficial velocities, both $\langle j_{g,0} \rangle$ and $\langle j_f \rangle$ are positively related to initiate the intensive intergroup transfer, which means the increase of $\langle j_f \rangle$ will result in a larger $\langle j_{g,0} \rangle$ in order to realize the intensive intergroup transfer. From the maps, the intensive intergroup transfer does not happen when $\langle j_f \rangle$ is higher than $= 2.0m/s$.
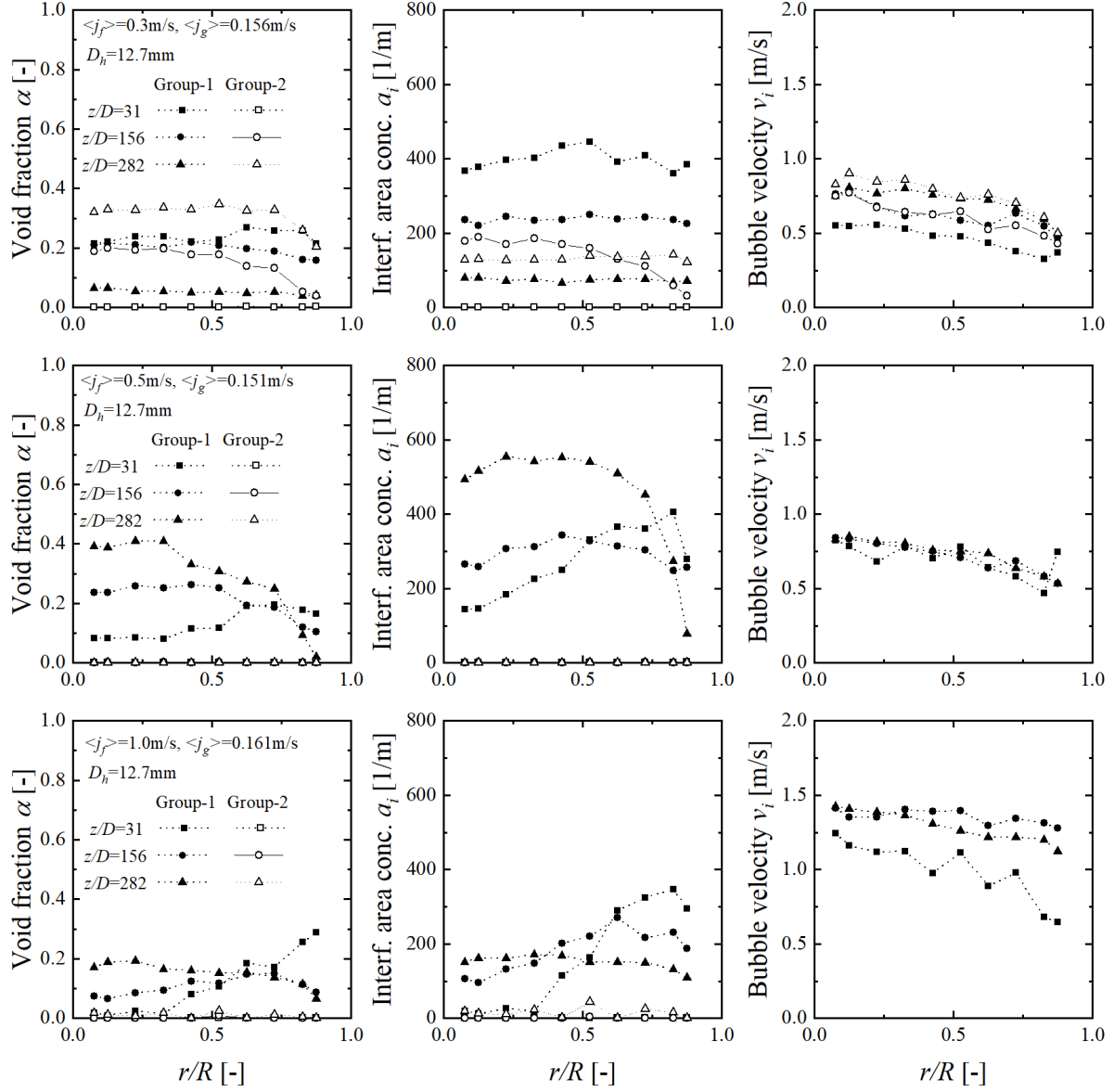
Figure 3.3. Two-group interfacial local profiles of three flow conditions with a similar superficial gas velocity.
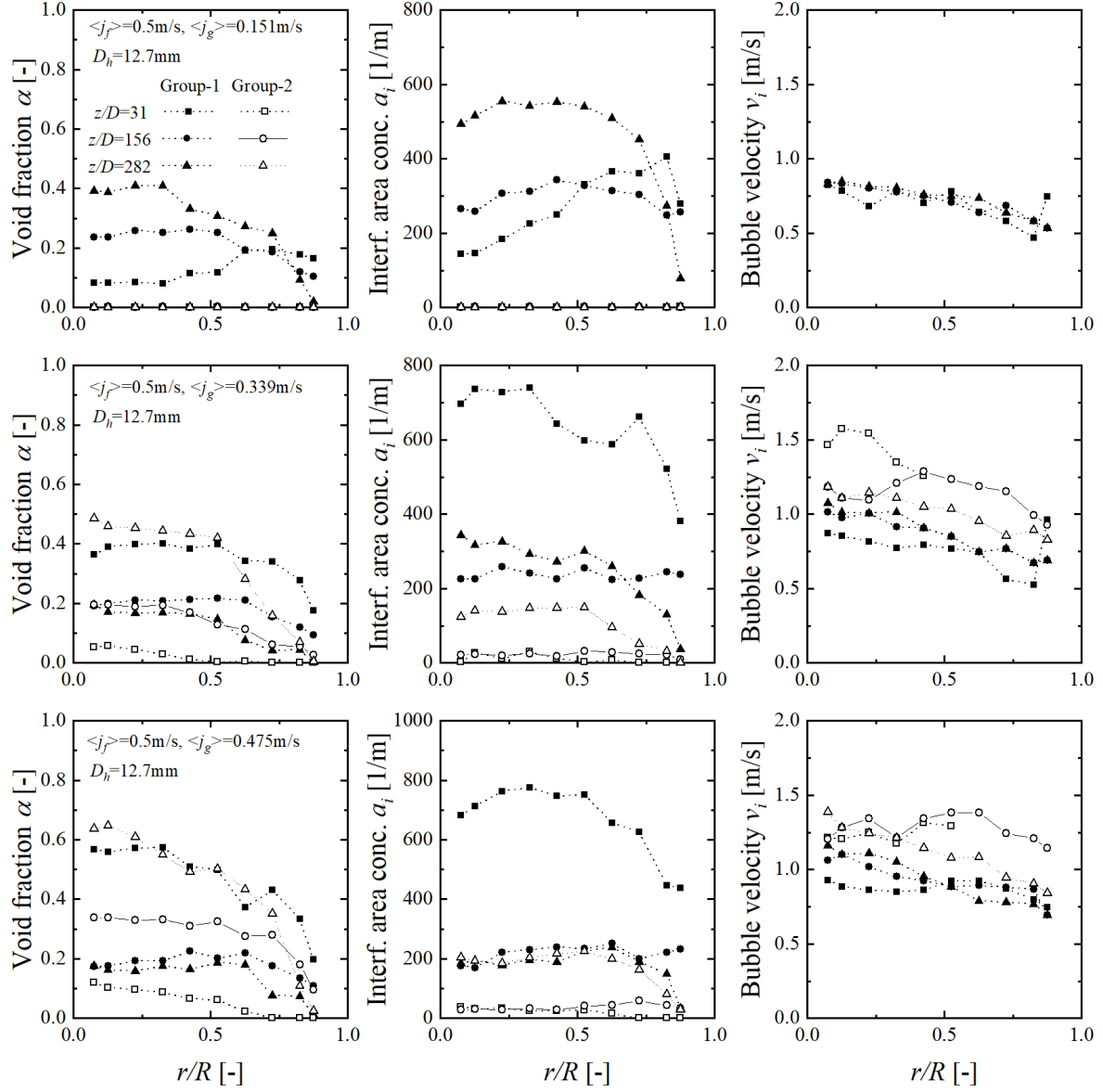
Figure 3.4. Two-group interfacial local profiles of three flow conditions with a similar superficial liquid velocity.
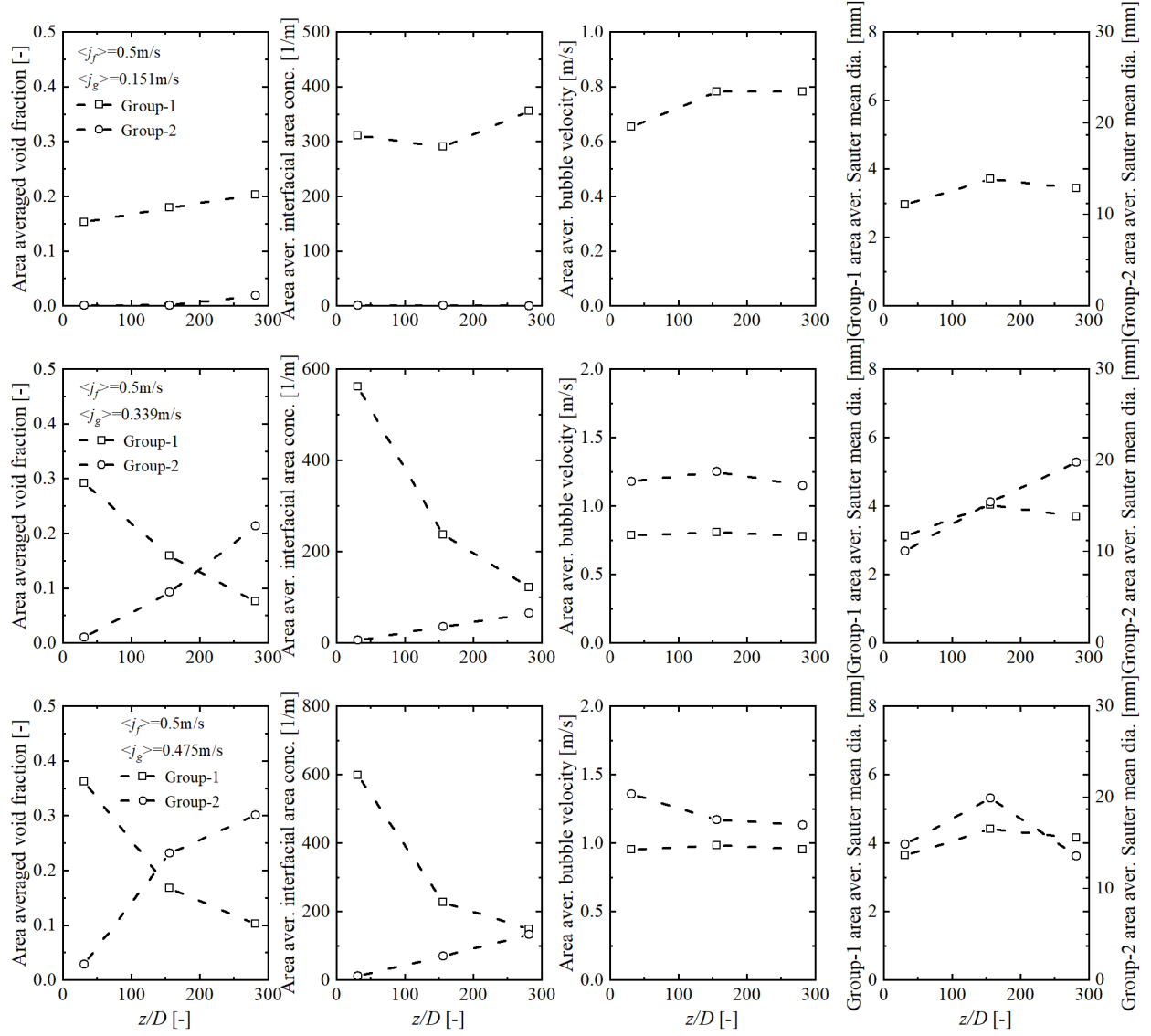
Figure 3.5. Area-averaged interfacial profiles of three flow conditions with a similar superficial gas velocity.
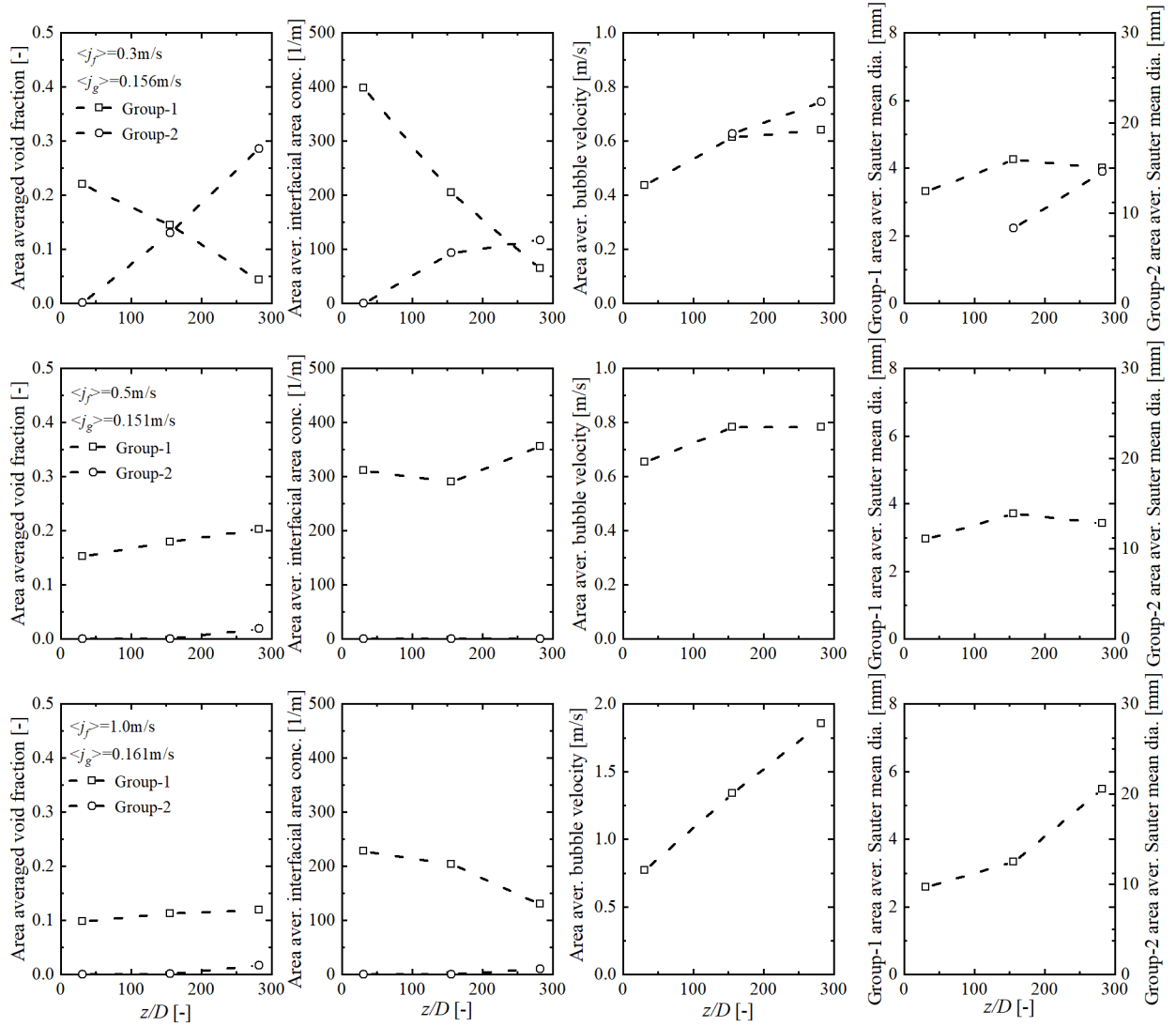
Figure 3.6. Area-averaged interfacial profiles of three flow conditions with a similar superficial liquid velocity.
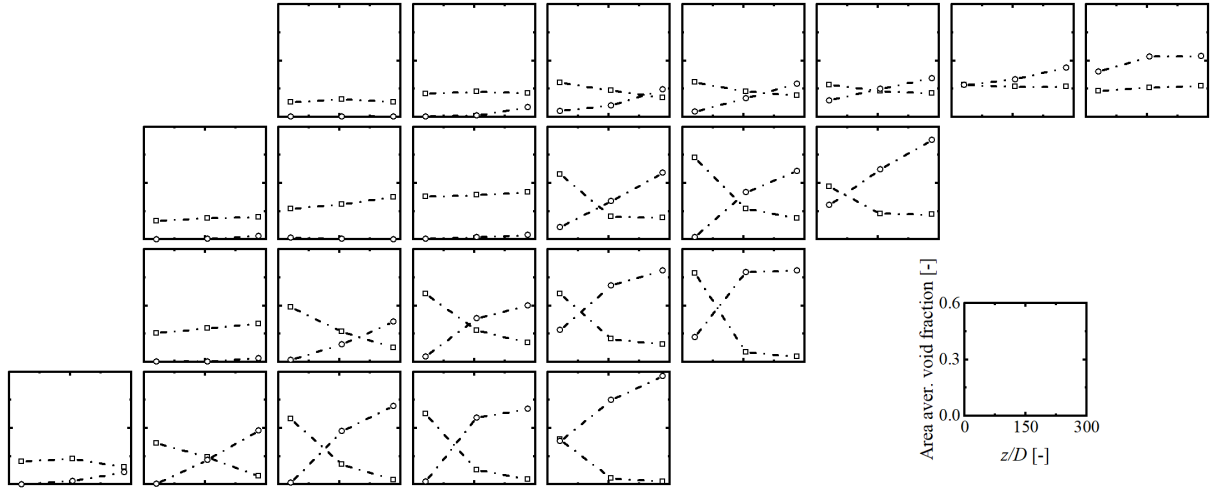
Figure 3.7. The area-averaged void fraction profiles arranged by superficial velocities.
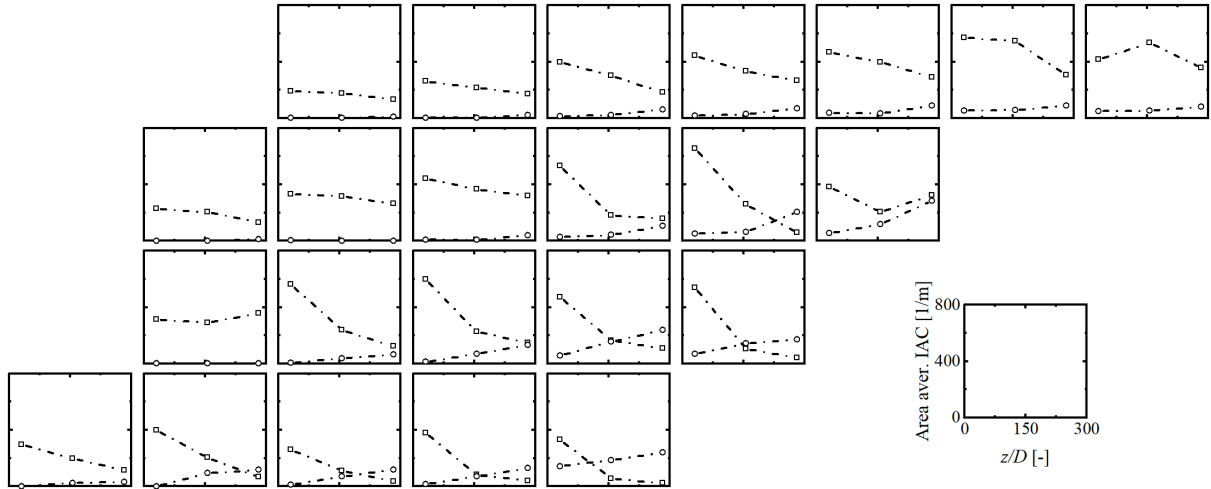
Figure 3.8. The area-averaged interfacial area concentration profiles arranged by superficial velocities.

3.3 Bubble Coalescence and Disintegration in Circular Pipes with Different Sizes

With this established database, the interfacial area transport due to bubble interactions in the circular pipes with different sizes can be compared. The calculation method used in this analysis follows the study of Wang et al. [43]. To summarize this method, firstly, the IAC change due to the bubble interactions is excluded in the calculation and only the pressure and velocity change (advection) effects are considered. The calculation results are considered to be free of modeling error since the two effects are calculated based on only experimental measurements, namely pressure and bubble velocities. By comparing the calculated IAC change and the experimental IACs, the intensity of the bubble interaction can be estimated. Specifically, the IACs along the axial direction are calculated based on the below expression,

$$\frac{d\left(\langle a_i\rangle_{eq}\langle\langle v_g\rangle\rangle\right)}{dz} = \frac{2}{3}\frac{\langle a_i\rangle_{eq}\langle\langle v_g\rangle\rangle}{\langle p\rangle}\left(-\frac{d\langle p\rangle}{dz}\right) \tag{3.4}$$

where $\langle a_i\rangle_{eq}$ is the calculated IAC that only considers the pressure and velocity effects. The interfacial area transport due to bubble coalescence and breakup can be estimated by comparing $\langle a_i\rangle_{eq}$ and measured IAC $\langle a_i\rangle_{exp}$,

$$\xi = \frac{\langle a_i\rangle_{exp}}{\langle a_i\rangle_{eq}} \tag{3.5}$$

ξ larger than 1 indicates bubble breakup dominants in the preceding flow development, and bubble coalescence dominants if ξ is smaller than 1. Figure 3.9 shows the interfacial area transport in different small- and medium-sized pipes under similar flow conditions. From the figure, it can be observed that for all flow conditions, with a smaller diameter pipe, the bubble coalescence mechanism tends to be more dominant. For high j_f conditions, the bubble breakup is larger than the coalescence mechanism so that the ξ is over than 1. This indicates that under these conditions, the turbulence impact mechanism is greatly enhanced.
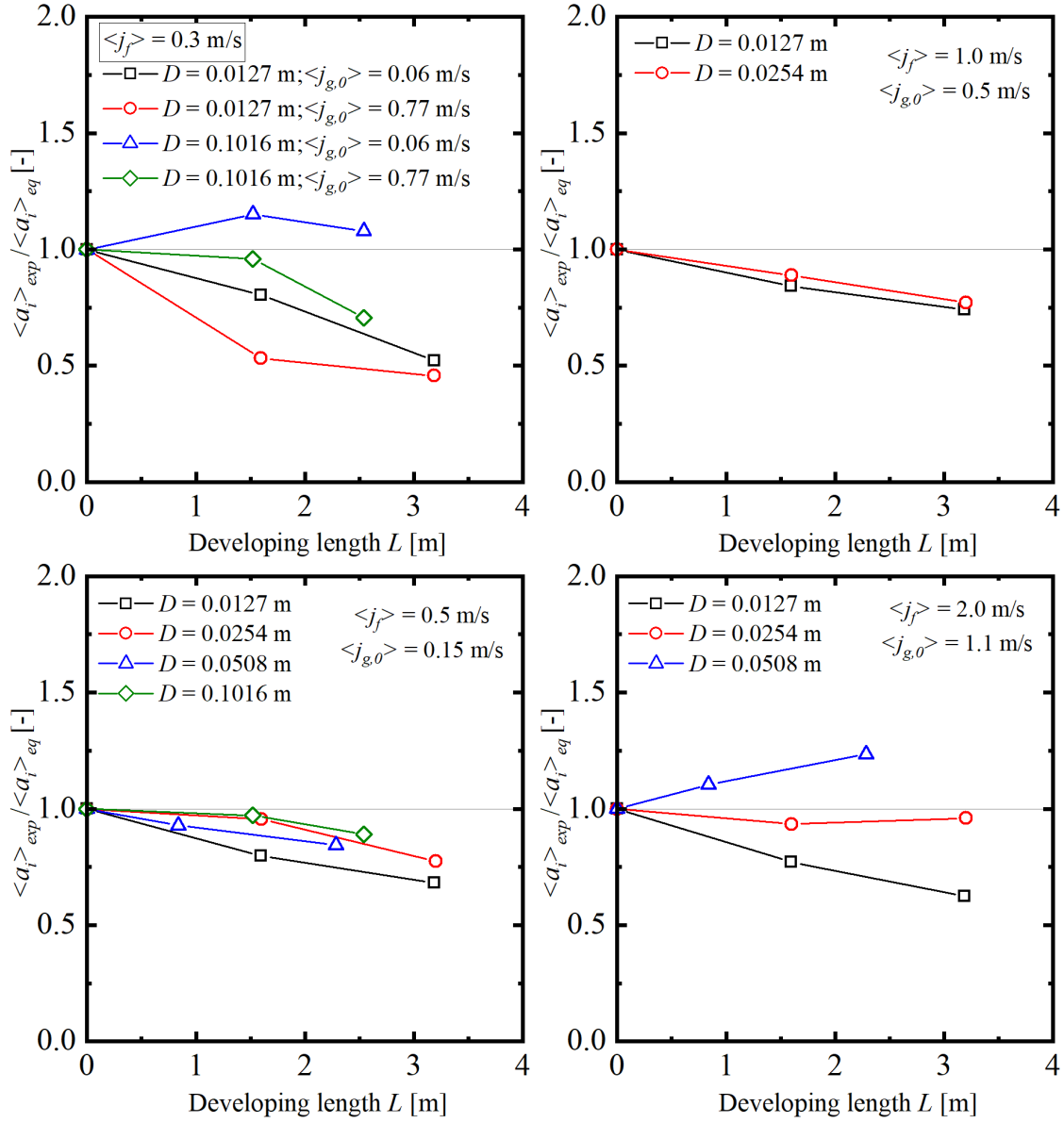
Figure 3.9. Interfacial area transport in the axial direction due to bubble coalescence and breakup.

3.4 Characteristics of Intergroup Transfer in Small Pipes

The intensive intergroup transfer was observed from the experiment that it is strongly associated with the flow conditions. While the experiment uses superficial velocities to determine the flow conditions, the intergroup transfer that is one of the characteristics of interfacial area transport is in reality related to the geometrical structure of two-phase flow. As discussed in the previous section, these geometrical structure can be void fractions and interfacial area concentration. The interfacial area concentration can be further represented using a more explicit geometrical parameter, bubble diameter. In this section, the characteristics of the interfacial transfer in small diameter pipe is analyzed in terms of the void fraction and the bubble diameter.

Before going into the detailed derivation of the relation between this unique phenomenon and the geometrical parameters. It is important to determine the mechanism that causes this phenomenon. In the existing IATE model for turbulent two-phase flows, the cause of small bubble to become large bubble through coalescence interaction is due to random collision and wake entrainment mechanism. The bubble coalescence due to random collision is the bubbles collide and collapse on each other driven by the turbulence in the continuous phase. The coalescence due to wake entrainment, on the other hand, happens on bubbles in align with the flow direction. The trailing bubble is within the wake region created by the leading bubble. Within this region, the relative velocity of the trailing bubble towards the leading bubble increases, and the two bubble can collide with each other. The wake entrainment is not strongly related to the existing flow turbulence, and it relies on the relative velocities of the leading bubble so that creates the wake region. It can be indicated that for small diameter pipe flow where the flow turbulence is relative low, the random collision can be correspondingly weak. However, from the previous section, the overall coalescence rate increases in a small diameter pipe. It indicates that the wake entrainment mechanism should be greatly enhanced for small diameter pipe flow. This indication can actually be proved from the experiments. As shown in the experimental observations 3.10, the cross-sectional area of the wake region created by the leading bubble can almost cover the whole pipe cross-section in a small diameter pipe. Given the local distribution of the small diameter pipe

two-phase flow, this leading bubble has few lateral bubbles, and it can affect all the bubble behind it. In this sense, this leading bubble can be regarded as more effective than regular leading bubbles. The reason that causes the leading bubble to be effective is due to the relative size between bubble and flow channel. Thus, to analyze this problem, a model that considers the geometrical relation between bubble and flow channel is needed.

The bubble's motion when rising in water can be decomposed into two types: one is that bubble moves in the rising direction; another one is it moves in either spiral or zigzag mode, which is also known as bubble secondary motion [44]. This secondary motion can be complex, and to simply this theory for the current modeling, it is assumed that the spherical bubble moves in spiral motion, and the covering cross-sectional area through this motion being modeled by a circle with its diameter equals to an equivalent diameter D_m. Besides, it is further assumed that the magnitude of the bubble zigzag motion and the spiral motion is approximately same, which is proved experimentally [45]. In this sense, we can estimate the D_m through a simple mathematical model. The established modeling is described in Figure 3.11. Based on the assumptions, D_m can be modeled using the partition of drift velocity v_{gj} in the radial direction and the spiral motion frequency,

$$D_m \approx D_b + \frac{v_{gj}\sin(\theta_b)}{2f_{os}} \tag{3.6}$$

where θ_b and f_{os} are the inclination angle of the bubble and the bubble oscillation frequency, respectively. From Miyahara et al. [46], θ_b is almost constant ($\sim 25°$) when bubble Reynolds number is less than 3000. The bubble oscillation frequency f_{os} is usually represented by the Strouhal number ($Sr_b = f_{os}D_b/U_b$). Tsuge and Hibino [47] performed a dimensional analysis using their data and established a relationship between Sr_b and C_D using the following correlation,

$$Sr_b = \begin{cases} 0.100C_D^{0.734} & (C_D \leq 2) \\ 6.13 \times 10^{-3}C_D^{4.71} & (C_D > 2) \end{cases} \tag{3.7}$$

By introducing θ_b and f_{os}, the relation between bubble diameter and the bubble motion diameter is expressed as,

$$D_m = D_b\left(1 + \frac{v_{gj}\sin(\theta_b)}{2Sr_bv_b}\right) \tag{3.8}$$

65

Bubbly flow near flow regime transition
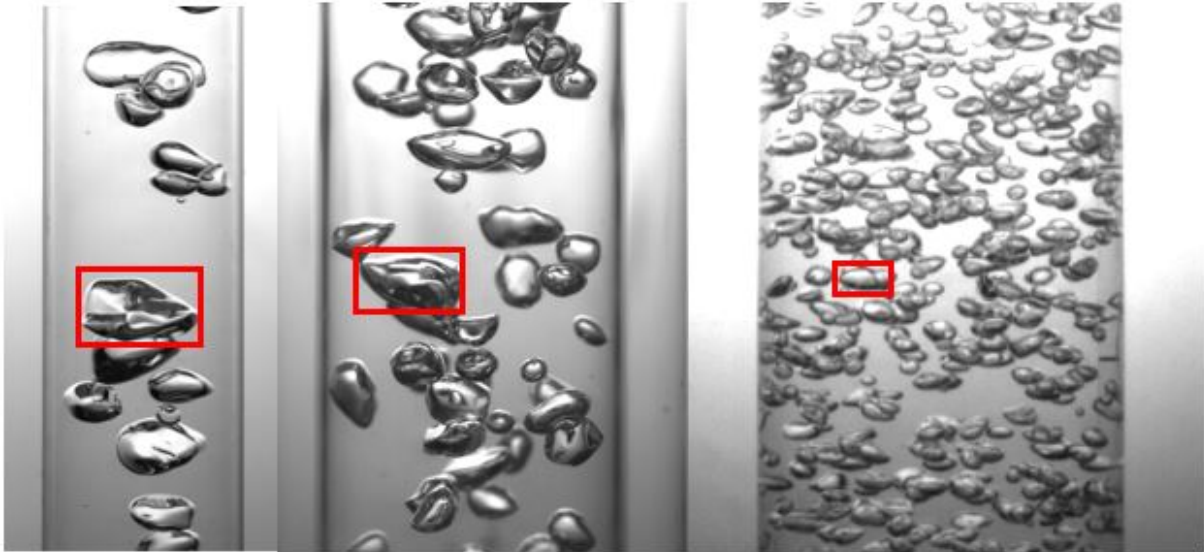
12.7mm ID pipe   25.4 mm ID pipe   50.8 mm ID pipe

Cap-bubbly flow near flow regime transition
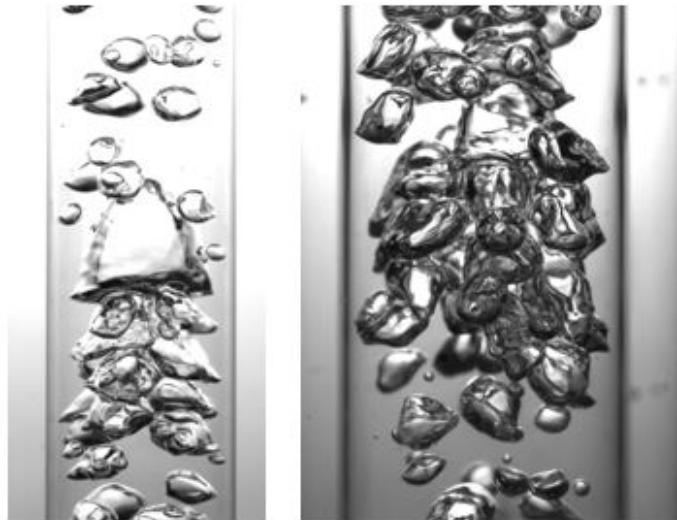
12.7mm ID pipe   25.4 mm ID pipe

Figure 3.10. Experimental observations of the bubble distributions in different diameter pipes using high-speed camera.

The geometrical relation between the bubble size and the pipe size can be established through the comparison of bubble diameter and pipe hydraulic diameter. The boundary situation that the leading bubbles with same diameter are in a semi-triangle arrangement so that they can cover almost all the pipe cross-sectional area. Figure 3.11 describes this model. In this case, the relation between bubble diameter and the pipe diameter is expressed as

$$\frac{D_m}{D_h} = \left(\frac{3}{2\sqrt{3}+3}\right)\lambda \tag{3.9}$$

λ is the ratio describing the maximum distance that bubbles can occupy in the flow cross-section. Based on the formulation of slug bubble, λ equals to 0.9.[8] In this situation, the bubble diameter is calculated as

$$D_{tr} = \frac{0.41}{1 + \frac{v_{gj}\sin(\theta_b)}{2Sr_b v_b}} D_h \tag{3.10}$$

Another important fact that should be considered is that the wake region is formed behind the leading bubble. This consideration is necessary since for a small diameter pipe case, the critical bubble diameter calculated from the above equation can be rather small. However, a bubble with such as small size can not have a stable wake region behind it. In the existing literature, the emergence of wake behind particle in the fluid is usually quantified using the particle Reynolds number, $Re(D_{re}) = \rho_g v_r D_{re}/\mu_g$. In a steady-state fluid flow, this Reynolds number should be large enough for the formation of a stable wake region behind the bubble, and thus the corresponding bubble size can be determined. Figure 3.12 shows the experimental bubble Sauter mean diameter against calculated bubble diameters based on the above mathematical formulations. The experimental results were from the current experimental database with the pipe size of 12.7 mm (left), and Wang et al.'s work on a 25.4 mm pipe [32]. The figure shows the experiment and model match satisfyingly.
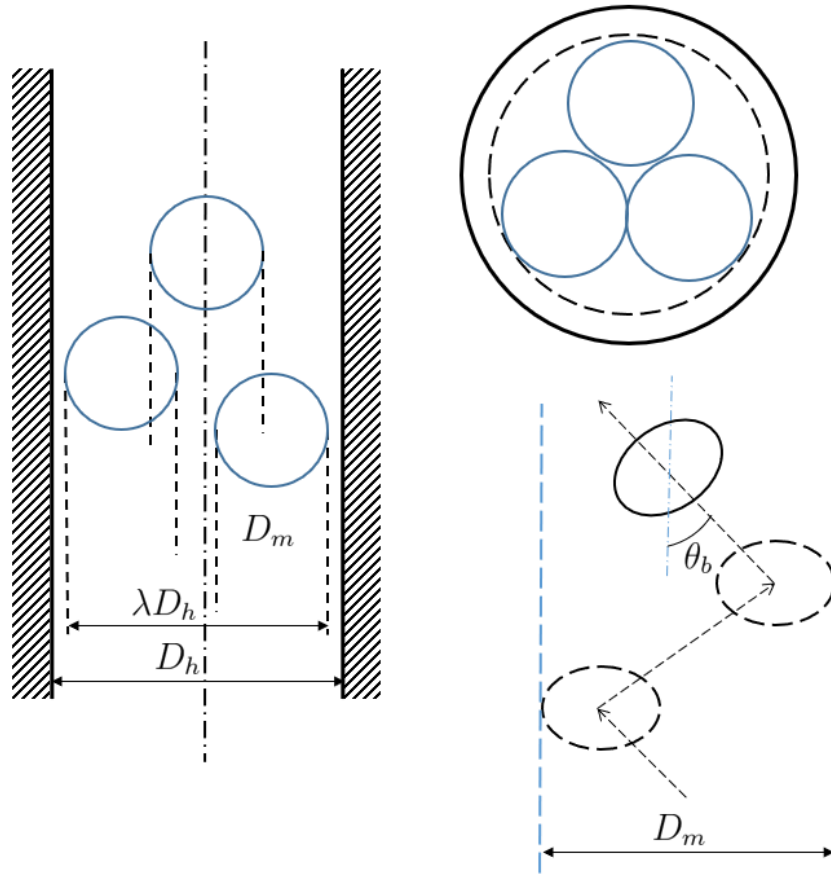
Figure 3.11. The geometrical relation between bubble moving area and the pipe cross-sectional area.
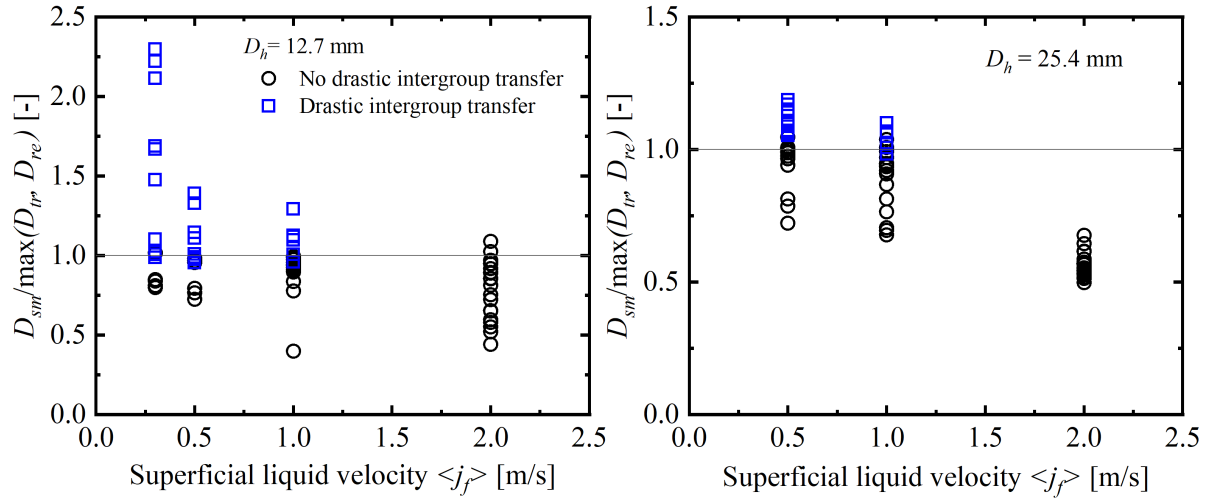
Figure 3.12. Bubble diameters against experimental observation on the intensive intergroup transfer: experimental data of the current study (12.7 mm) and Wang et al. (25.4 mm) [32]

3.5 Distribution Parameter and Drift Velocity

The peak position when wall peaking phenomena were observed has been studied in past researches. [5], [48], [49] In the study of Grossetete [49], the peak of the void fraction distribution can be approximately estimated by the bubble diameter. Specifically, it is reported by Hibiki et al. [5] that the peak location for a 3-mm diameter bubble in a 9.0 mm or 25.4 mm diameter tube is estimated to be about r/R= 0.67 and 0.88, respectively. It indicates that the void fraction distribution profile is related to the pipe diameter. More evidence is depicted in Figure 3.13 and 3.14. With the similar bubble size of these two test cases, the peak of the test case with a smaller pipe size is closer to the center of the flow channel. This phenomenon is easy to be understood since bubbles of the same size are closer to the centerline of the smaller pipe. This non-uniform distribution can affect bubble interaction. For example, in the wake entrainment mechanism, the number density of the trailing bubble behind a larger leading bubble is a crucial parameter. Since a large bubble tends to be closer to the center of the flow channel, the trailing bubble density within the wake region of the leading bubble can be smaller than the average bubble number density of the whole flow channel.

In the one-dimensional Drift Flux model, the non-uniform void fraction distribution of two-phase flow is modeled by the distribution parameter, C_0. The most popular correlation of distribution parameter is developed by Ishii, [50] which is originally for subcooled boiling flow in small diameter round pipes,

$$C_0 = (1.2 - 0.2\sqrt{\rho_\mathrm{g}/\rho_\mathrm{f}}) \left(1 - \mathrm{e}^{-18(\alpha)}\right) \tag{3.11}$$

This correlation shows that the void fraction is related to the non-dimensional distribution for bubbly flow. Although this correlation was developed for subcooled boiling flows, it was also used for adiabatic air-water conditions. Another correlation was proposed by Hibiki and Ishii [51] and they consider the distribution is related to bubble size,

$$C_0 = (1.2 - 0.2\sqrt{\rho_\mathrm{g}/\rho_\mathrm{f}}) \left(1 - \mathrm{e}^{-22(D_\mathrm{Sm})/D}\right) \tag{3.12}$$
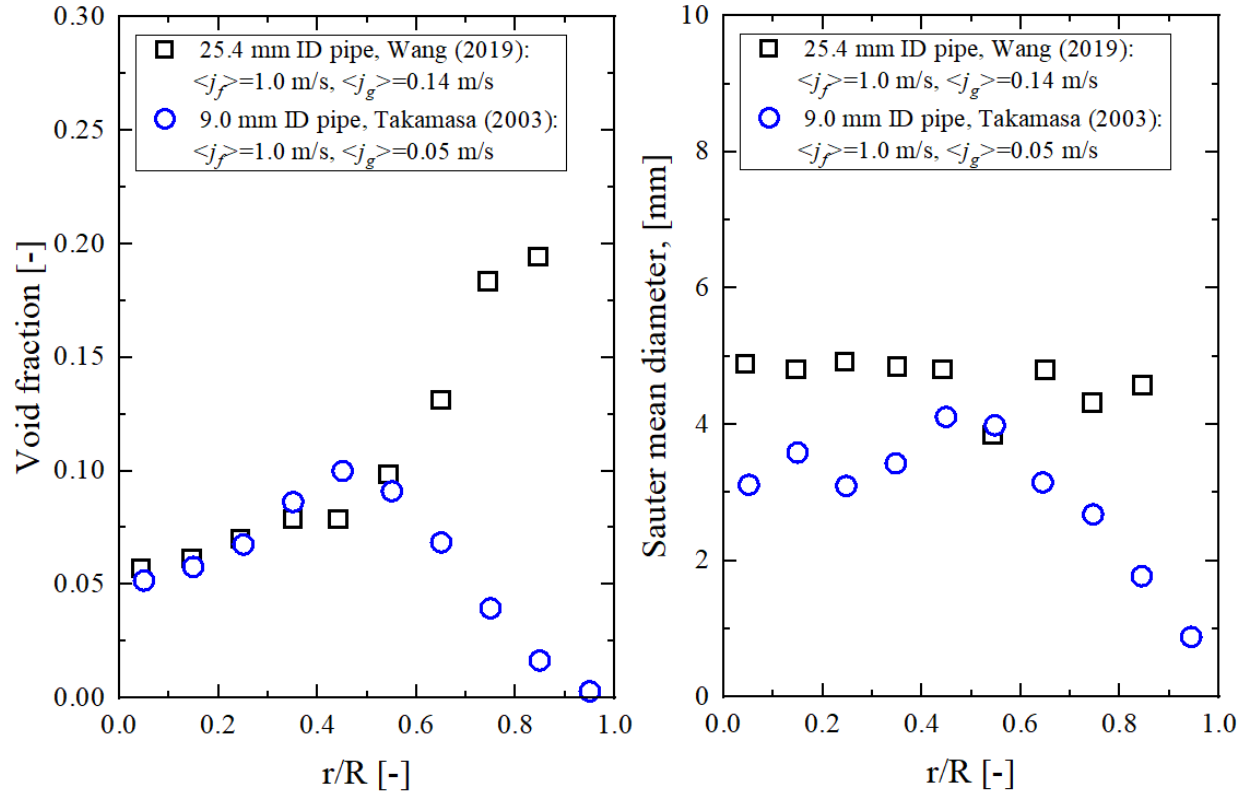
Figure 3.13. Wall-peaking distributions of the void fraction profile in test cases of 12.7 mm and 25.4 mm ID pipe size.
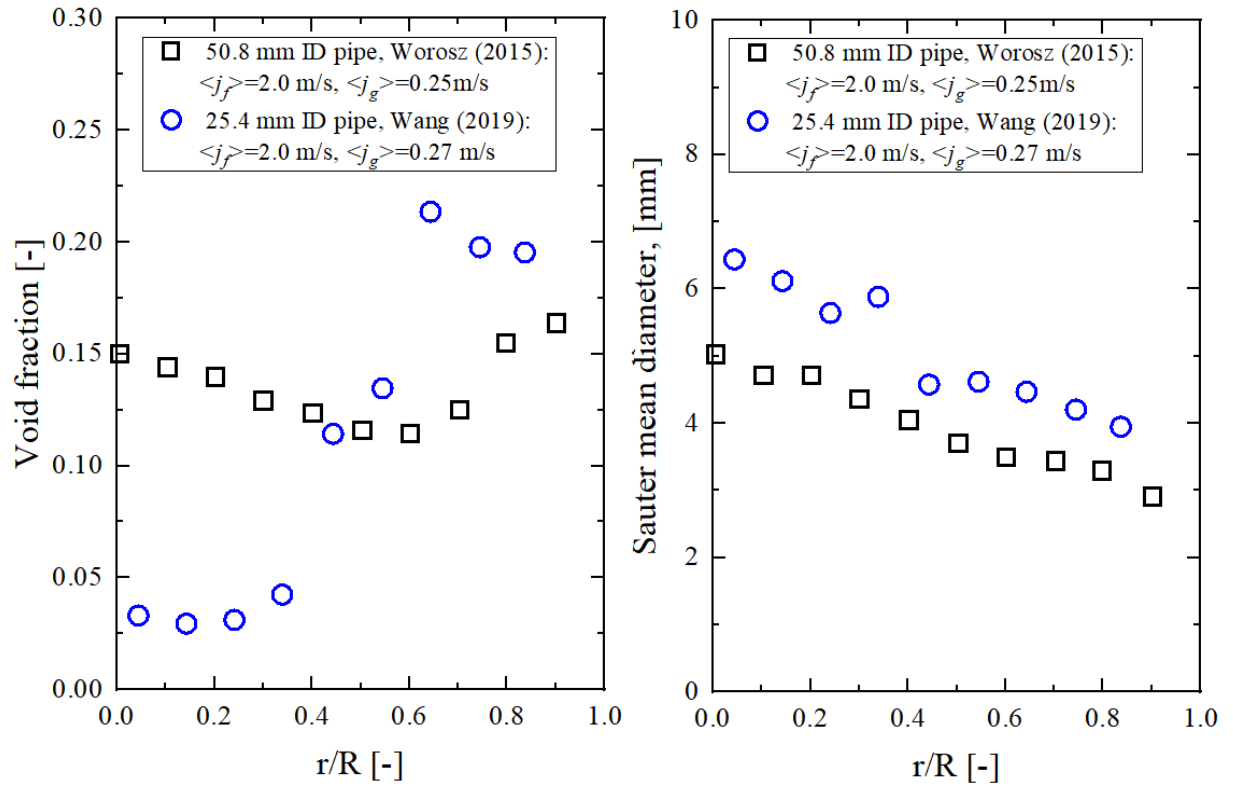
Figure 3.14. Wall-peaking distributions of the void fraction profile in test cases of 25.4 mm and 50.8 mm ID pipe size.

The performances of the two correlations are evaluated in the study of Hibiki and Ishii [51], which is given in Figure 3.15 and 3.16. The results show that the Ishii's correlation does not provide satisfyingly good predictions. While the performance of Hibiki's correlation is strongly related to the pipe diameter. Therefore, an improvement is made by properly combining this two models. This is because from the above experimental analysis, both void fraction and the bubble diameter contribute to the non-uniform distribution of two-phase flow. An understanding to this fact can be found in the conceptual schematics Figure 3.17. Assume that the two parameters affect the bubble distribution in the same order of magnitude, then the correlation is formulated in the following form,

$$C_0 = (1.2 - 0.2\sqrt{\rho_\mathrm{g}/\rho_\mathrm{f}}) \left(1 - \mathrm{e}^{-C_1 \langle D_{sm} \rangle / D_h - C_2 \sqrt[3]{\langle \alpha \rangle}}\right) \tag{3.13}$$

where C_1 and C_2 are coefficients determined experimentally. Based on these data, the coefficients are determined as $C_1 = 5$ and $C_2 = 3$. Figure 3.18a and 3.18b show the comparison of the new-derived correlation and experimental distribution parameters from multiple studies. Table 3.1 shows the performance of the distribution parameter correlations by comparing against data. It can be seen that both the modified Ishii's and the newly-derived correlation have better performance than the original Ishii's and Hibiki's corelations.

Table 3.1. The absolute relative errors of the distribution parameter models against experimental data.

Experiment	Eq.3.11[50]	Eq.3.12[51]	Eq.3.13
Hibiki et al., 1999, 25.4 mm[5]	13.0%	25.3%	5.9%
Hibiki et al., 1998, 50.8 mm[52]	13.8%	4.2%	5.2%
Wang et al., 2019, 25.4 mm[32]	7.5%	10.0%	4.9%
Worosz, 2015, 50.8 mm[14]	10.1%	10.4%	4.5%
Present, 12.7 mm	6.6%	8.5%	4.6%
Total	10.8%	11.2%	5.0%
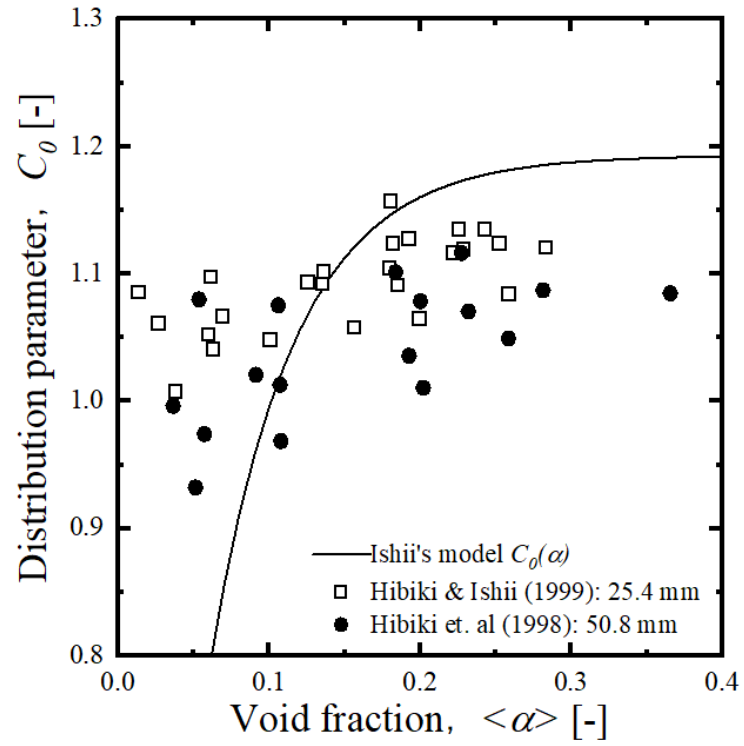
Figure 3.15. Comparison of distribution parameter correlation by Ishii (1977) with the experimental results (Hibiki et al, 1999, 2001).
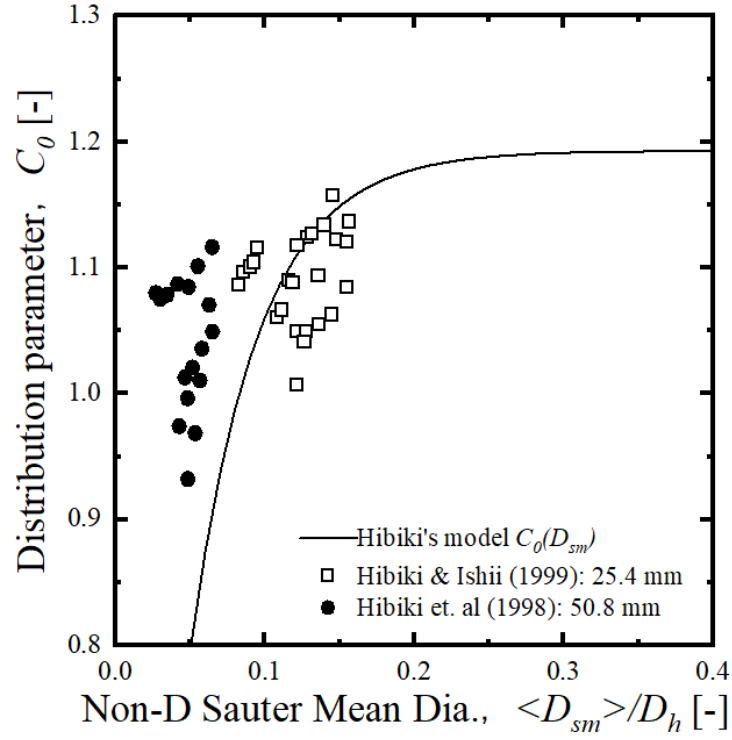
Figure 3.16. The distribution parameter correlation by Hibiki and Ishii (2002) against experimental data (Hibiki et al, 1999, 2001).

Void phase accumulation   Bubble size addition
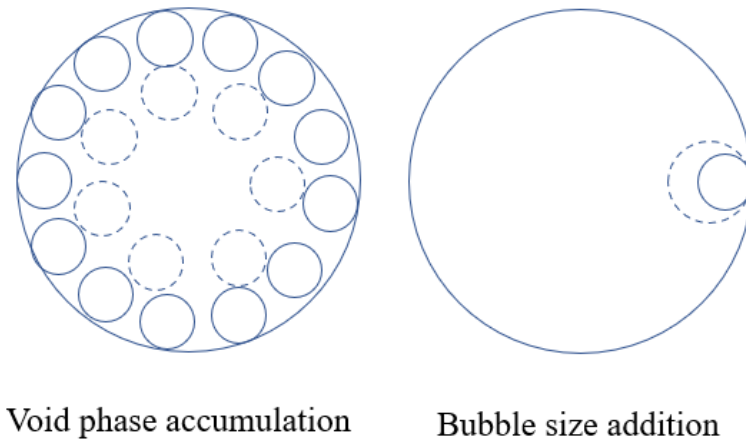
Figure 3.17. To separately consider the influential elements on bubble non-uniform distributions.
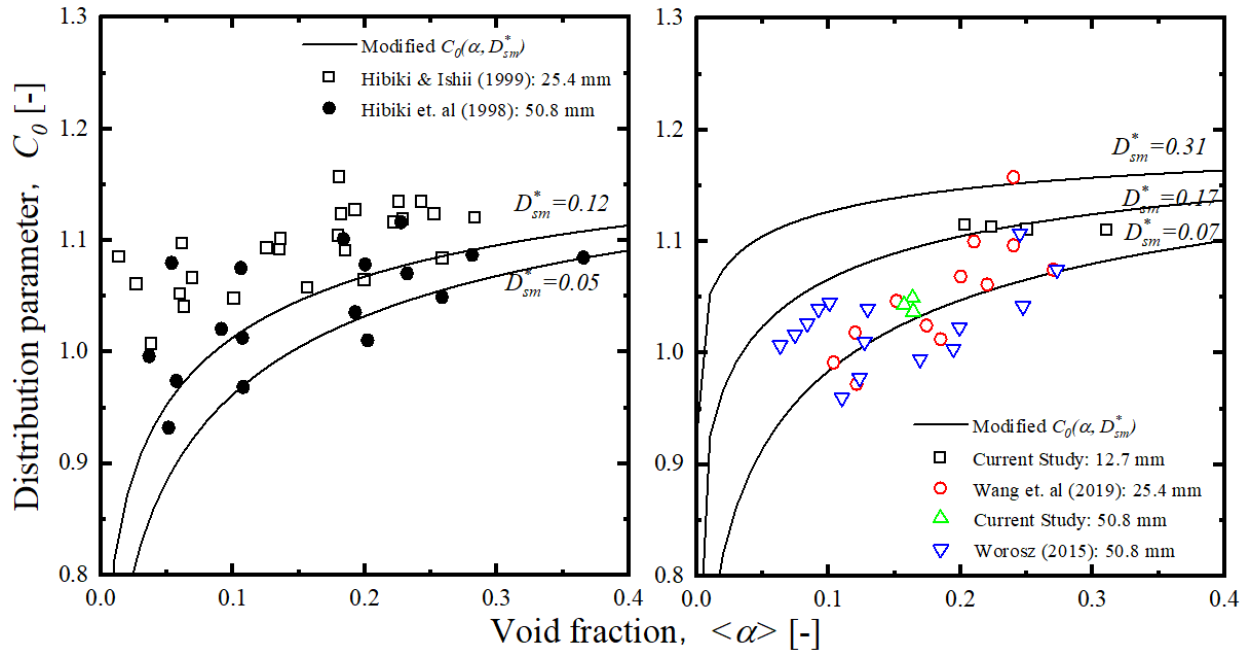
Figure 3.18. Comparison of new-derived distribution parameter correlation with the experimental results.

It has been well proved from the past study [53] that the pipe wall affects the bubble terminal velocity. In this study, the comparison of the measurement results also provides evidence that the velocity of the bubble is more affected by the wall when the pipe size is smaller. Figure 3.19 gives the comparisons of axial bubble velocity obtaining from experiments using different sizes of pipes under the same flow conditions. Noted that the inlet setups of these experiments are highly similar, thus the mixture-injecting effect on the two-phase flows can be negligible. From the results, experimental results show that bubble velocities measured on a smaller diameter pipe are generally smaller than those measured on a larger diameter pipe. Besides, it can also be observed that the wall effect is larger on the 12.7 mm-diameter pipe than on 25.4 mm- and 50.8 mm-diameter pipes.

Based on Clift [53], the terminal velocity ratio $K_u = u_T/u_{T,\infty}$ ($u_{T,\infty}$ is the terminal velocity of the bubble in an infinite medium) can be express as follows,

$$K_u = \left(1 - 2\left(\frac{D_{sm1}}{D_h}\right)^2\right)^{3/2} \tag{3.14}$$

This equation can be applied to the flow condition where Eo < 40. Figure 3.20 depicts the comparison of the adjusted bubble velocities of different pipe sizes using Eq. 3.14. Each point in the figure are generated from the experimental data with similar flow condition (superficial gas and liquid velocity) and measurement position, but collecting on test facilities with different pipe sizes. After adjusted using Eq. 3.14, the bubble velocities on the test loops of different pipe sizes are generally equal with each other.
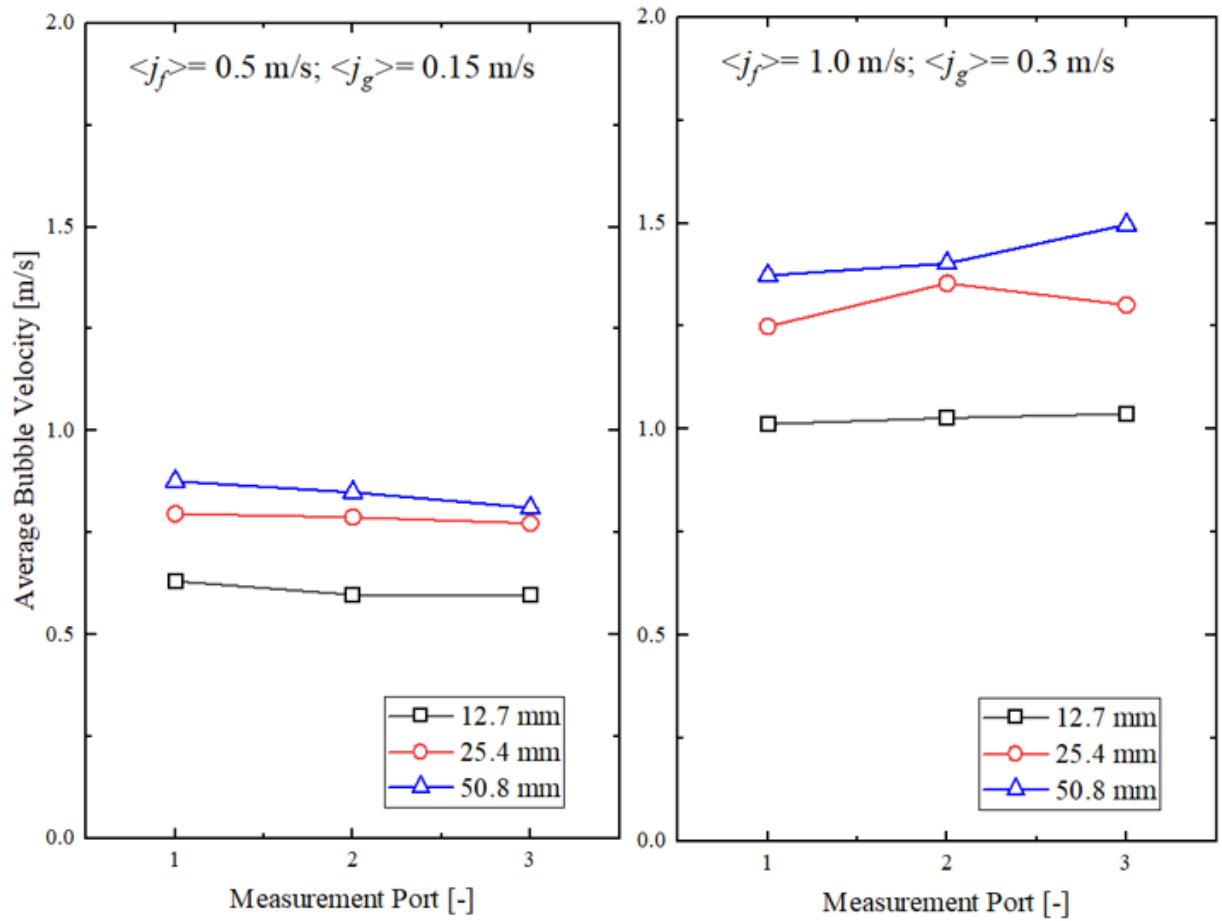
Figure 3.19. Averaged experimental bubble velocities in different sizes of pipes.
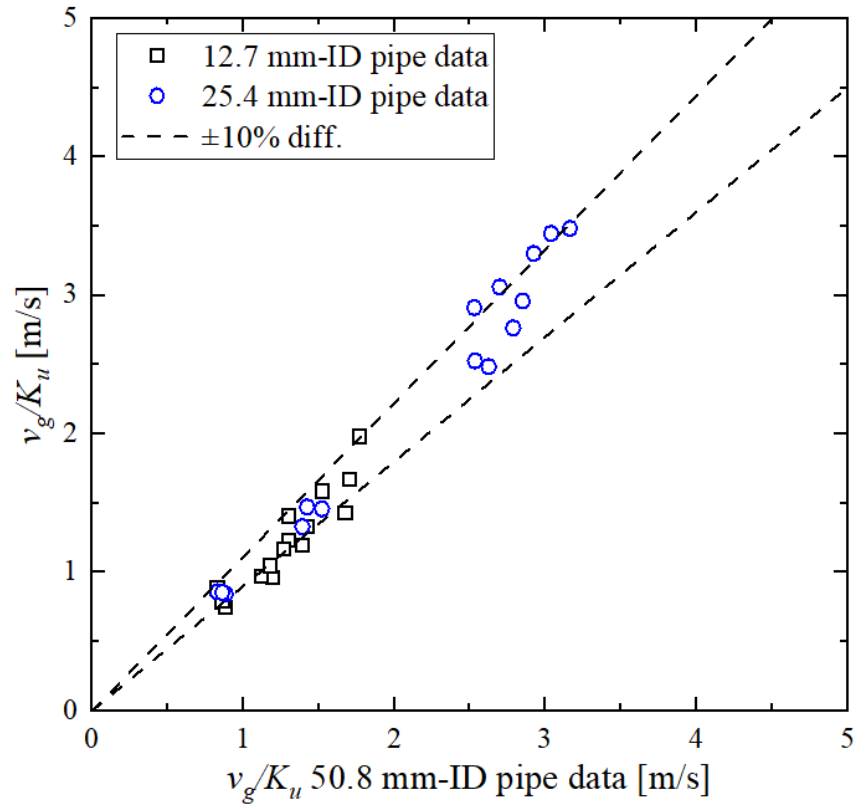
Figure 3.20. Comparison of the adjusted bubble velocities of different pipe sizes.

3.6 Flow Regime Transition

The experimental data shows due to the wake entrainment mechanism, the intensity of the bubble coalescence in a small diameter pipe is higher than in a large diameter pipe. It indicates that the Group-2 bubbles may emerge earlier in a small diameter tube. Therefore, it is important to analyze the pipe wall effect on the bubbly-to-cap-bubbly flow regime transition, namely one-group to two-group flow regime transition.

Figure 3.21 shows the flow regime identification results in 12.7mm, 25.4mm, and 50.8mm ID pipe, as well as the bubbly-to-cap-bubbly flow transition lines. The flow regime identification is realized using the SOM algorithm, described in the previous chapter, as well as flow visualization. Figure 3.22 shows the examples of the typical input signals for different flow regimes included in the experiments. From the results, the bubbly-to-cap-bubbly transition happens at relatively lower void fractions in a smaller diameter pipe. It indicates that in bubbly flow with the same boundary conditions and similar void fraction, small bubbles are in higher probabilities to transform into Group-2 bubbles, in the approach of bubble coalescence. This phenomenon can be explained as in a small diameter circular pipe, the bubble motion in the radial direction is largely restricted by the pipe wall. Therefore, the modeling of the bubbly-to-cap-bubbly flow transition criteria should include the consideration of the pipe wall effect.

In the previous studies, the most commonly-used bubbly-to-cap-bubbly flow transition criterion is developed by Mishima and Ishii [42]. They identified a tetrahedral structure formed by spherical bubbles for bubble packing and coalescence pattern and calculated a critical void fraction as the transition boundary,

$$\alpha_\infty = \left(\frac{2}{3}\right)^3 \approx 0.296 \tag{3.15}$$

Here the subscript ∞ indicates that this model considers the bubble coalescence in an infinity medium without considering the existence of containing wall. However, in a finite space confined by the pipe wall, as discussed in the last paragraph, the motion of the bubble in the radial direction is restricted. This phenomenon can be simplified by classifying the

pipe cross-sectional area into two regions: one is the free zone in the center of the pipe; another one is the near-wall zone, as depicted in figure 3.23. The spherical bubbles in the free zone are regarded as not being affected by the wall and their coalescence pattern can be estimated using Eq. 3.15. The motion of bubbles within the wall zone is largely restricted by the existence of the wall. For simplification, it is assumed that the bubbles within the wall zone will only move towards the free zone and collide with bubbles in the free zone. In this sense, the boundary between the free zone and the wall zone is determined using the mean bubble diameter in the transition flows. From the experimental data, the maximum likelihood of bubble diameter is approximate 1.5 times the Laplace length, as given in the figure. Therefore, a modification factor for the transition boundary model in Eq. 3.15 should be,

$$\lambda_{\text{wall}} = \left(1 - 1.5 \frac{Lo}{D_h} \right)^2 \tag{3.16}$$

where Lo denotes the Laplace length scale. Finally, a bubbly-to-cap-bubbly flow regime transition criterion for vertical upward round pipes can then be written as,

$$\alpha \left(D_h \right) = \alpha_\infty \lambda_{\text{wall}} = 0.296 \left(1 - 1.5 \frac{Lo}{D_h} \right)^2 \tag{3.17}$$

3.7 Chapter Summary

The experimental portion of this work consists of two major efforts: 1) establishing an experimental database on 12.7 mm -diameter pipes in vertical-upward air-water two-phase flow that highlights one-group to two-group transition. 2) systematically investigating the pipe size/wall effect on the interfacial area parameters and transport of two-phase flow. The major findings of the work are summarized as:

- The change in the local void fraction distribution from wall-peak to center-peak is a characteristic phenomenon of the initiation of group transition. The distribution change depends on the amount of void and bubble size.
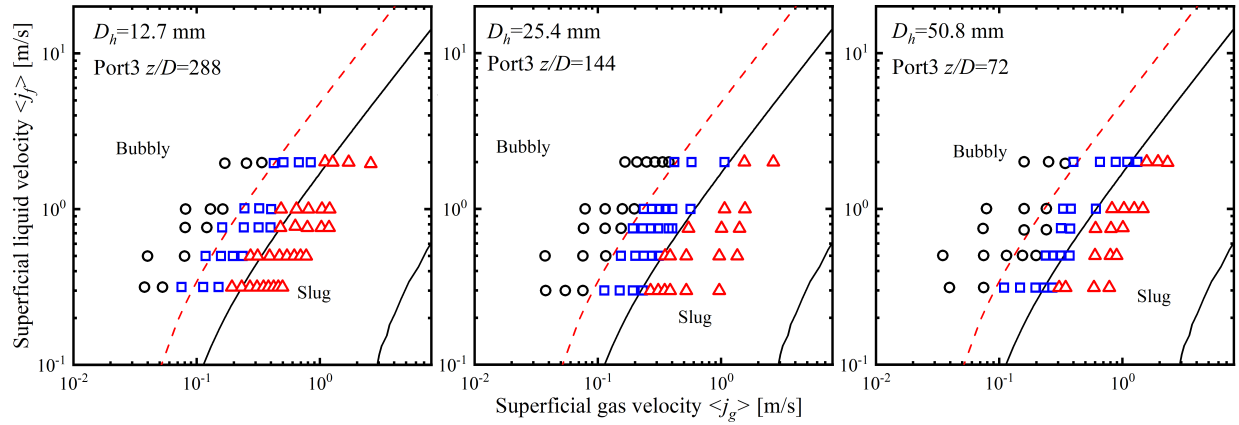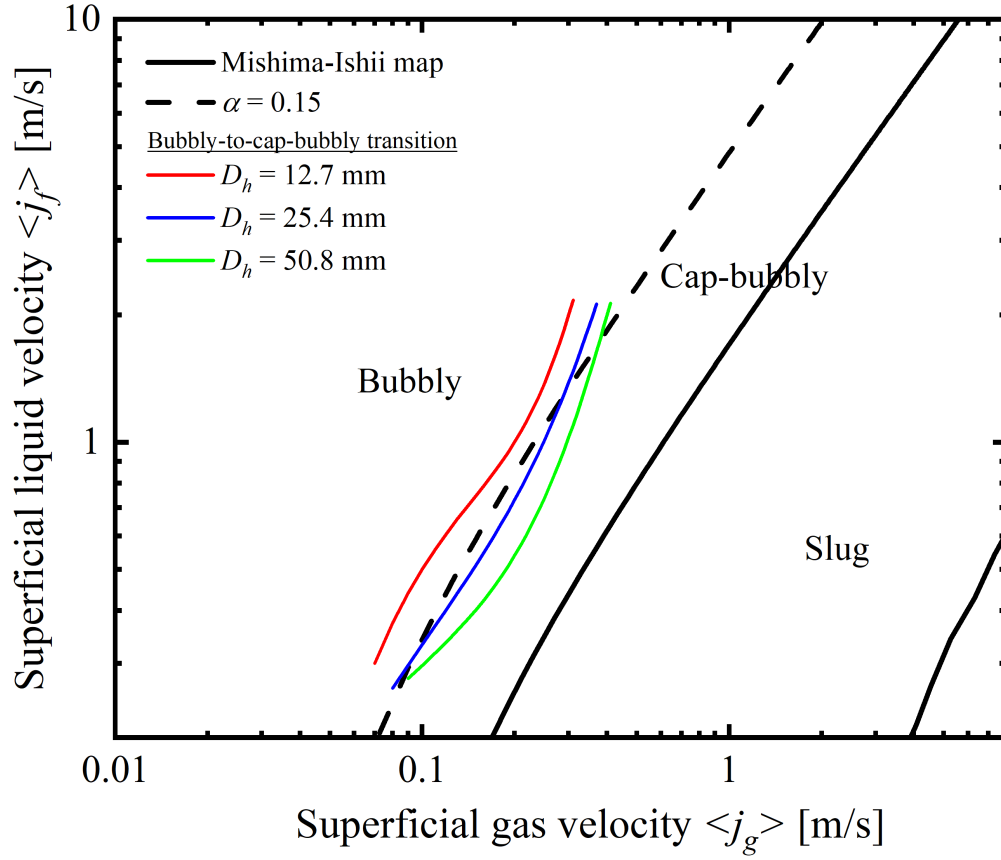
Figure 3.21. One-group to two-group transitions (bubbly-to-cap-bubbly) in different small diameter pipes.
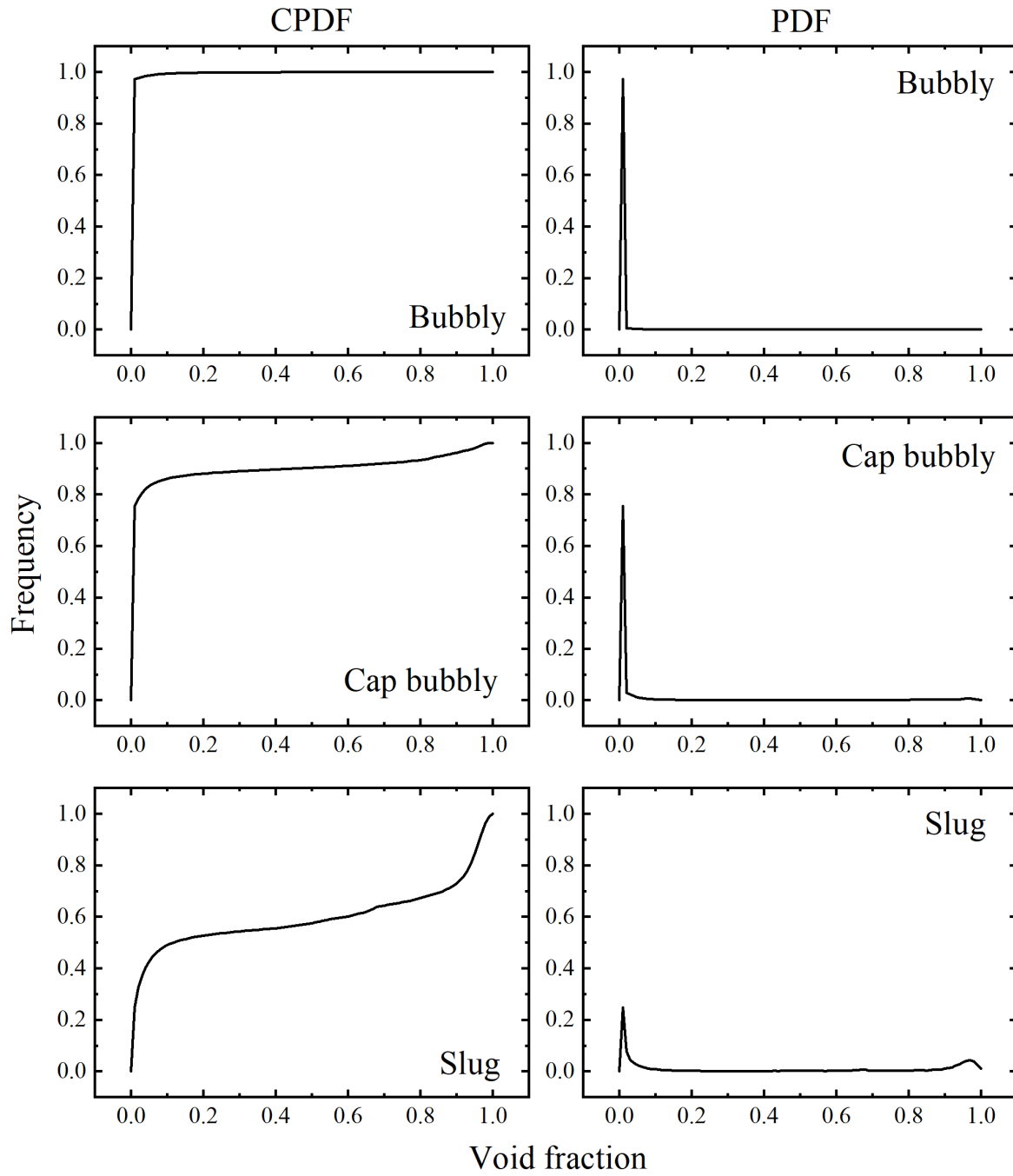
Figure 3.22. Examples of the typical input signals (CPDF and PDF curves) for different flow regimes included in the experiments.
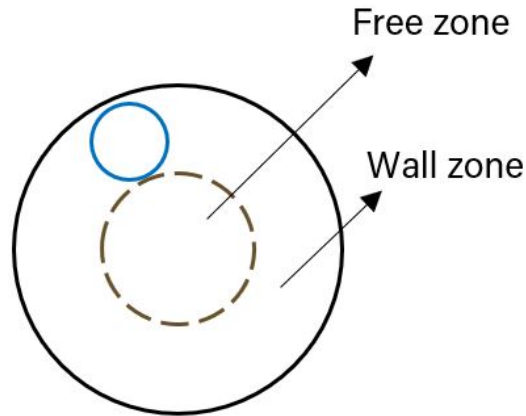
Figure 3.23. Conceptual diagram of bubbles of different zones in the circular pipe cross-sectional area.
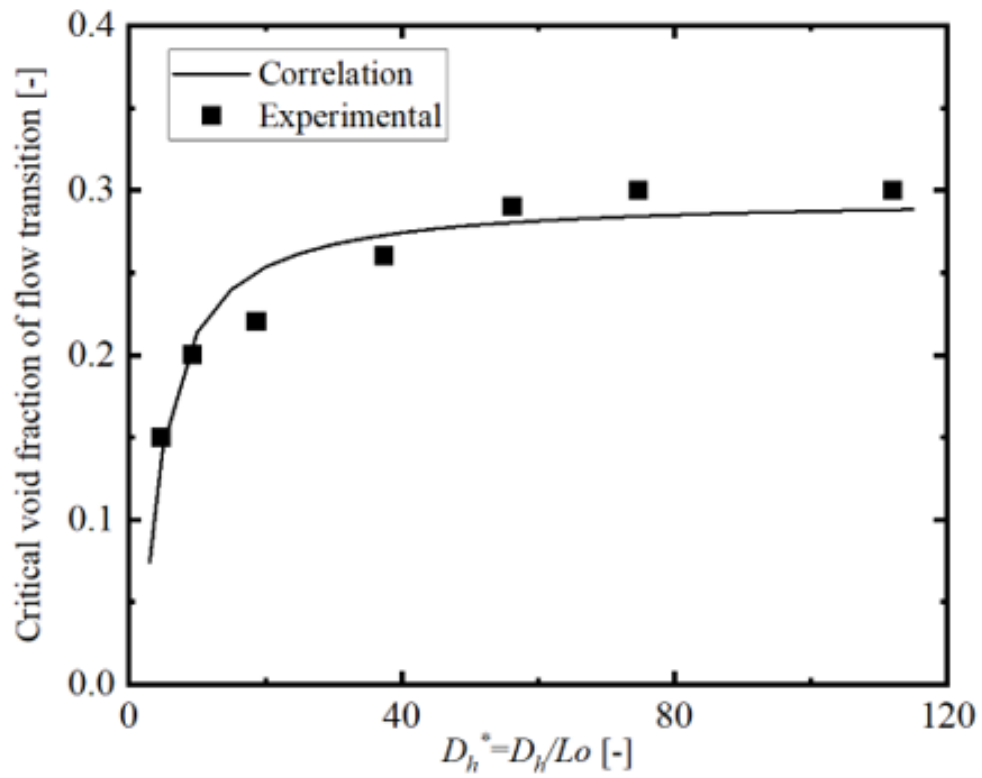

Figure 3.24. Flow regime transition void fractions against experimentally determined critical void fraction of flow transition.

- The distribution parameter in the Drift-flux model that models the void fraction distribution is reformulated based on Ishii's and Hibiki & Ishii's correlation [50], [51]. It considers both the averaged void fraction and the bubble Sauter mean diameter.

- The wall effect on the average bubble velocity is observed by comparing the experimental data with the previous experimental database [14], [33]. It's observed that the wall effect on bubble velocity is non-linear again the pipe size. An adjusting correlation K_u in terms of the non-dimensional bubble Sauter mean diameter is proposed based on the correlation of Clift [53].

- The intensive intergroup transfer on the void fraction and the interfacial area concentration are observed on flow conditions close to bubbly-to-slug transition on the 12.7mm-diameter pipe experiment. This phenomenon also reported in the 25.4mm-diameter pipe experimental [33] but did not appear on the 50.8mm-diameter pipe data. The cause of this phenomenon is due to the constraint of the pipe wall on the bubble motion that the Group-1 bubble can behave as a Group-2 bubble. In this sense, Group-1 wake entrainment to form a Group-2 bubble can be enhanced.

4. MECHANISTIC MODELING OF INTERFACIAL AREA TRANSPORT FOR VERTICAL ROUND PIPES OVER WIDE RANGE OF PIPE DIAMETERS

From the previous experimental study, the interfacial area transport for pipes of different sizes is largely determined by the pipe diameter effect on bubble interaction mechanisms. For the results, in a small diameter pipe, the strong wall effect can enhance bubble coalescence in comparison with bubble disintegration. As a result, the area-averaged interfacial area concentration decreases at a larger rate in a smaller diameter pipe. In this chapter, a detailed discussion on the causes of these phenomena and the physical modelings of the pipe diameter effect on bubble interactions are provided.

4.1 Turbulence beyond Inertia Subrange

One of the most fundamental assumptions made in the development of the bubble interaction source term models is that the size of the turbulent eddies driving the bubble to interact should be in the inertia subrange. This assumption can simplify the modeling by introducing the following properties,

- the turbulence is isotropic

- Turbulent fluctuation velocity can be quantified with $C(\varepsilon D_b)^{1/3}$ where C is a constant and $C = \sqrt{2}$

- Turbulent eddy number density can be estimated with a simple correlation in terms of the eddy size.

The first property indicates the distribution of the turbulence is homogeneous in the carrying phase. Thus, the covariance of dispersed phase and turbulence can be eliminated. The second property quantifies the bubble displacement velocity driven by the turbulence. The last property ensures the turbulence eddy number can be calculated using a explicit

expression. From the study of Azbel and Athanasios [54], the eddy number density with wave number, k_e (inverse proportional to the eddy size) can be expressed as,

$$n_e\left(k_e\right) = N_e\left(k_e\right)\left(1 - \alpha\right) \tag{4.1}$$

where N_e is number of eddies,

$$\frac{\mathrm{d}N_e\left(k_e\right)}{\mathrm{d}k_e} = 0.1k_e^2 \tag{4.2}$$

The from the above two equations, it can be calculated that the relation between the eddy size d_e and the eddy number density n_e is,

$$n_e \propto d_e^{-3} \tag{4.3}$$

The bubble number density can be estimated using the following equation,

$$n_b = \psi\frac{a_i^3}{\alpha^2} \tag{4.4}$$

Since $d_{sm} = 6\alpha/a_i$, the relation between the bubble size (Bubble Sauter mean diameter) and the bubble number density n_b is,

$$n_b \propto d_{sm}^{-3} \tag{4.5}$$

From Eq. 4.3 and Eq. 4.5. Since bubble size and eddy size should be comparable, their corresponding number density should be in the same order of magnitude. Therefore, within the inertia subrange, it is not necessary to consider modeling the eddy number density for the interaction models.

In the conventional bubble coalescence and disintegration modeling, the validation of inertia subrange assumption is by comparing the three different scales: integral length scale k_e, bubble or turbulent eddy scale k_b, and dissipating length scale k_d (i.e. Kolmogorov length scale η) [55]. The criterion should be,

$$k_e \ll k_b \ll k_d \tag{4.6}$$

where $k_e = 2/D_h$ is the wavenumber of the large energy-containing eddies, determined from duct geometry; $k_b = 2/D_b$ is the wave number corresponding to the bubble size; $k_d == 2/\eta$ is the wavenumber of the eddies of viscous dissipation, determined though the viscous layer scale. The three wave numbers should be different in at least one order of magnitude in order to realize Eq. 4.6 [56] For one-group dispersed air-water flow in ambient condition, Eq. 4.6 is usually valid in medium and large diameter pipe, however, k_e and k_d is getting closer in small diameter pipes. This indicates that the bubble size can be in the energy-containing subrange scale and the inertia subrange assumption may not be valid. In this sense, for the existing interfacial area transport models to be able to apply for small diameter pipe flows, the modeling of turbulence eddy density and velocity should be extended to the energy-containing subrange.

Kolmogorov [57] proposed a simple energy spectrum model for the inertia subrange scale,

$$E(k) = C\varepsilon^{2/3}k^{-5/3} \tag{4.7}$$

where ε denotes the turbulent kinetic energy dissipation rate per unit mass and k represents the wave number. Pope [58] proposed another model that aims to expand the Kolmogrov's model into the full energy spectrum,

$$E(k) = C\varepsilon^{2/3}k^{-5/3}f_L(kL)f_\eta(\eta k) \tag{4.8}$$

where $f_L(kL)$ and $f_\eta(\eta k)$ are semi-empirical non-dimensional functions representing the shape of energy containing subrange and the dissipating subrange, respectively. L denotes the integral length scale that is usually the scale of flow channel, and η is dissipation length scale, namely Kolmogorov length scale . $f_L(kL)$ and $f_\eta(\eta k)$ are given by Pope as follows,

$$f_L(kL) = \left\{\frac{kL}{[(kL)^2 + c_L]^{1/2}}\right\}^{5/3+p_0} \tag{4.9}$$

$$f_\eta(k\eta) = \exp\left\{-\beta\left([(k\eta)^4 + c_\eta^4]^{1/4} - c_\eta\right)\right\} \tag{4.10}$$

where p_0 and β are usually specified with constants of 2 and 5.8, respectively. c_L and c_η are adjustable parameters usually determined by the Reynolds number. $f_L(kL)$ and $f_\eta(\eta k)$ are usually approximately equal to 1 when in inertia subrange scale, however, they will be less than 1 when the length scale are in their corresponding subrange scale. The number density of the turbulence eddy can be estimated through the energy balance formulation. For the eddies with their wave numbers ranging from k to $k + dk$, the following formulation in terms of the energy spectrum can be written,

$$\dot{n}_k \rho_c \frac{\pi}{6} d_k^3 \frac{\bar{u}_k^2}{2} dk = E_{\text{spectrum}}(k) \rho_c (-dk) \tag{4.11}$$

where d_k is the eddy size, corresponding to its wave number, and $\dot{n}_k$ and $\bar{u}_k$ are the average eddy number density and eddy fluctuation velocity, respectively. From the Eq. 4.11, the eddy number density is proportional to the energy spectrum, namely proportional to $f_L(kL)$ and $f_\eta(\eta k)$. This means that we could use $f_L(kL)$ to extend the application range of the existing interaction models from the inertia subrange scale to the energy-containing subrange scale.

In order for the $f_L(kL)$ to be used in the IATE interaction models, Eq. 4.9 is re-formulated in terms of the relative bubble size, $f(D_b^*)$,

$$f(D_b^*) = \left(\frac{D_b^{*-1}}{\left[D_b^{*-2} + C_{D_h} \right]^{1/2}} \right)^{\frac{5}{3} + P_0} , \quad D_b^* = \frac{D_b}{D_h} \tag{4.12}$$

where P_0 is a constant and equals to 2. C_{D_h} is also an adjustable parameter in terms of the Reynolds number.

4.2 Bubble Number Density Distribution

Previous studies have proved the validity of using a linear function to approximate the bubble number density distribution. [6], [8], [13] In the present study, the distribution is assumed to follow a linear function distribution that the maximum likelihood of the distribution equals the measured bubble volume with the Sauter mean diameter, named as the

Sauter mean volume V_{sm}. The upper and lower limits are determined as the minimum and maximum diameter that the bubbles in the group can reach. A simple schematic describing the bubble number density distributions is given in Figure 4.1. For the Group-1 bubble number density distribution, the maximum possible diameter is the boundary diameter between the two groups, calculated based on Taylor instability,

$$D_{d,\max} = 4\sqrt{\frac{\sigma}{g\Delta\rho}} \tag{4.13}$$

beyond which the bubble becomes cap in shape and is categorized as a Group-2 bubble. $D_{d,\max}$ is also the lower limit of Group-2 bubble size. However, from the experimental observation, the deviation of the Group-1 bubble size is usually small and away from the critical size $D_{d,\max}$. Therefore, it is assumed that the $V_{max,1}$ is smaller than the volume with critical size $V_c(D_{d,\max})$.

From Kim [4], the bubble distribution function f is defined by,

$$n = \int_{V_{min}}^{V_{max}} f\,dV \tag{4.14}$$

The mean of the bubble size that is greater than V_{sm}, namely leading bubble V_l, $(V_{sm} < V_l < V_{max})$ can be given by,

$$\int_{V_{sm}}^{V_{max}} fV\,dV = \int_{V_{sm}}^{V_{max}} \left[f_{sm} - \frac{f_{sm}}{V_{max} - V_{sm}} \left(V - V_{sm} \right) \right] V\,dV \tag{4.15}$$

The solution of the RHS of Eq. 4.15 is,

$$\int_{V_{sm}}^{V_{max}} fV\,dV = \frac{1}{3} n_{sm} \left(V_{max} + 2V_{sm} \right) \tag{4.16}$$

Since

$$\overline{V_l} = \frac{\int_{V_{sm}}^{V_{max}} fV\,dV}{\int_{V_{sm}}^{V_{max}} f\,dV} \tag{4.17}$$

The mean leading bubble volume can be given by

$$\overline{V_l} = \frac{1}{3} \left(V_{max} + 2V_{sm} \right) \tag{4.18}$$

90

Kim [4] considered two limiting cases where $V_l \to V_{sm}$ and $V_{sm} \to V_{min}$. Assuming $V_{min} \ll V_{max}$, Eq.4.18 can be reformed as,

$$\bar{V_l} \cong C V_{\max} \text{ where } \frac{1}{3} \leq C \leq 1 \tag{4.19}$$

The middle of the range of C, $C = 2/3$, is selected for the further calculation. Therefore,

$$\overline{V_l} = \frac{4}{3} V_{sm} \tag{4.20}$$

Similarly, the mean trailing bubble volume V_l ($V_{min} < V_l < V_{sm}$) can be given by

$$\overline{V_t} = \frac{1}{3} \left(V_{min} + 2V_{sm} \right) \approx \frac{5}{6} V_{sm} \tag{4.21}$$

For group-2 bubble, the maximum bubble size $V_{max,2}$ is characterized by the maximum stable bubble,

$$D_{c,\max} = 40 \sqrt{\frac{\sigma}{g \Delta \rho}} \tag{4.22}$$

Since distortion of Group-2 bubbles is significant, the shape factor and the projected area on the cross-section of the flow channel are important. Typically, Group-2 bubbles are classified as cap bubble and slug bubble. In terms of the cap bubble, the model of its shape is simplified as depicted in figure 4.2(a). The relation between The equivalent cap bubble radius $R_{e,cap}$ and the Sauter mean diameter can be given as,

$$D_{sm,cap} = \frac{6V_{cap}}{A_{cap}} = \frac{6\pi h^2 (R_{e,cap} - h/3)}{4\pi R_{e,cap} h - \pi h^2} \tag{4.23}$$

Since $h = R_{e,cap}(1 - cos(\theta_w))$ and $\theta_w \approx 50^o$, we get $D_{sm} \approx 0.52 R_{e,cap}$. Thus,

$$D_{cap} = 2R_{e,cap} sin(\theta_w) \approx 2.95 D_{sm,cap} \tag{4.24}$$

The above relation represents the projected area of the Group-2 bubble in terms of its Sauter mean diameter. Under the current experimental setup of atmospheric pressure and temperature, $D_c \approx 10.9 mm$. This indicates that a cap bubble may hardly exist in a pipe flow

channel with its inner diameter smaller than 30 mm. Therefore, a slug bubble can directly form, skipping to be a cap bubble.

For a slug bubble that occupies the flow channel, the projected area can be regarded as a circle with its diameter close to the pipe hydraulic diameter, which is $D_{slug} = \lambda_p D_h$. [8] suggested that $\lambda_p = 0.9$. For the shape of a gas slug, the height of the slug is important. To simplify the calculation, it is assumed that the geometrical configuration of a slug bubble consists of a cap head and a cylindrical body, as depicted in figure 4.2(b). The Sauter mean diameter for a slug bubble is given as,

$$D_{sm,slug} = \frac{6V_{slug}}{A_{slug}} = \frac{6\pi h_{head}^2 (R_{e,head} - h_{head}/3) + 0.25\pi D_{slug}^2 h_{body}}{2\pi R_{e,head} h_{head} + 0.25\pi D_{slug}^2 + \pi D_{slug} h_{body}} \tag{4.25}$$

where $D_{slug} = 2R_{e,head} sin\theta_w$, $h_{head} = (1 - cos\theta_w)R_{e,head}$ and $\theta_w \approx 50^o$, Eq. 4.25 becomes,

$$D_{sm,slug} = \frac{0.187 D_{slug} + 1.5 h_{body}}{0.555 D_{slug} + h_{body}} D_{slug} \tag{4.26}$$

From Eq. 4.26, $D_{sm,slug}^* = D_{sm,slug}/D_h$ is bounded in a range of $[0.337\lambda_p, 1.5\lambda_p]$. $D_{sm,slug}^*$ that is smaller than $0.337\lambda_p$ is a spherical-cap bubble. $D_{sm,slug}^*$ that is beyond $1.5\lambda_p$ is due to the shape of the slug is beyond the shape of a ideal slug. Although h_{slug} can be calculated from $D_{sm,slug}$ since Eq. 4.26 is monotonic, it can introduce great errors becuase $D_{sm,slug}$ measured experimentally can be larger than the upper bound of the function $1.5\lambda_p$. Another approach to estimate the h_{slug} is based on the potential flow theory. Based on the study of Mishima and Ishii on slug flow [42], the cross-sectional void fraction of a slug bubble can be estimated as,

$$\alpha_{sl} = \frac{\sqrt{\frac{2gh_{sl}\Delta\rho}{\rho_c}}}{\sqrt{\frac{2gh_{sl}\Delta\rho}{\rho_c}} + (C_0 - 1)j + 0.35\sqrt{\frac{gD_h\Delta\rho}{\rho_c}}} \tag{4.27}$$

Assuming that the entire slug bubble is in cylindrical shape (thereby neglecting the shape of the slug nose) and using the expression for the void fraction of the resulting cylinder, the above equation can be re-written as,

$$D_{slug} = \alpha_{sl}^{0.5} D_h \tag{4.28}$$

92

Since $D_{slug} = \lambda_p D_h$, the above equation is reformulated for h_{slug} as,

$$h_{slug} = \left[\frac{(C_0 - 1)\, j + 0.35 \sqrt{\frac{g \Delta \rho D_h}{\rho_e}}}{0.23 \sqrt{\frac{2g\Delta\rho}{\rho_o}}} \right]^2 \tag{4.29}$$

Based on the study of Kim [4], the expression of a shape factor is given as,

$$\psi \equiv \frac{1}{36\pi} \left(\frac{D_{sm}}{D_e} \right)^3 \tag{4.30}$$

where

$$D_e = \left(\frac{6V}{\pi} \right)^{1/3} \tag{4.31}$$

For a Group-1 bubble, the shape factor is,

$$\psi_1 \equiv \frac{1}{36\pi} \tag{4.32}$$

The shape factor of a Group-2 bubble (either a cap bubble or a slug bubble) is expressed as,

$$\psi_2 \approx \frac{1}{36\pi} \frac{D_{sm}^{*\,3}}{\left(0.187 + 1.5 h_{slug}^* \right)} \tag{4.33}$$

where $h_{slug}^* = \frac{h_{slug}}{D_h}$. Noted that for a cap bubble where $D_{sm}/D_h < 0.337\lambda_p$, $h_{slug}^* = 0$.
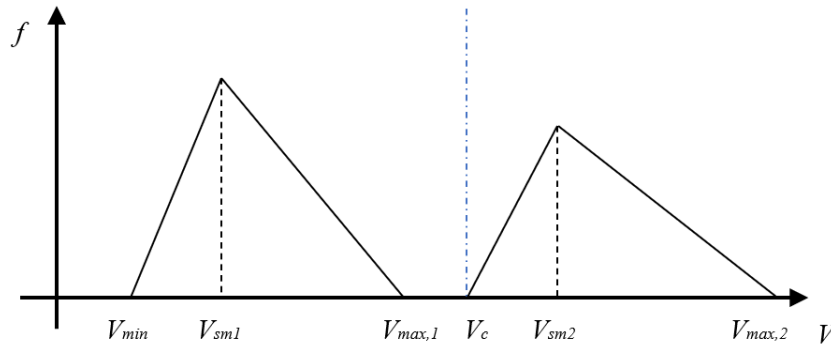
Figure 4.1. Schematic diagram of bubble number density distribution.
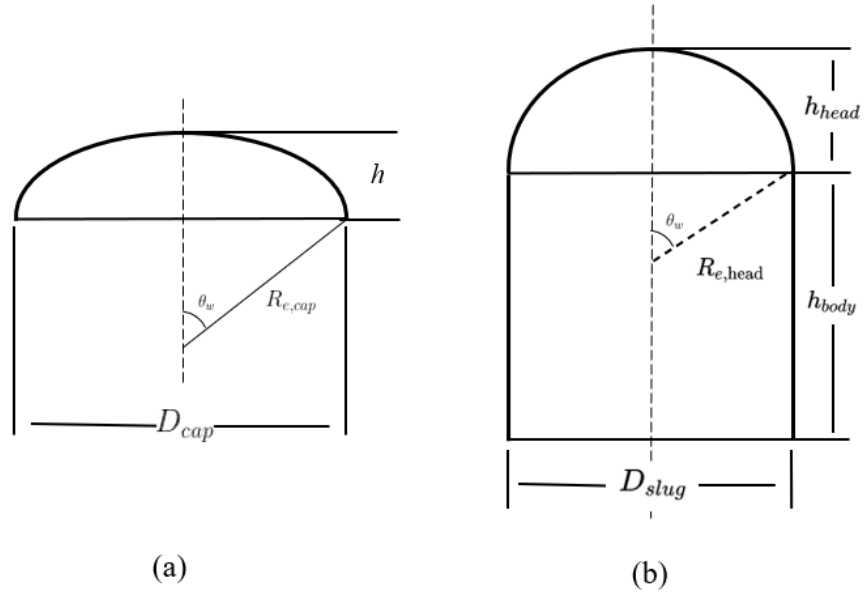
Figure 4.2. Schematic diagram of (a) cap and (b) slug bubble.

4.3 Bubble Coalescence due to Random Collision

In the two-phase flow system, bubbles can coalesce due to random collision driven by turbulence. In the previous researches, the physical-based modeling of this phenomenon considers the collision frequency and the collision efficiency. The collision frequency is modeled with the following two approaches: The modeling of the mean path distance between the two colliding bubbles [3]; the modeling of the average impacting area formed by the two colliding bubbles [55]. Both of the two approaches assume the scales of the bubble and the turbulent eddy size are in the inertia subrange. Therefore, the probability that the bubbles are driven by the turbulent eddy with the comparable size is not modeled. It should be noted here that some of the previous studies [6], [7] claimed that their model includes this consideration by falsely applying the parameter developed by Wu et al. [3], which in reality describes that the collision will not lead to coalescence if two colliding bubble are too far away from each other. The probability that the colliding bubbles are driven by the turbulent eddies with comparable sizes can be re-modeled by considering the availability of the turbulent eddies of such sizes. It can be realized by using the function that extending the inertia subrange assumption to the energy-containing subrange scale, i.e., Eq. 4.12.

Another consideration on the bubble coalescence due to turbulent fluctuation, namely random collision, is the constraints of the existing wall on the bubble motion. In general, for small diameter pipe flows, the motion of bubbles in the transverse direction can be restricted by the pipe wall, whereas bubbles can move more freely in large diameter pipes. Specifically, in terms of the bubble size, the pipe wall constraints to the transverse motion of small Group-1 bubbles can be related to the relative bubble size to the pipe size. For a Group-2 bubble, since it can almost fully cover the whole flow channel cross-sectional area of small and medium diameter pipe, the transverse motion is negligibly small and there is almost no Group-1 bubble in a similar axial position. Besides, the Group-2 bubbles are usually arranged along the axial direction of the flow channel. Therefore, from the above two aspects, Group-2 bubble coalescence due to random collision can hardly happen in a small diameter pipe flow. In contrast, in a large diameter pipe, the situation can be reversed. The bubbles are more aligned in the radial direction, and the wall restriction on the bubble is

reduced. Therefore, the random collision is much likely to happen. Additionally, according to Schlegel [59], the bubble-induced turbulence by relatively large bubbles acting on the transverse direction by the pipe wall. However, in a large diameter pipe, large bubbles tend to be in the center of the flow channel and away from the pipe wall, the bubble-induced turbulence can be produced without the disturbance of the pipe wall. Therefore, although the wall shear-induced turbulence in large diameter pipes is less than that in small diameter pipes, the intensity of turbulence can be stronger than in small diameter pipes. The presence of the large Group-2 bubbles in the flow channel can have a significantly larger effect on small Group-1 bubbles. As a result, the coalescence due to the random collision of Group-1 bubbles, which are free to move in 3-dimensional direction in a large diameter pipe, can be stronger than in a small diameter pipe. In the remainder of this section, the modeling of the random collision mechanism in both small and large diameter pipes is discussed in detail.

4.3.1 Coalescence of Group-1 Bubbles by Random Collision

According to Wu et al. [3], the time needed for two bubble approaching each other driven by turbulence is expressed as,

$$\Delta t = L/u_t \tag{4.34}$$

where L denotes the averaged distance between two colliding bubbles. It is modeled using the dense packing limit,

$$L \approx D_e - \delta D \propto \frac{D}{\alpha^{1/3}} \left[1 - \left(\frac{\alpha}{\alpha_{1,\text{max}}} \right)^{1/3} \right] \tag{4.35}$$

Since this equation is developed for pure bubbly flow, to extend it to two-group flow regimes, the above equation Eq. 4.35 is modified as follows,

$$L \propto \frac{D_{sm1}}{\alpha_1^{1/3}} \left[1 - \left(\frac{\alpha_1}{\alpha_{\text{max}}(1 - \alpha_2)} \right)^{1/3} \right] \tag{4.36}$$

The turbulent fluctuating velocity for Group-1 bubbles is expressed as,

$$u_t = (\varepsilon D_{sm1})^{1/3} \tag{4.37}$$

Based on Wu et al. [3], the random collision probability is considered as,

$$P_\infty^{(1)} \propto \left(\frac{\alpha_1}{\alpha_{1,\max}} \right)^{2/3} \tag{4.38}$$

where α_{max} is the critical void fraction when the center bubble cannot pass through the free space among the neighboring bubbles. The parameter is determined through closest packed structures, hcp or fcc, and with a value of 0.74. The above equation is based on the assumption that the bubbles are moving in an infinite space, namely, bubbles can be towards any direction without restriction. However, This assumption may not be valid near the wall region, as bubbles may less likely to move towards the wall. The population of this kind of bubble is rather small for medium or large diameter pipes but can be large for small diameter pipes. Considering the flow channel diameter effect, this parameter is modified in terms of the bubble radial locations,

$$P_{c,\ new}^{(1)} = \begin{cases} P_\infty^{(1)} & \frac{2r}{D_h} < \frac{\delta D_b}{D_h} \\ (4/3)^{2/3} P_\infty^{(1)} & \frac{2r}{D_h} > \frac{\delta D_b}{D_n} \end{cases} \tag{4.39}$$

where δ is an arbitrary coefficient, and is estimated to be equal to 1.5 based on experimental data. The constant added in the equation is based on the closest packed structures that for any bubble there are 12 closest neighboring bubbles, with 3 in each direction.

Another important aspect to consider is the modeling of collision efficiency. Wu et al. [3] and Kim [4] considered the collision efficiency as a constant for simplification. Later on, Hibiki et al. [16] derived the coalescence efficiency based on the the liquid film thinning model,

$$\lambda_{RC,1} = \exp \left(-C_{RC,1} \frac{D_{sm1}^{5/6} \rho_f^{1/2} \varepsilon^{1/3}}{\sigma^{1/2}} \right) \tag{4.40}$$

Thus, the final form of the coalescence rate for Group-1 bubble is expressed as,

$$
\begin{aligned}
R_{\mathrm{RC}}^{(1)} =& \frac{u_t n_1 P_{c,new}^{(1)}}{L} \lambda_{RC,1} f\left(D_{sm1}^*\right) \\
=& C_{\mathrm{RC}} \left[\frac{u_t n_1 a_{i1}(1-\alpha_2)^{1/3} \lambda_{RC,1} f\left(D_{sm1}^*\right)}{\alpha_{1,\max}^{1/3}\left(\alpha_{1,\max}^{1/3} - \alpha_1^{1/3}\right)} \right] \\
& \times \left[1 - \exp\left(-C \frac{\alpha_{1,\max}^{1/3}\alpha_1^{1/3}}{\alpha_{1,\max}^{1/3} - \alpha_1^{1/3}} \right) \right]
\end{aligned}
\tag{4.41}
$$

The interfacial area change of Group-1 bubble due to the coalescence of Group-1 bubbles by random collision is modeled by assuming the two colliding bubbles are in the averaged Group-1 bubble diameter of D_{sm1}. In this case, two situations could exist: 1) two relatively small Group-1 bubbles collide and form a larger Group-1 bubble; 2) two relatively large Group-2 bubbles collide and form a Group-2 bubble. It is noted that although the situation exists that one small and one large Group-1 bubbles collide and form a Group-2 bubble theoretically, however, this situation is quite less likely to happen so it is neglected. The interfacial area change in the two situations is calculated based on the bubble number density distribution function. Firstly, the probability that two large Group-1 bubbles collide and form a Group-2 bubble is estimated. The bubble boundary diameter that defines the relative size of the Group-1 bubble is around 0.8 times of the $D_{d,max}$, which corresponds to the volume of 0.512 times of $V_{d,max}$. As a result, the percentage of bubble that is greater than $0.512 V_{d,max}$ interfacial area change is expressed as,

$$
p_{c1} = \begin{cases} 0.238(1 - V_{sm1}^*)^{-1} & V_{sm1}^* \leq 0.512 \\ 1 - 0.262 V_{sm1}^{*-1} & V_{sm1}^* > 0.512 \end{cases}
\tag{4.42}
$$

Thus, for situation 1, the interfacial area change is calculated by the average Group-1 bubble interfacial area change weighted by the bubble size smaller than bubble boundary diameter described above,

$$
\begin{aligned}
(\Delta A_i)_{RC,1}^{(1,1)} &= -0.413 \times 0.64(1 - p_{c1})^2 \frac{1}{\phi_1}\left(\frac{a_1}{a_{i,1}}\right)^2 \\
&= -0.264(1 - p_{c1})^2 \frac{1}{\phi_1}\left(\frac{a_1}{a_{i,1}}\right)^2
\end{aligned}
\tag{4.43}
$$

98

In the case that two large Group-1 bubbles collide and form a larger Group-2 bubble, the average change of Group-1 interfacial area weighted by the bubble size larger than bubble boundary diameter,

$$
\begin{aligned}
(\Delta A_i)^{(11,2)}_{RC,1} &= -2 \times 3.24 p_c^2 \frac{1}{\phi_1} \left(\frac{a_1}{a_{i,1}} \right)^2 \\
&= -6.48 p_c^2 \frac{1}{\phi_1} \left(\frac{a_1}{a_{i,1}} \right)^2
\end{aligned}
\tag{4.44}
$$

The interfacial area change of Group-2 bubble per iteration can be correspondingly obtained,

$$
\begin{aligned}
(\Delta A_i)^{(11,2)}_{RC,2} &= 1.58 \times 3.24 p_c^2 \frac{1}{\phi_2} \left(\frac{a_1}{a_{i,1}} \right)^2 \\
&= 5.12 p_c^2 \frac{1}{\phi_2} \left(\frac{a_1}{a_{i,1}} \right)^2
\end{aligned}
\tag{4.45}
$$

4.3.2   Coalescence of Group-1 and Group-2 Bubbles by Random Collision

As discussed earlier in this section, the coalescence of the Group -2 bubble due to random collision is largely limited by the pipe size. In a small diameter pipe, since the bubble size is large enough to cover the whole flow channel area, small bubbles tend to exist in front or behind the large bubbles. The coalescences between small and large bubbles are more likely driven by wake entrainment instead of random collision. Thus, the modelings of the coalescence of the large bubble due to the random collision are usually neglected in small diameter pipes. The random collision source terms are only considered and modeled in large diameter pipes. [7], [59]. Therefore, similar to the approach used in Group-1 bubbles that comparing the sizes of pipe cross-sectional area and the bubbles can also be used for Group-2 bubble interactions. The coalescence of Group -1 and Group -2 Bubble by random collision is modeled in a similar form as the Group -1 bubble random collision mechanism. However, since the size of Group -2 bubble are much larger than that of Group -1 bubble, the averaged distance between two colliding bubbles L is modeled based on the Group-2 bubble size,

$$
L \approx D_{e,2} - \delta D_1 \approx D_{e,2} \propto \frac{D_{sm2}}{[(1 - \alpha_1)\alpha_2]^{1/3}}
\tag{4.46}
$$

The turbulent fluctuation velocity in this case would be in terms of the Group-2 bubble,

$$u_{t2} = (\varepsilon D_{sm2})^{1/3} \tag{4.47}$$

The estimated collision probability follows the expression given by Sun [6] and Smith [7],

$$P_{RC}^{(12)} \propto \alpha_1^{2/3} \alpha_2 \tag{4.48}$$

The collision efficiency is given as,

$$\lambda_{RC,122} = \exp\left(-C_{RC,122}\frac{D_{sm2}^{5/6}\rho_f^{1/2}\varepsilon^{1/3}}{\sigma^{1/2}}\right) \tag{4.49}$$

Thus, the final form of the coalescence rate for Group-1 and Group-2 bubble is expressed as,

$$
\begin{aligned}
R_{RC}^{(12,2)} &= \frac{u_{t2}n_t}{L}P_{RC}^{(12)}\lambda_{RC,122}f\left(D_{sm2}^*\right) \\
&= C_{RC}^{(12,2)}u_{t2}n_t\alpha_1^{2/3}\alpha_2^{1/3}a_{i2}(1-\alpha_1)^{1/3}\lambda_{RC,122}f\left(D_{sm2}^*\right)
\end{aligned}
\tag{4.50}
$$

The estimation of the interfacial area and volume change of each group are based on the work of Worosz [14], they are given as:

$$(\Delta A_i)_{RC,1}^{(12,2)} = -\frac{1}{\psi_1}\left(\frac{\alpha_1}{a_{i1}}\right)^2 \tag{4.51}$$

$$(\Delta A_i)_{RC,2}^{(12,2)} = \frac{2}{3\psi_2}\left(\frac{D_{sm1}}{D_{sm2}}\right)^3\left(\frac{\alpha_2}{a_{i2}}\right)^2 \tag{4.52}$$

$$(\Delta V)_{RC,1}^{(12,2)} = -\frac{1}{\psi_1}\left(\frac{\alpha_1}{a_{i1}}\right)^3 \tag{4.53}$$

4.3.3 Coalescence of Group-2 Bubbles by Random Collision

The modeling of Group-2 bubble random collision is similar to the previous approach. The averaged distance between two colliding bubbles L is modeled based on the Group-2 bubble size,

$$L \approx D_{e,2} - \delta D_2 \propto \frac{D_{sm2}}{(1-\alpha_1)^{1/2}\alpha_2^{1/2}} \tag{4.54}$$

The estimated collision probability was modeled by Smith [7] by considering the relative diameter of the Group-2 bubble and the pipe size,

$$P_{RC}^{(2)} \propto \left(\frac{D_{b2}}{D_h}\right)^{2/3} \tag{4.55}$$

Here, the D_{b2} cannot be simply replaced by D_{sm2}, since numerically D_{sm2} could be greater than D_h. This will make the $P_{RC}^{(2)}$ greater than one. Therefore, to avoid this problem, the approach of using void fractions that is similar to Wu et al.'s method is used,

$$P_{RC}^{(2)} \propto \left(\frac{\alpha_2}{\alpha_{2,\max}}\right)^{2/3} \tag{4.56}$$

where the $\alpha_{2,\max}$ is the critical void fraction that is close to the dense packing limit. Assuming the Group-2 bubbles are all in cylindrical shape, the closest packing fraction of cylinders is the densest ordered packing of circles in 2D, which is $(\pi/6)\sqrt{3} = 0.9069$. The $\alpha_{2,\max}$ is set as 0.85. Besides, the collision efficiency is estimated as,

$$\lambda_{RC,2} = 1 - \exp\left(-C_{RC2}\alpha_2^{1/2}\right) \tag{4.57}$$

Thus, the final form of the coalescence rate for Group-1 and Group-2 bubble is expressed as,

$$\begin{aligned} R_{RC}^{(2)} &= \frac{u_{t2}n_2}{L}P_{RC}^{(2)}\lambda_{RC,2}f\left(D_{sm2}^*\right) \\ &= C_{RC}^{(2)}u_{t2}n_2\alpha_2^{1/6}\alpha_{max,2}^{-2/3}a_{i,2}(1-\alpha_1)^{1/2}\lambda_{RC,2}f\left(D_{sm2}^*\right) \end{aligned} \tag{4.58}$$

The interfacial area change of the Group-2 bubble due to the random collision can simply be modeled by considering the surface area reduction when two Group-2 bubbles with the

average size of all Group-2 bubbles, V, collide and form a larger bubble with its size of 2V. The interfacial area change can be estimated as,

$$(A_i)_{RC,2}^{(2)} \approx -0.413 \frac{1}{\psi_2} \left(\frac{\alpha_2}{a_{i2}} \right)^2 \tag{4.59}$$

4.4 Coalesence Due to Entrainment in the Wake Region of a Leading Bubble

Similar to random collision, the wake entrainment can also be considered to be caused by turbulence, which is induced by bubbles. A bubble that generates turbulence is called a leading bubble, while the bubble that encounters the bubble-induced turbulence is called a trailing bubble. The area of the liquid phase that is impacted by the leading bubble is called a wake region. For small diameter pipes, wake entrainment is the dominant bubble interaction mechanism since the lateral fluctuation of bubbles is small, and it is an important influential factor for the bubbly-to-slug, and slug-to-churn transitions. Hibiki et al. [60] also pointed out that the wake entrainment can be stronger in relatively low velocity conditions. However, when the flow velocities are relatively high, the trailing bubbles can easily escape from the wake regions due to the liquid turbulence. This can reduce the wake entrainment coalescence rate. However, in the previous modelings of wake entrainment, the trailing bubbles within the wake region were assumed to absolutely collide with the leading bubble, and the flow velocity effect on the wake entrainment was not considered.

In terms of the pipe diameter, as already discussed in the previous chapter, the existence of pipe walls in a small diameter pipe can force the bubbles aligned along with the axial position. Thus, wake entrainment is the dominating bubble coalescence mechanism and the important factor for the flow regime transitions. For large diameter pipes, the liquid turbulence is usually larger since the containing pipe diameter effect on reducing the liquid turbulence is weaker. The trailing bubbles can have more space and more driven energy to escape from the wake region. In this case, bubble coalescence due to wake entrainment may not be as strong as in small diameter pipes. The modeling of wake entrainment consists of three cases: Group-1 bubbles are entrained and collide with a leading Group-1 bubble;

Group-1 bubbles are entrained and collide with a leading Group-2 bubble; two Group-2 bubbles collide due to wake entrainment.

4.4.1 Transition function for one-group to two-group bubble flows

Through the experimental analysis in Chapter 4, the bubble coalescence due to wake entrainment is enhanced when the pipe cross-sectional area is small. The criteria in terms of void fraction and bubble diameter on determining this intensive bubble coalescence behavior are derived based on the geometrical relations between the dispersed gas phase and the pipe cross-sectional area. A continuous function in terms of these criteria should be developed and applied to the wake entrainment models, namely transition function. This function $T(D_{sm}, \alpha)$ is designed as,

$$
\begin{aligned}
T\left(D_{sm}, \alpha\right) &= a + \frac{(1 - 2a)}{(1 + e^{-g(D_{sm})})(1 + e^{-h(\alpha)})} \\
g(D_{sm}) &= \frac{(D_{sm} - max[D_{tr}, D_{re}])}{\beta D_c} \\
h(\alpha) &= \frac{(\alpha - \alpha_{tr})}{\beta}
\end{aligned}
\tag{4.60}
$$

where a and β are adjustable parameters determined through the experiments. This transition function is developed based on the Sigmoid function ($S(x) = 1/(1 + e^{-x})$). Fig. 4.3 shows an example of the transition function when $max[D_{tr}, D_{re}] = 4mm$ and α is greater than α_{tr}. In the model prediction for real cases, these parameters are calculated based on the boundary conditions.

The transition function is designed to be applied to the models of bubble coalescing rate due to wake entrainment by simply being multiplied with the current models,

$$
R_{WE}^{(11,2)} \rightarrow R_{WE}^{(11,2)} T\left(D_{sm}, \alpha\right)/a
\tag{4.61}
$$

The above equation assumes that the Group-1 bubble size is the same, which is also utilized in Worosz's approach [14]. This assumption is valid in the adiabatic air-water experiment, based on the experimental observation. Whereas in the boiling two-phase flow, such as
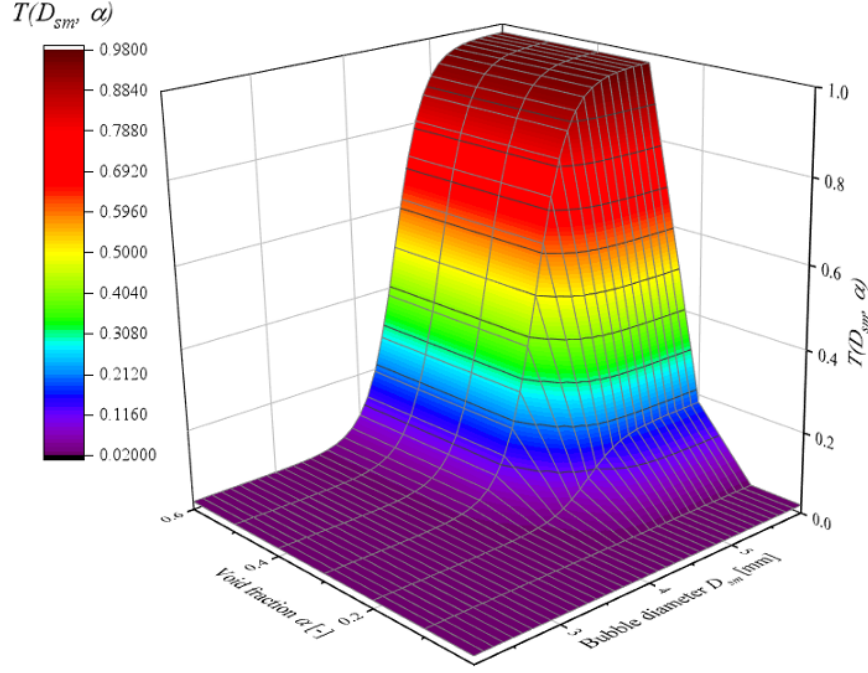
Figure 4.3. The newly-proposed transition function $T(D_{sm})$ with $A = 0.02$, $max[D_{tr}, D_{re}] = 4mm$, and $\beta = $ 9e-3. $\alpha_{tr} = 0.216$.

subcooled boiling convective flows, this assumption is not valid as the size of the Group-1 bubbles varies a lot due to the existence of phase change. However, the transition function could also be used to only the leading bubbles if the bubble number density distribution is specified.

4.4.2 Group-1 Bubble Coalescence due to Wake Entrainment

From the studies of Wu et al. [3] and Kim [4], the number of bubbles inside the cylindrical-like wake region is expressed as,

$$N_{\mathrm{w}} = V_{\mathrm{w}} n_t \propto D^2 \left(L_{\mathrm{w}} - \frac{D}{2} \right) n_t \tag{4.62}$$

where n_l denotes the trailing bubble number density. Assuming that the average time interval for a bubble in the wake region to catch up with the preceding bubble is ΔT, the collision rate per unit mixture volume should satisfy,

$$R_{\text{WE}} \propto n_l \frac{N_{\text{w}}}{\Delta T} \approx D^2 n_l n_t \left(\frac{L_{\text{w}} - D/2}{\Delta T} \right) \approx D^2 n_l n_t \bar{u}_{\text{rw}} \tag{4.63}$$

where $\bar{u}_{\text{rw}}$ is the average relative velocity between the leading bubble and the bubble in the wake region. It can be approximated in terms of the relative velocities of the continuous medium inside and outside the wake region,

$$\bar{u}_{\text{rw}} = \overline{U_f(z) - K_u U_\infty} \tag{4.64}$$

where k_U is discussed and defined in the previous chapter with Eq. 3.14.

Kim [4] adopted the analytical expression developed by Schlichting [61] to estimate the bubble relative velocity in the wake region. For a turbulent wake around a spherical body, the velocity inside the wake, u_{w} can be expressed as,

$$u_w = U(z) - K_u U_\infty \propto K_u U_\infty \left(\frac{C_D A}{z^2} \right)^{1/3} \tag{4.65}$$

Eq. 4.64 can be approximated using Eq. 4.65,

$$U_f(z) - K_u U_\infty = K_u u_r C_D^{1/3} \left(\frac{D_b/2}{z} \right)^{2/3} \tag{4.66}$$

The average relative velocity inside the wake region can be obtained as

$$\bar{u}_{rw} = K_u u_r C_D^{1/3} \left[\frac{3 D_b/2}{L_w - D_b/2} \right] \left(\left(\frac{L_w}{D_b/2} \right)^{1/3} - 1 \right) \tag{4.67}$$

Let a dimensionless length L_w^* represent L_w,

$$L_w^* = \frac{L_w}{D_b/2} \tag{4.68}$$

Eq. 4.67 becomes,

$$\bar{u}_{rw} \propto K_u u_r C_D^{1/3} \frac{\left(L^{*1/3} - l\right)}{(L^* - l)} = K_U u_r C_D^{1/3} f(L^*) \tag{4.69}$$

In terms of the coalescence efficiency $\lambda_{WE,1}$, Hibiki et al. [62] used the same expression of the coalescence efficiency due to random collision. So far, the coalescence rate due to the wake induced entrainment mechanism is given by,

$$R_{WE,1} = C_{WE}^{(1)} C_D^{1/3} n_l n_t D_b^2 K_u u_{r1} \lambda_{WE,1} \tag{4.70}$$

The leading and trailing bubble number density is estimated using the bubble number distribution function. An arbitrary coefficient can be used. Therefore, the bubble number density is expressed as,

$$n_l n_t = \beta_{lt} n_1^2 \tag{4.71}$$

β_{lt} is obtained from the bubble number density distribution, which is presented in the previous section. As stated before, the size of the leading bubble is no smaller than that of the trailing bubble. Besides, the number of the trailing bubble should at least be equal to that of the leading bubble. Therefore, Eq. 4.71 is expressed as,

$$\beta_{lt} = \sum_{D_t = D_{min}}^{D_{sm}} \sum_{D_l = D_{sm}}^{D_{max}} \frac{\phi(D_l) \phi(D_t)}{\left[\Phi(D_{max}) - \Phi(D_{min})\right]^2} \approx 0.165 \tag{4.72}$$

where D_l and D_t are the diameters of leading bubbles and trailing bubbles, respectively. D_{max} and D_{min} are the maximum and minimum diameters of the group 1 bubble can reach. Eq. 4.72 indicates that given the bubble number density distribution in this study, β_{lt} is a constant value.

The relative velocity u_{r1} is derived by Kim [4] based on the study by Ishii and Chawala [63], where the void fraction and the bubble size are considered,

$$u_{r1}(D_b) = \sqrt{\frac{g D_{sm1} \Delta \rho}{3 C_{D1} \rho_f}} \tag{4.73}$$

where C_{D1} is given by,

$$C_{D1} \approx 2.4 \frac{1}{\text{Re}_{D_{sm1}}^{1/4}} = 2.4 \left(\frac{v_f}{(1-\alpha)u_{r1}D_{sm1}} \right)^{1/4} \tag{4.74}$$

Finally, the intergroup transfer caused by Group-1 wake entrainment should be considered by including the transition function developed in the last section. Combine the equations above, the final form of the Group-1 coalescence rate due to the wake induced entrainment mechanism is given by,

$$R_{WE}^{(1)} = C_{WE}^{(1)} C_{D1}^{1/3} n_1^2 D_{sm1}^2 K_u u_r \lambda_{WE,1} T\left(D_{sm}, \alpha\right) \tag{4.75}$$

Similar to Group-1 bubble random collision, the coalescence of Group-1 bubble can create either Group-1 bubbles or Group-2 bubbles. In the case that Group-2 bubbles are created, the estimation of interfacial area and volume change due to wake entrainment follows the idea by Worosz [14]: the generation of a Group-2 bubble as the result of an evolutionary process that consists of a series of successive coalescence interactions between a large Group-1 bubble and many trailing bubbles. However, Worosz assumes that all the Group-1 bubbles are in the same size, and this study proposes that the bubble number density distribution follows the linear function distribution. Thus, modification is needed to obtain the ΔA_i and ΔV.

Consider a leading Group-1 bubble with a size of $V_l(D_l)$. The trailing Group-1 bubbles should have sizes no bigger than the leading bubble $S = \{V_t(D_t) \in G1 | V_t(D_t) < V_l(D_l)\}$. The critical bubble can be obtained when the leading bubble coalesce with N trailing bubble with size of $\bar{D}_t$,

$$NV(\bar{D}_t) + V(D_l) -> V(D_c) \tag{4.76}$$

It can be convenient to approximate $\bar{D}_t$ and $\bar{D}_t$ with respect to D_{sm}. From section 4.1, we obtain that $\bar{V}_l \approx 4/3 V_{sm}$ and $\bar{V}_t \approx 5/6 V_{sm}$. let $D_{sm}^* = D_{sm}/D_c$, the above equation becomes,

$$\bar{N} = \frac{V_c - V_l}{V_t} \approx 1.2 \left(D_{sm}^*\right)^{-3} - 1.6 \tag{4.77}$$

Consider in the real case, there should be at least one coalescence before a Group-2 bubble is produced. To eliminate the singularity, Eq. 4.77 is reformed as

$$\bar{N} = max \left[1, 1.2 \left(D_{sm}^*\right)^{-3} - 1.6\right] \tag{4.78}$$

The rate of change of Group-2 interfacial area due to the coalescence of Group-1 bubbles by wake entrainment can be obtained by dividing the area of generated Group-2 bubbles by the number of iteration,

$$(\Delta A_i)_{WE,2}^{(11,2)} = \frac{1}{N} \sum_{j=1}^{\bar{N}} (\Delta A_i)_{2j} = \frac{A_{ic}}{\bar{N}} = \frac{(36\pi)^{1/3}\varphi_c V_c^{2/3}}{\bar{N}} \tag{4.79}$$

let $V_c = \pi D_c^3/6$, $D_{sm} = 6\alpha/a_i$, $\psi_1 = 1/36\pi$, $D_{sm}^* = D_{sm}/D_c$, the above equation becomes,

$$(\Delta A_i)_{WE,2}^{(11,2)} = \frac{1}{\psi_1} \left(\frac{\alpha_1}{a_{i1}}\right)^2 \left(\frac{\varphi_c}{\bar{N}} D_{sm1}^*\right) \tag{4.80}$$

φ_c (equals to $(\varphi_1 + \varphi_2)/2 = 1.3$) is the mixed shape factor used by Worosz [14], The average change of Group-1 interfacial area can be obtained by dividing the total area of coalesced Group-1 bubbles at the **final** stage by the total number of iteration,

$$(\Delta A_i)_{WE,1}^{(11,2)} = -\frac{A_t + A_{l,n-1}}{N} = -\frac{(0.833 N_{WE} + 0.5)^{2/3} + 0.886}{N_{WE}\psi_1} \left(\frac{\alpha_1}{a_{i1}}\right)^2 \tag{4.81}$$

The change of Group-1 void fraction per iteration can be correspondingly obtained,

$$(\Delta V_i)_{WE,1}^{(11,2)} = -\frac{V_t + V_{l,n-1}}{N} = -\frac{N V_t + V_l}{N} = -\frac{1}{\psi_1} \left(\frac{\alpha_1}{a_{i1}}\right)^3 \left(0.83 + \frac{1.33}{N}\right) \tag{4.82}$$

In the case that Group-2 bubbles are created, the coalescence only causes interfacial area change within Group-1. The interfacial area change can be calculated based on the average leading and trailing bubble sizes,

$$(\Delta A_i)_{WE}^{(1)} = A_i(V_l + V_t) - A_i(V_t) - A_i(V_t) = -0.423 \frac{1}{\psi_1} \left(\frac{\alpha_1}{a_{i1}}\right)^2 \tag{4.83}$$

4.4.3 Group-1 and Group-2 Bubble Coalescence due to Wake Entrainment

In the case that Group-1 and Group-2 bubbles coalesce and get larger Group-2 bubbles due to wake entrainment, the interaction rate is firstly modified by considering the leading and trailing bubble number density. From Worosz [14], Group-1 bubble cannot present in the area where Group-2 bubbles exist, and vice versa. In this sense, the leading and trailing bubble number density in this situation is expressed as,

$$n_l n_t = \frac{n_1 n_2}{(1 - \alpha_1)(1 - \alpha_2)} \tag{4.84}$$

From the study of Sun [6], different coeffcients for the Group-2 relative velocity are used with different Group-2 bubble sizes. From section 4.1, the relation between cap bubble diameter and the Sauter mean diameter is $D_{cap} = 2.96 D_{sm2}$. Therefore, based on the study of Brooks et al. [64], the relative velocity u_{r2} is given as,

$$u_{r2} = \begin{cases} 0.54 \sqrt{\frac{g D_h \Delta \rho}{\rho_f}} (1 - \langle \alpha_2 \rangle)^{1/2} & (2.96 D_{sm2} > D_h) \\ 0.93 \sqrt{\frac{g \langle D_{\mathrm{Sm2}} \rangle \Delta \rho}{\rho_f}} (1 - \langle \alpha_2 \rangle)^{1/2} & (2.96 D_{sm2} \leq D_h) \end{cases} \tag{4.85}$$

The coalescence rate between Group-1 and Group-2 bubbles due to the wake entrainment mechanism is expressed as,

$$R_{WE}^{(12,2)} = C_{WE}^{(12,2)} C_{D2}^{1/3} \lambda_{WE,122} \frac{n_1 n_2 D_{b2}^2 u_{r2}}{(1 - \alpha_1)(1 - \alpha_2)} \tag{4.86}$$

The interfacial area and volume change of each group are derived based on the work of Worosz [14], they are given as,

$$(\Delta A_i)_{WE,1}^{(12,2)} = -\frac{1}{\psi_1} \left(\frac{\alpha_1}{a_{i1}} \right)^2 \tag{4.87}$$

$$(\Delta A_i)_{WE,2}^{(12,2)} = \frac{2}{3\psi_2} \left(\frac{D_{sm1}}{D_{sm2}} \right)^3 \left(\frac{\alpha_2}{a_{i2}} \right)^2 \tag{4.88}$$

109

$$(\Delta V)_{WE,1}^{(12,2)} = -\frac{1}{\psi_1}\left(\frac{\alpha_1}{a_{i1}}\right)^3 \tag{4.89}$$

4.4.4 Group-2 Bubble Coalescence due to Wake Entrainment

In the case that Group-2 bubbles coalesce and get larger Group-2 bubbles due to wake entrainment, the leading and trailing bubble number density in this situation is approximated as,

$$n_l n_t = \frac{n_2^2}{4} \tag{4.90}$$

The bubble coalescence efficiency should be considered since the size of trailing bubble is now comparable to the pipe size. This indicates that when pipe size is small, the trailing Group-2 bubble within the wake region is less likely to escape due to the confined space. This situation can be opposite to that in a large diameter pipe. Therefore, the Group-2 bubble Sauter mean diameter is replaced by the pipe hydraulic diameter,

$$\lambda_{WE,2} = \exp\left(-C_{WE,2}\frac{D_h^{5/6}\rho_f^{1/2}\varepsilon^{1/3}}{\sigma^{1/2}}\right) \tag{4.91}$$

From the study of Fu [8], the relative velocity between the two Group-2 bubbles are formulated using an empirical correlation developed by Moissis and Griffith [65] as a function of the distance between the leading and trailing Group-2 bubbles,

$$\frac{u_2}{U_{2\infty}} = 1 + 8\exp\left(\frac{-1.06z}{D}\right) \tag{4.92}$$

This correlation was developed for slug flow without considering the viscous effect and surface tension effect. Therefore, for adiabatic air-water flow in a circular pipe, this correlation is valid when the pipe diameter is larger than around 27 mm, calculated based on the following criteria used in the study of Fu et al. [8],

$$N_\mu = \mu_f/(\rho_f\sigma\sqrt{\sigma/g\Delta\rho})^{1/2} < 0.032$$
$$D^* = D_h/\sqrt{\sigma/g\Delta\rho} > 10 \tag{4.93}$$

It indicates that Eq. 4.92 is not valid for flows in a small diameter pipe whose inner diameter is smaller than 27 mm, as viscous and surface tension effect can not be neglected. Moissis and Griffith [65] showed that the rising velocity of the trailing slug bubbles is much smaller in 0.5 inch pipe than those in larger pipes. In view of this issue, Eq. 4.92 is modified by introducing the scale of turbulent eddy velocity, which is proportional to the 3/4 times of Reynolds number,

$$\frac{u_2}{U_{2\infty}} = 1 + 8\exp\left(-1.06\frac{z}{D}\left(\frac{Re_{cr}}{Re_{D_h}}\right)^{3/4}\right) \tag{4.94}$$

Integral Eq. 4.94 over the wake length, which is from 0 to 7 times the pipe size, the average relative velocity can be expressed as,

$$\overline{\left[\frac{u_2}{U_{2\infty}}\right]} = \int_0^{7D_h} 1 + 8\exp\left(-1.06\frac{z}{D_h}\right)dz \approx 2\exp\left(-\left(\frac{Re_{cr}}{Re_{D_h}}\right)^{3/4}\right) \tag{4.95}$$

Based on the above equation, It can be concluded that the relative velocity between the trailing and leading Group-2 bubble is approximately 2 times the relative velocity of the Group-2 bubble in the infinite medium. The coalescence rate of Group-2 bubbles due to the wake entrainment mechanism is expressed as,

$$R_{WE}^{(2)} = C_{WE}^{(2)}\lambda_{WE,2}C_{D2}^{1/3}n_2^2 D_{b2}^2 u_{r2}\exp\left(-\left(\frac{Re_{cr}}{Re_{D_h}}\right)^{3/4}\right) \tag{4.96}$$

Now consider the interfacial area change during the coalescence of two Group-2 bubbles due to the wake entrainment. In a small diameter pipe, almost all the Group-2 bubbles can cover the whole flow cross-section. Thus, the size of the leading and trailing bubble is not important compared with the situation of Group-1 bubble wake entrainment. In a large diameter pipe, since the Group-2 bubbles have more freedom to move in the transverse direction, the wake region formed by the leading bubble can usually partially cover the trailing bubbles, as included in the consideration of Group-2 wake entrainment coalescence efficiency. In this sense, the leading bubble may not be necessarily larger than the trailing bubble. In summary, the average sizes of leading and trailing bubbles can be assumed as the

same. The characteristic change in Group-2 interfacial area for this interaction can be given as,

$$(A_i)^{(2)}_{WE,2} \approx -0.413 \frac{1}{\psi_2} \left(\frac{\alpha_2}{a_{i2}} \right)^2 \tag{4.97}$$

The final expression of the Group-2 wake entrainment source term of interfacial area concentration is,

$$\phi^{(2)}_{WE,2} = (\Delta A_i)^{(2)}_{WE,2} R^{(2)}_{WE} \tag{4.98}$$

4.5 Shearing-off of Small Bubbles at the Rim of Large Bubbles

When bubble size reaches a certain diameter or the relative velocity at the rim of the bubble is high enough, small bubbles can be sheared off from the rim of the large bubble by the shear force. In the previous study by Kim [4], the shearing-off source term is modeled by the force balance between the interfacial shear force and the surface tension force. In this approach, it is of vital importance to determine the bubble interfacial friction factor, in which the current existing correlations are not able to give a satisfying estimation. Another approach that analyzing the skirt volume and the sheared-off bubble size has been adopted by the studies of Sun [6] and Fu et al. [8]. This approach estimates the bubble shearing-off rate by dividing the skirt volume by the average sheared-off bubbles. The key parameter in using this approach is the relative velocity between the liquid and the large bubble at the end of the bubble. Fu et al. [8] modeled this parameter using the potential flow theory (Bernoulli equation) and considering the influence of the wall friction on the liquid velocity. This approach can be valid for large slug bubbles with their edges close to the pipe wall. Whereas the effect of the wall on the liquid velocity near the end of bubble can be minimized as the bubble is away from the pipe wall in a large diameter pipe. Although potential flow theory may still be valid in determining the liquid velocity around a Group-2 bubble that is not a slug bubble, the effect of wall friction on the liquid velocity should be remodeled. In this study, this derivation and modifications on bubble disintegration due to shearing-off are performed based on Fu's approach.

Firstly, the relative velocity at the rim of the large bubble v_{rb} is expressed as,

$$v_{rb} = -v_{lfj} + \overline{V}_{gj} \tag{4.99}$$

where v_{lfj} is the liquid film velocity. The $\overline{V}_{gj}$ is the drift velocity and can be estimated based on drift flux model,

$$\overline{V}_{gj} = (C_0 - 1)\, j + u_{r2} \tag{4.100}$$

where u_{r2} is given in Eq. 4.85. In order to estimate the liquid film velocity, it is further assumed that the pressure inside bubble is uniform and the liquid around the bubble can be regarded as in form of liquid film. Thus, the liquid film velocity at the rim of Group-2 bubble can be estimated by Bernoulli equation,

$$v_{lfj0} = -\sqrt{\frac{2gh_{slug}\Delta\rho}{\rho_f}} \tag{4.101}$$

where h_{slug} is calculated using Eq. 4.29 or simply approximated as $D_{sm,2}^3/D_{b2}^2$. The minus sign indicates the liquid velocity is opposite to the bubble velocity. In the study of Fu et al. [8], the effect of wall friction on the liquid film velocity is modeled in the form of an exponential function, analogous to the approaches used in the previous studies and current study in modeling phenomenal effects,

$$1 - \exp\left(-C_{SO,212}\frac{v_{\text{fm}}}{v_{lfj0}}\right) \tag{4.102}$$

where C is an adjustable parameter determined based on experimental data. v_{fm} is the liquid film velocity at the rim of the maximum stable Group-2 bubble, namely the slug bubble with a maximum possible length in the pipe. This is modeled by Mishima and Ishii [42] in the modeling of slug-to-churn turbulent flow regime transition criterion. Based on the potential flow theory mentioned above, v_{fm} can be estimated as,

$$v_{\text{fm}} = \sqrt{\frac{2gL_b\Delta\rho}{\rho_f}} \tag{4.103}$$

where L_b is the maximum possible length of the Group-2 bubble. This parameter can be calculated by Mishima and Ishii [42] as,

$$v_{\text{fm}} = j + 0.75 \sqrt{\left(\frac{\Delta\rho g D_h}{\rho_{\text{f}}}\right) \left(\frac{\Delta\rho g D_h^3}{\rho_{\text{f}} v_{\text{f}}^2}\right)^{1/18}} \qquad (4.104)$$

For air-water flow, the above equation can be further simplified as,

$$v_{\text{fm}} = j + 2.3 \sqrt{\left(\frac{\Delta\rho g D_h}{\rho_{\text{f}}}\right)} \qquad (4.105)$$

Eq. 4.102 has been proved by Fu et al.[8] as a good approximation for the wall friction on liquid film velocity in small and medium diameter pipes. However, two facts should be considered before Eq. 4.102 can be used for Group-2 bubbles in larger diameter pipes. Firstly, it is obvious that the Group-2 bubbles are not in form of gas slugs, instead, they are cap bubbles. Therefore, the assumption of potential flow may not be valid. Secondly, even if it can be could assume that the potential theory can be used for the estimation of liquid film velocity around the cap bubbles, the wall frictions effect is also reduced because Group-2 bubbles may not be close to the wall in a large diameter pipe. Therefore, the distance of Group-2 bubbles to the pipe wall should also be considered in estimating the wall fraction effect on the liquid film velocity. Therefore, Eq. 4.102 is modified by considering the Group-2 shape factors and the pipe diameter,

$$1 - \exp\left(-C_{SO,212}\sqrt{\frac{L_b D_h D_{b2}}{D_{sm2}^3}}\right) \qquad (4.106)$$

where L_b can still be calculated based on Eq. 4.104. Therefore, the relative velocity between the liquid and the Group-2 bubble at the rim of the bubble is expressed as,

$$v_{rb} = (C_0 - 1)j + u_{r2} + \left[1 - \exp\left(-C_{SO,212}\sqrt{\frac{L_b D_h D_{b2}}{D_{sm2}^3}}\right)\right]\sqrt{\frac{2gh_{slug}\Delta\rho}{\rho_f}} \qquad (4.107)$$

114

The shearing-off rate is modeled based on the shirt thickness approach used in Fu's study. From the study of Evans [66], the maximum sheared-off bubble size is given as,

$$d_{s,\max} = \left(\frac{We_c\sigma}{2}\right)^{3/5} (\rho_f)^{-1/5}(\varepsilon)^{-2/5} \tag{4.108}$$

where ε is the energy dissipation rate per unit volume,

$$\varepsilon \approx \frac{\rho_f b v_{rb}^3}{2L_{mz}}(1 - 2b) \tag{4.109}$$

Combine Eq.4.108 and 4.109, we get,

$$d_{s,\max} \propto \left(\frac{\sigma}{\rho_f}\right)^{3/5} D_h^{2/5} v_{rb}^{-6/5} \tag{4.110}$$

The averaged sheared-off bubble diameter can be estimated from the maximum sheared-off bubble diameter by multiplying Eq.4.110 with an arbitrary coefficient C_d,

$$d_s = C_d \left(\frac{\sigma}{\rho_f}\right)^{3/5} D_h^{2/5} v_{rb}^{-6/5} \tag{4.111}$$

C_d should be determined based on experimental data. Sun [6] gives $C_d = 4.8$ based on his experimental data. Noted that the test section of Sun's experiment uses a rectangle-shaped flow channel, therefore this coefficient should be re-determined for the circular pipe flow. Since there is no enough data to investigate the shearing-off effect, this coefficient will be investigated in the future work.

As stated before, the shearing-off rate is estimated by dividing the large bubble skirt volume by the averaged sheared-off bubble volume. The skirt volume is estimated by,

$$G_{\mathrm{SO}} \propto \pi D_{\mathrm{c}} \delta v_{\mathrm{r}} \tag{4.112}$$

where δ denotes the thickness of the skirt. For simlification, δ is approximated as equal as d_s,

$$\delta \approx d_s \tag{4.113}$$

Last but not least, the Group-2 bubble should have a sufficiently large size or the relative velocity should be large enough. A modification factor with its form based on the study of Worosz [14] is given as,

$$
g\left(We_2\right) = \begin{cases} \sqrt{1 - \frac{We_{cr2}}{We_2}}, & \text{for } We_2 > We_{cr2} \\ 0 & , \text{ else} \end{cases} \tag{4.114}
$$

where We_2 is expressed as,

$$
We_2 = \frac{\rho_f v_{rb}^2 D_{b2}}{\sigma} \tag{4.115}
$$

Overall, the shearing-off rate is expressed as,

$$
R_{SO}^{(2,12)} = \frac{G_{SO}}{V_{d_s}} = g\left(We_2\right) n_2 \frac{\pi D_c d_s v_r}{\frac{1}{3}\pi d_s^3} = 3g\left(We_2\right) C_{SO}^{(2,12)} n_2 C_d^{-2} \left(\frac{\sigma}{\rho_f}\right)^{-6/5} \lambda_p D_h^{1/5} v_{rb}^{-7/5} \tag{4.116}
$$

The Group-1 interfacial area and volume change can be easily estimated using the averaged sheared-off bubble diameter d_s,

$$
(\Delta A_i)_{SO,1}^{(2,12)} = \pi d_s^2 \tag{4.117}
$$

$$
(\Delta V)_{SO,1}^{(2,12)} = \frac{1}{6}\pi d_s^3 \tag{4.118}
$$

For the interfacial area change of the Group-2 bubble, the change happens at the rim of the bubble, namely the skirt. It can be estimated by assuming that the sheared-off volume is so small compared with the skirt volume that it only shortens the length/height of the skirt, but not the thickness of the skirt. In this sense, the interfacial area change of the Group-2 bubble can be estimated by the loss volume divided by the cross-section area of the skirt,

$$
(\Delta A_i)_{SO,2}^{(2,12)} \approx -\frac{\frac{1}{6}\pi d_s^3}{\pi D_h d_s} 2\pi D_h = -\frac{1}{3}\pi d_s^2 \tag{4.119}
$$

In summary, the interfacial area and volume source terms due to large bubble shearing-off is given as:

$$\phi_{SO,1}^{(2,12)} = 3g\left(We_2\right)C_{SO}^{(2,12)}\pi D_h n_2 v_{rb} \tag{4.120}$$

$$\phi_{SO,2}^{(2,12)} = -g\left(We_2\right)C_{SO}^{(2,12)}\pi D_h n_2 v_{rb} \tag{4.121}$$

$$\eta_{SO,2}^{(2,12)} = -0.5g\left(We_2\right)C_{SO}^{(212)}\pi n_2 C_d \left(\frac{\sigma}{\rho_f}\right)^{3/5}\lambda_p D_h^{2/5} v_{rb}^{-1/5} \tag{4.122}$$

4.6 Bubble Disintegration of Due to Turbulent Impact

The bubble interaction due to the turbulent impact is originally modeled by Wu et al. [3] in a simple momentum balance approach. Bubble in the continuous liquid phase collides with turbulent eddy with its size comparable to the size of colliding bubble. As stated in the previous studies such as [16], the larger eddies can only transport the bubble or deform the bubble in shape, instead of resulting in bubble disintegration. In this sense, the bubble disintegration mechanism is largely related to the availability of the turbulent eddies. This theory has been discussed in the modeling of bubble coalescence of random collision. For simplicity, the pipe diameter effect on the availability of turbulent eddies used in the modeling of random collision, expressed in Eq. 4.12, is also used for the modeling of turbulent impact. In this study, the modeling of Group-1 bubble disintegration due to turbulent impact uses the same formation in the study of Wu et al. [3],

$$\phi_{TI}^{(1)} = \frac{1}{18}C_{TI}^{(1)}g\left(We_1\right)\left(\frac{a_{i1}^2}{\alpha_1}u_{t1}\right)\exp\left(-\frac{We_{cr1}}{We_1}\right)f\left(D_{sm1}^*\right) \tag{4.123}$$

In terms of the Group-2 disintegration due to turbulent impact, the source term is derived following the same approach of Wu et al. [3]. Firstly, the momentum balance is given as,

$$\frac{\rho_f D^3 D}{\Delta T^2} \propto F_t - F_\sigma \tag{4.124}$$

where F_t and F_σ are inertia force and surface tension force, respectively. For a large Group-2 bubble, the two forces are expressed as,

$$F_t \propto \rho_f u_t^2 D_h^2 \tag{4.125}$$

$$F_\sigma \propto \sigma D_h \tag{4.126}$$

Thus, the general disintegration rate can be derived as,

$$R_{\mathrm{TI}} \propto n \frac{1}{\Delta T} = n \frac{u_t}{D_h} \left(1 - \frac{We_{\mathrm{cr}}}{We} \right)^{1/2}, \quad We > We_{\mathrm{cr}} \tag{4.127}$$

Considering the collision efficiency that the large bubble successfully breaks up when the bubble and turbulence interact with each other, the final form of the Group-2 bubble disintegration rate due to turbulent impact is given as,

$$R_{TI}^{(2)} = C_{TI}^{(2)} g\left(We_2\right) n_2 \frac{(\varepsilon)^{1/3}}{D_h^{2/3}} \exp \left(-\frac{We_{cr2}}{We_2} \right) f\left(D_{sm2}^*\right) \tag{4.128}$$

where u_{t2} denotes the Group-2 bubble turbulent velocity,

$$u_{t2} = \sqrt{2} \left(\varepsilon D_h\right)^{1/3} \tag{4.129}$$

The interfacial area change of the disintegration interaction is modeled by assuming the original bubble can break up into any Group-2 bubble size smaller than the original bubble with equal probability. In this sense, the process can be regarded as the opposite of two equal-sized bubbles coalesce with each other. Therefore, the interfacial area change is given as,

$$(\Delta A_i)_{TI,2}^{(2)} = \frac{0.26}{\psi_2} \left(\frac{\alpha_2}{a_{i,2}} \right)^2 \tag{4.130}$$

4.7 Bubble Disintegration of Due to Surface Instability

The bubble disintegration due to surface instability usually happens only in large diameter pipes. It is known to happen when the bubble radius of curvature is greater than the maximum stable bubble size $D_{c,max}$ in Eq. 4.22, thus, flow channel cross-sectional area should be large enough to accommodate this size of bubble. It is also assumed that the bubble disintegration due to surface instability happens instantaneously when a bubble reaches to the disintegration size. In the previous studies of IATE development, the surface instability mechanism is only focused for large flow channel systems, such as Sun [6] and Smith [7]. In these studies, the modeling of surface instability is considered as a symmetrically mechanism of large bubble coalescence that can create a bubble whose size is larger than the maximum stable bubble size. The pressure change and advection effects that could increase the bubble size towards the maximum stable bubble size are negligibly small. These bubble coalescence mechanism includes Group-2 bubble random collision and wake entrainment. Following their approaches, the the interaction rate of surface instability can be firstly estimated based on Eq. 4.50 and Eq. 4.94 as,

$$
\begin{aligned}
R_{SI}^{(2)} =& R_{RC}^{(2)} + R_{WE}^{(2)} \\
=& C_{RC}^{(2)} u_{t2} n_2 \alpha_2^{1/6} \alpha_{max,2}^{-2/3} a_{i,2} (1-\alpha_1)^{1/2} \lambda_{RC,2} f\left(D_{sm2}^*\right) \\
&+ C_{WE}^{(2)} C_{D2}^{1/3} n_2^2 D_{b2}^2 u_{r2}
\end{aligned}
\tag{4.131}
$$

In terms of the estimation of the interfacial area change, Smith [7] gave a model based on the study of initial disturbance angular location by Miller et al. [67],

$$
\begin{aligned}
\Delta A_i &= \left[\left(\tfrac{D_1}{D_{c,\max}}\right)^2 + \left(\tfrac{D_2}{D_{c,\max}}\right)^2 - 1\right] \cdot A_{i,\max} \\
D_1 &= 0.452 D_{c,\max}, \quad D_2 = 0.767 D_{c,\max} \\
\Delta A_i &= 0.488 D_{c,\max}^2
\end{aligned}
\tag{4.132}
$$

Therefore, the final expression for the Group-2 bubble disintegration due to surface instability can be given as,

$$\Phi_{SI}^{(2)} = p_{c2}\Delta A_i \left[\begin{array}{c} C_{WE}^{(2)}C_{D2}^{1/3}n_2^2 D_{b2}^2 u_{r2} \\ +C_{RC}^{(2)}u_{t2}n_2\alpha_2^{1/6}\alpha_{max,2}^{-2/3}a_{i,2}(1-\alpha_1)^{1/2}\lambda_{RC,2}f\left(D_{sm2}^*\right) \end{array} \right] \tag{4.133}$$

where p_{c2} estimates the percentage of the Group-2 bubble that could coalescence with another Group-2 bubble and becomes larger than the maximum stable bubble, similar to Eq. 4.42.

4.8 Summary

In this Chapter, the bubble interaction source/sink term models for the two-group interfacial area transport equation (IATE) for vertical round pipes with large geometrical scalability were developed. The developed mechanistic models for bubble interactions are based on the existing models that are designed for medium and large diameter pipes.[3], [4], [6], [14], [62]. The original contribution of this work on the newly derived interaction source terms is it identified and modeled the pipe wall effect on the bubble interactions. the major contributions of this modeling work are summarized in the following paragraphs.

For modeling of the bubble interactions driven by the flow turbulence, a fundamental assumption is used that the turbulence, in the forms of vortexes or eddies, that drives the bubbles to fluctuate and collide is usually in inertia subrange scale. This assumption is usually valid for medium and large diameter pipe flow, however, not for small diameter pipe flows. This is because the integral length scale is small in a small diameter pipe and close to the bubble size scale for air-water flow in ambient condition. In this sense, the bubble or turbulent eddy size can be in the energy-containing subrange scale. For the models developed under inertia subrange assumption to be applicable for small diameter pipe flows, a modification for the turbulence in terms of size-corresponding turbulent eddy density is necessary. Therefore, the modification function developed by Pope [58] is re-formulated and used for this study.

For the bubble interactions of the two-phase flow in small diameter pipes, the wake entrainment is the dominant coalescence mechanism. Besides, in the transition regime from

one-group to two-groups, namely bubbly-to-slug transition regime in small diameter pipes, wake entrainment is significantly dominant and it leads to a drastic intergroup transfer phenomenon. A transition function in terms of the critical bubble diameters, derived in the previous chapter, is developed for the wake entrainment model, thus giving the IATE the ability to predict this unique phenomenon happening in small diameter pipes. When large Group-2 bubble exists in the flow, the shearing-off and turbulent impact on the large bubble gradually emerge and become significant.

In large diameter pipes, the random collision is the dominant coalescence mechanism. The transition between bubbly to cap bubbly flow is also largely due to the random collision. [59] This is due to that the large flow channel cross-sectional area leads to the relative free bubble movement and interaction driven by the random collision. The bubble-induced turbulence in the flow is also higher as the turbulence generated from bubble can hardly be reduced by the pipe wall. In the modeling of random collision, transition functions related to the relative bubble diameter to the pipe diameter are added to consider the pipe diameter effect on the random collision.

In summary, 15 models in total are included in the newly proposed two-group bubble interaction terms for IAC, given as:

$$
\begin{aligned}
\sum \phi_{j,1} = {} & \phi_{RC,1}^{(11,1)} + \phi_{RC,1}^{(12,2)} + \phi_{WE,1}^{(11,2)} \\
& + \phi_{WE,1}^{(12,2)} + \phi_{TI,1}^{(1,11)} + \phi_{SO,1}^{(2,12)}
\end{aligned}
\tag{4.134}
$$

$$
\begin{aligned}
\sum \phi_{j,2} = {} & \phi_{RC,2}^{(11,2)} + \phi_{RC,2}^{(12,2)} + \phi_{RC,2}^{(22,2)} \\
& + \phi_{WE,2}^{(11,2)} + \phi_{WE,2}^{(12,2)} + \phi_{WE,2}^{(22,2)} \\
& + \phi_{TI,2}^{(2,22)} + \phi_{SO,2}^{(2,12)} + \phi_{SI,2}^{(2,22)}
\end{aligned}
\tag{4.135}
$$

5 models are included in the two-group bubble interaction terms for void fraction, given as:

$$
\begin{aligned}
\sum \phi_{j,2} = {} & \eta_{RC,2}^{(11,2)} + \eta_{RC,2}^{(12,2)} + \eta_{WE,2}^{(11,2)} \\
& + \eta_{WE,1}^{(12,2)} + \eta_{SO,1}^{(21,2)}
\end{aligned}
\tag{4.136}
$$

$$
\sum \eta_{j,1} = -\sum \eta_{j,2}
\tag{4.137}
$$

5. EVALUATION OF NEWLY-DEVELOPED INTERFACIAL AREA TRANSPORT EQUATION FOR VERTICAL CIRCULAR PIPES

In this chapter, the evaluation scheme of the newly-developed mechanistic models for bubble interactions will be provided and the evaluation results will be discussed. Given the complexity of the IATE, the veracity of the newly developed constitutive models is initially evaluated in one-dimensional form [3]. The IATE and its constitutive equations are simplified by averaging into one-dimensional forms. The coefficients that should be determined through experimental data will be specified. The evaluation of the newly developed IATE constitutive models follows the same procedures taken by the previous studies [6], [14].

5.1 Steady-state One-dimensional Two-group Interfacial Area Transport Equation

The general form of the two-group interfacial area transport equation was presented in the earlier chapter,

$$
\begin{aligned}
\frac{\partial a_{i1}}{\partial t} + \nabla \cdot (a_{i1}\vec{v}_{i1}) = &\left[\frac{2}{3} - \chi^2\right]\left(\frac{a_{i1}}{\alpha_1}\right)\left[\frac{\partial \alpha_1}{\partial t} + \nabla \cdot (\alpha_1 \vec{v}_{g_1}) - \eta_{ph1}\right] \\
&+ \sum_j \phi_{j1} + \phi_{ph1}
\end{aligned}
\tag{5.1}
$$

$$
\begin{aligned}
\frac{\partial a_{i2}}{\partial t} + \nabla \cdot (a_{i2}\vec{v}_{i2}) = &\frac{2}{3}\left(\frac{a_{i2}}{\alpha_2}\right)\left[\frac{\partial \alpha_2}{\partial t} + \nabla \cdot (\alpha_2 \hat{v}_{g_2}) - \eta_{ph2}\right] \\
&+ \chi^2\left(\frac{a_{i1}}{\alpha_1}\right)\left[\frac{\partial \alpha_1}{\partial t} + \nabla \cdot (\alpha_1 \vec{v}_{g_1}) - \eta_{ph1}\right] + \sum_j \phi_{j2} + \phi_{ph2}
\end{aligned}
\tag{5.2}
$$

The one-dimensional forms of the above equations are obtained by taking proper averaging over the interfacial terms that varies in r and θ directions (in a cylindrical coordinate system). Specifically, the void fractions α and interfacial area concentrations (IAC) a_i are taking area averaging,

$$
\langle\xi\rangle \equiv \frac{1}{A}\int_A \xi(x,y)\mathrm{d}A
\tag{5.3}
$$

122

and the velocities are taking parameter(e.g. void fraction)-weighted averaging,

$$\langle\langle\xi\rangle\rangle = \frac{\int \alpha(x,y)\xi(x,y)\mathrm{d}A}{\int_A \alpha(x,y)\mathrm{d}A} = \frac{\frac{1}{A}\int \alpha(x,y)\xi(x,y)\mathrm{d}A}{\langle\alpha\rangle} \tag{5.4}$$

Noted that the approximation of IAC-weighted velocity $\langle\langle\vec{v}_{i1}\rangle\rangle$ follows the same treatment of Sun [6] since the bubble size if group-1 bubbles across the flow channel is nearly uniform in the test cases,

$$\langle\langle\vec{v}_{i1}\rangle\rangle = \frac{\langle a_{i1}\bar{v}_{i1}\rangle}{\langle a_{i1}\rangle} \approx \frac{\langle \alpha_1 \bar{v}_{g1}\rangle}{\langle \alpha_1\rangle} = \langle\langle\vec{v}_{g1}\rangle\rangle = \langle\langle v_{gz1}\rangle\rangle \tag{5.5}$$

where $\langle\langle v_{gz1}\rangle\rangle$ can be obtained from the experiment. These types of averaging methods is valid under the adiabatic, air-water experimental conditions since the bubble size across the flow channel is nearly uniform, thus the covariances between interfacial area concentration, void fraction, and gas velocity raised through the area-averaging should be negligibly small. Another approximation that adopted here is from Worosz [14] that the effects of intergroup expansion/contraction χ can be negligible. This approximation is also valid in this study since the intergroup transfers due to the pressure and velocity change under the adiabatic, air-water experimental conditions can hardly occur. Based on the above averages and simplifications, the IATE is converted into a steady-state one-dimensional two-group form and can be expressed as,

$$\frac{\mathrm{d}}{\mathrm{d}z}\left(\langle a_{i1}\rangle\langle\langle v_{gz1}\rangle\rangle\right) = \frac{2}{3}\frac{\langle a_{i1}\rangle}{\langle\alpha_1\rangle}\frac{\mathrm{d}}{\mathrm{d}z}\left(\langle \alpha_1\rangle\langle\langle v_{gz1}\rangle\rangle\right) + \sum_j \langle\phi_{j,1}\rangle \tag{5.6}$$

and

$$\frac{\mathrm{d}}{\mathrm{d}z}\left(\langle a_{i2}\rangle\langle\langle v_{gz2}\rangle\rangle\right) = \frac{2}{3}\frac{\langle a_{i2}\rangle}{\langle\alpha_2\rangle}\frac{\mathrm{d}}{\mathrm{d}z}\left(\langle \alpha_2\rangle\langle\langle v_{gz2}\rangle\rangle\right) + \sum_j \langle\phi_{j,1}\rangle \tag{5.7}$$

$\langle\phi_{j,1}\rangle$ and $\langle\phi_{j,2}\rangle$ are the interaction source and sink terms. In the present study, for simplicity, the covariance terms that are generated by taking area averaging on these interaction terms are neglected. The source/sink terms are based on the work from Sun [6] and Worosz [14] and modified wake entrainment model presented in the earlier chapter.

5.2 Model Evaluation Method and Supporting Models

The general form of the IATE and mechanistic models were properly averaged. Meanwhile, some key parameters including the energy dissipation rate and relative velocities should be also properly treated in the one-dimensional calculations. In the previous IATE studies, these parameters are usually calculated using different equations since these studies usually focus on the two-phase flows in either small or large flow channels. However, they may not be valid in each other's situation. For a model that aims at both small and large diameter pipes, these parameters should be revised to be adopted in more generalized models. This section provides detailed discussions on the supporting models of energy dissipation, relative velocities, and the drift-flux correlation for the 1-D IATE calculations. Other supporting models are presented in Table 5.1.

Supporting Models

The energy dissipation rate is a crucial parameter for bubble interactions. In the sophisticated CFD modelings that the interfacial area transport equation is coupled with filed equations and constitutive equations, ε can be calculated locally such as k-ε model and the Reynolds averaging method. [3] For the one-dimensional evaluation, ε is simplified into approximated correlations by assuming the turbulent production is equal to the turbulent dissipation. Therefore, the turbulent dissipation can be expressed using the expressions on turbulent generations. In the study of Sato and Sakoguchi [68], the turbulence in a confined channel is considered to be the addition of the shear-induced turbulence and the bubble-induced turbulence. By simplifying the modeling that the turbulent dissipation is to be equal as the turbulent production [7], the turbulent dissipation rate can be expressed as,

$$\varepsilon = \varepsilon_{SI} + \varepsilon_{BI} \tag{5.8}$$

The shear-induced turbulent dissipation rate is given by the study of Wu et al. [3],

$$\varepsilon_{SI} = f_{TW} \frac{v_w^3}{2D_h} v_r^3 D_b \tag{5.9}$$

where f_{TW} is the two-phase friction factor and is is calculated as,

$$f_{\mathrm{TW}} = f_{\mathrm{f}} \left(\frac{\mu_{\mathrm{m}}}{\mu_{\mathrm{f}}}\right)^{0.25} = \frac{0.316}{Re_{\mathrm{m}}^{0.25}} \left(\frac{1}{(1 - \langle\alpha\rangle)}\right)^{0.25} \tag{5.10}$$

The bubble-induced turbulent dissipation rate is given by the study of Schlegel et al. [69],

$$\varepsilon_{BI} = \frac{1}{8}C_D a_i^2 v_r^3 D_b \tag{5.11}$$

From Eq. 5.9 to 5.11, the pipe diameter can have an effect on the turbulence across the flow channel. With the increase of the flow channel diameter, the velocity gradient becomes small and the wall-induced turbulence becomes less intensive. At the same time, the wall effect that reduces the bubble-induced turbulence becomes weak, and the bubble interaction becomes to be more intensive in the large diameter flow channel than in the small diameter flow channel. Hibiki and Ishii [20] proposed an approximate energy dissipation rate in consideration of the pipe diameter,

$$\varepsilon \approx \varepsilon_{BI} \exp\left(-A \operatorname{Re}_f\right) + \varepsilon_{SI} \left\{1 - \exp\left(-A \operatorname{Re}_f\right)\right\} \tag{5.12}$$

where A and Re_f are an adjustable coefficient and flow channel Reynolds number, respectively. A is given as 0.0005839.

Specifically, the one-dimensional Group-1 relative velocity in the evaluation to the equation used by Worosz [14] and it is expressed as follows:

$$u_{r1} = \sqrt{\frac{g D_{sm} \Delta\rho}{3 C_D \rho_f}} \tag{5.13}$$

The effect of pipe diameter on the Group-2 bubble relative velocity is more explicit. Based on the study of Sun's study [6], the Group-2 relative velocity is related to the bubble cross-sectional diameter D_{b2}, which is modeled based on the simple model of Group-2 bubble shape

and the pipe diameter. Therefore, the Group-2 bubble relative velocity is expressed using the below piecewise function,

$$u_{r2} = \begin{cases} 0.69\sqrt{\frac{gD_{sm2}\Delta\rho}{\rho_f}} & (D_{sm2}^* \leq 0.337) \\ 0.35\sqrt{\frac{gD_h\Delta\rho}{\rho_f}} & (D_{sm2}^* > 0.337) \end{cases} \tag{5.14}$$

Model Evaluation Method

The finite difference method is used to convert the continuous governing equations to discrete form including two-group void fraction and IAC transport equations. This method follows the approach in the previous evaluation scheme designed by Worosz. One of the important step is to exclude the intergroup expansion/contraction and include the intragroup expansion/contraction source/sink term in the IAC calculation. The final form of the discrete intragroup expansion/contraction terms are given as,

$$\left\langle \phi_{exp,1}^{intra} \right\rangle_i = -\frac{2}{3} \frac{\left(\langle a_{i1} \rangle \left\langle \langle v_{g1} \rangle \right\rangle \right)_i}{(\rho_g)_{i+1}} \frac{(\rho_g)_{i+1} - (\rho_g)_i}{\Delta z} \tag{5.15}$$

$$\left\langle \phi_{exp,2}^{intra} \right\rangle_i = -\frac{2}{3} \frac{\left(\langle a_{i2} \rangle \left\langle \langle v_{g2} \rangle \right\rangle \right)_i}{(\rho_g)_{i+1}} \frac{(\rho_g)_{i+1} - (\rho_g)_i}{\Delta z} \tag{5.16}$$

where ρ_g per each step is converted from the initial condition and the local pressure,

$$\rho_{\mathrm{g}}(z) = \rho_{\mathrm{g}}(z_0) \left(1 + \frac{z - z_0}{p(z_0)} \frac{\mathrm{d}p}{\mathrm{d}z} \right) \tag{5.17}$$

The details of the calculation scheme are depicted in Figure 5.1.

5.3 Evaluation Database

The evaluation of the model performance uses a database generated from multiple experiments. Besides the adiabatic, air-water vertical two-phase flow experiments on 12.7mm ID pipe collected in this study, the experimental data taken in vertical pipes with various sizes are also included to form a completed database. Table 5.2 summaries the experimental

Table 5.1. Summary of the supporting models of two-group IATE.

Interaction term	Model
Maximum packing void fraction	$\alpha_{1,\max} = 0.75$
Bubble terminal velocity	$u_{r1} = \sqrt{\frac{gD_{sm}\Delta\rho}{3C_D\rho_f}}$ $u_{r2} = \begin{cases} 0.69\sqrt{\frac{gD_{sm2}\Delta\rho}{\rho_f}} & (D^*_{sm2} \leq 0.337) \\[2mm] 0.35\sqrt{\frac{gD_h\Delta\rho}{\rho_f}} & (D^*_{sm2} > 0.337) \end{cases}$
Drag coefficients	$C_{D1} = \frac{2}{3}D_{Sm1}\sqrt{\frac{g\Delta\rho}{\sigma}}\left(1 - \langle\alpha_1\rangle\right)^{-1/2}$ $C_{D2} = \frac{8}{3}\left(1 - \langle\alpha_2\rangle\right)^2$
Turbulent kinetic energy dissipation rate	$\varepsilon = f_{TW}\frac{1}{2D_h}\langle v_m\rangle^3$ $f_{TW} = f_f\left(\frac{\mu_m}{\mu_f}\right)^{0.25} = \frac{0.316}{Re_m^{0.25}}\left(\frac{\mu_m}{\mu_f}\right)^{0.25}$ $\mu_m = \frac{\mu_f}{1-\langle\alpha\rangle}, \langle v_m(z)\rangle = \frac{\rho_g(z)\langle j_g(z)\rangle + \rho_f\langle j_f\rangle}{\langle\alpha\rangle\rho(z)+(1-\langle\alpha\rangle)\rho_f}$
Mixture Reynolds number	$Re_m = \frac{\rho_f D_h v_m}{\mu_m}$
Bubble Reynolds number	$Re_b = \frac{\rho_g D_{sm}u_r}{\mu_g}$
Mixture viscosity	$\mu_m = \frac{\mu_f}{1-\langle\alpha\rangle}$
Maximum distorted bubble diameter	$D_{d,max} = 4\sqrt{\frac{\sigma}{g\Delta\rho}}$
Maximum stable bubble diameter	$D_{c,max} = 40\sqrt{\frac{\sigma}{g\Delta\rho}}$

Figure 5.1. Schematic flow diagram of the numerical solution scheme.

database used in the IATE evaluation. The selection of these experimental data is based on the similarities of these experimental setups. Firstly, they are all round pipe flow channels with spargers at the inlet and no flow constraints at the outlet. The spargers used in the experiments are made of porous rods. Secondly, there are several measurement positions for local interfacial area measurements that the first port can be used as the inlet/initial condition and the others can be used for the comparisons with the model predictions. Note here although the locations of these ports can be different for different test facilities, the comparisons are made between the predictions at the same developing level and the experimental measurements. In general, 112 test cases in total are used in the evaluation and most of them are located near the transition boundary from the bubbly flow and slug flow, where the pipe size can have a large effect on the interfacial area transport.

Table 5.2. Experimental databases for IATE evaluation.

Research	Pipe size	No. of data
Current study	12.7 mm	23
Wang et al. [32]	25.4 mm	24
Worosz [14]	50.8 mm	9
Smith [7]	101.6 mm	19
Smith [7]	152.4 mm	12
Schlegel [59]	203.2 mm	11
Schlegel [59]	304.8 mm	14
Total		112

5.4 Model Coefficient

In this study, as the models developed consider the general relations of the hydrodynamic parameters and ignore the ratios, the coefficients of the mechanistic models in the previous studies are no longer valid for the newly developed models in this study and should be re-determined. The adjustable coefficients typically are determined from certain experimental flow conditions where some interaction mechanisms are more dominant than the others. The determination of the dominant interaction mechanisms is based on experimental and analytical observations. Specifically, the major steps of determining the coefficients are adapted from the study by Sun [6], and summarized as follows:

- The coefficients in the current study associated with the models in the previous studies should be around the same orders of magnitude as those in the previous studies;

- The intergroup transport coefficients are evaluated and determined through the void fraction transport equation;

- The intragroup transport can be determined based on the interfacial area transport equation along with the pre-determined intergroup coefficients.

Specifically, the coefficients associated with shearing-off C_{so} and $We_{c,so}$ should be determined using the flow conditions with both the existence of large bubbles and high velocity ($> 1.2m/s$ for this study). In the study of Sun, C_{so} and $We_{c,so}$ are set as 4500 and 3.8×10^{-5}. Given the geometrical difference which leads to the bubble shape difference in the flow channel, these two parameters are modified based on the following consideration. When pipe size is small, a bubble of the same scale can have a larger deformation and larger radius of curvature along the flowing direction, thus the small bubbles can be sheared off at the rim more easily. As a result, either C_{so} should be higher or $We_{c,so}$ should be lower. Since the current database focuses on the transition between bubbly to slug and only 2 flow conditions satisfy the criteria, the coefficient C_{so} is set as in the order of 10^{-4} to fit these conditions. However, future study is essentially needed when more satisfying data is obtained.

To summarize, the values of the intergroup and intragroup coefficients determined based on the above discussion are summarized as follows:

- Random Collision: $C_{RC}^{(1)} = 0.003$, $C_{RC}^{(122)} = 0.005$, $C_{RC1} = 3.0$, $C_{RC2} = 3.0$, $C_{RC,(1)} = C_{RC,(122)} = C_{RC,(2)} = 1.29$

- Wake Entrainment: $C_{WE}^{(1)} = 0.05$, $C_{WE}^{(122)} = 0.025$,$C_{WE}^{(2)} = 0.25$.

- Turbulent Impact: $C_{TI}^{(1)} = 0.002$, $We_{cr,TI}^{(1)} = 6.5$, $C_{TI}^{(2)} = 1.0$, $We_{cr,TI}^{(2)} = 9.5$

- Shearing-Off: $C_{SO}^{(2,12)} = 8 \times 10^{-4}$, $C_d = 4.8$, $We_{c,SO} = 4500$. $C_{SO,212} = 1.25$.

5.5 Model Performances

Table 5.3 summaries the average IAC root mean square relative errors (RMS) at port2 and port3 in different sizes of pipes. The errors are calculated as,

$$RMS = \sqrt{\sum_{j=1,k=2}^{j=N,k=3} \left[\frac{\left\langle a_{i,kj} \right\rangle_{pred} - \left\langle a_{i,kj} \right\rangle_{exp}}{\left\langle a_{i,kj} \right\rangle_{exp}} \right]^2} \qquad (5.18)$$

where j indicates the number of test conditions in this pipe, and k indicates the port number. Overall, the average absolute relative errors for the total IAC and void fraction less than 15%. Figure 5.2 to 5.5 gives the comparing values of the experimental and predicting IACs and void fractions. In these figures, the performance of the model on each flow condition is presented. Experimental results for small and large diameter pipes are plotted separately. In general, the differences between the predictions and the experiments are sufficiently small. Specifically, the drastic intergroup transfer that happened in 12.7mm and 25.4mm test cases are predicted fairly well by the new-derived model. Therefore, it can be concluded that the overall performance of the new-derived model is reasonably good. The detailed two-group model predictions for each test condition are given in the Appendix.

Table 5.3. Absolute relative errors for void fraction and interfacial area concentrations.

Root-Mean-Square (RMS) relative error for IAC, %								
Pipe diameter [mm]	304.8	203.2	152.4	101.6	50.8	25.4	12.7	Overall
Port2	20.5	16.3	9.5	11.3	3.1	9.3	10.3	11.5
Port3	15.7	14.3	11.1	17.9	7.2	15.6	14.3	14.4
No. of test case	14	11	12	19	9	24	23	112
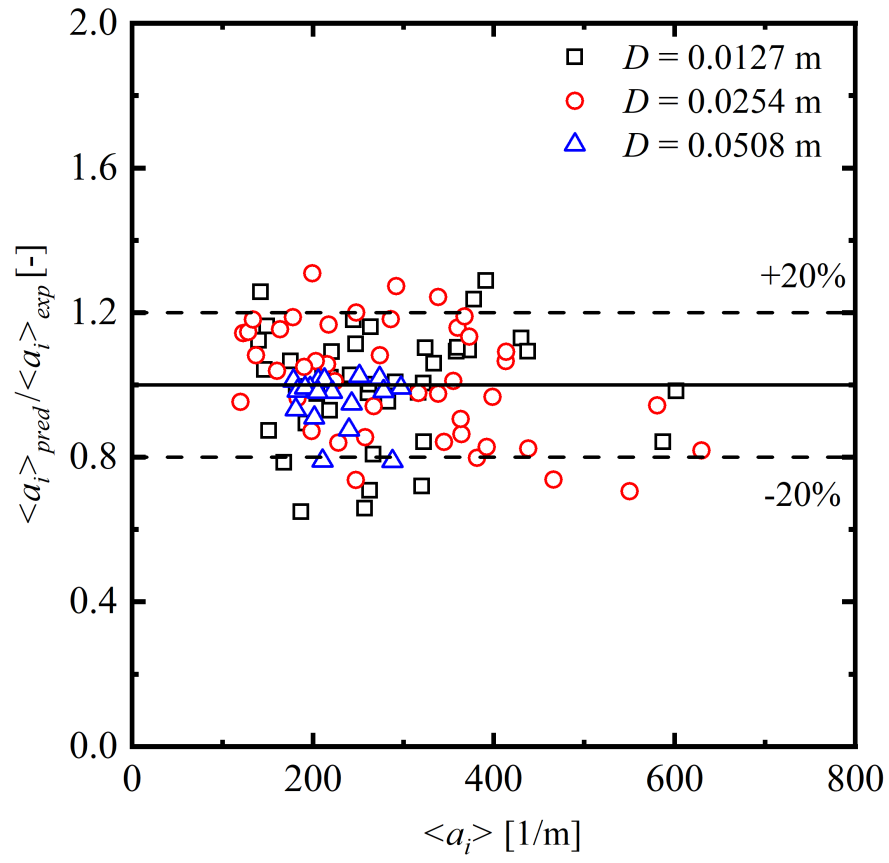
Figure 5.2. Model performance for IAC predictions in small diameter pipes.
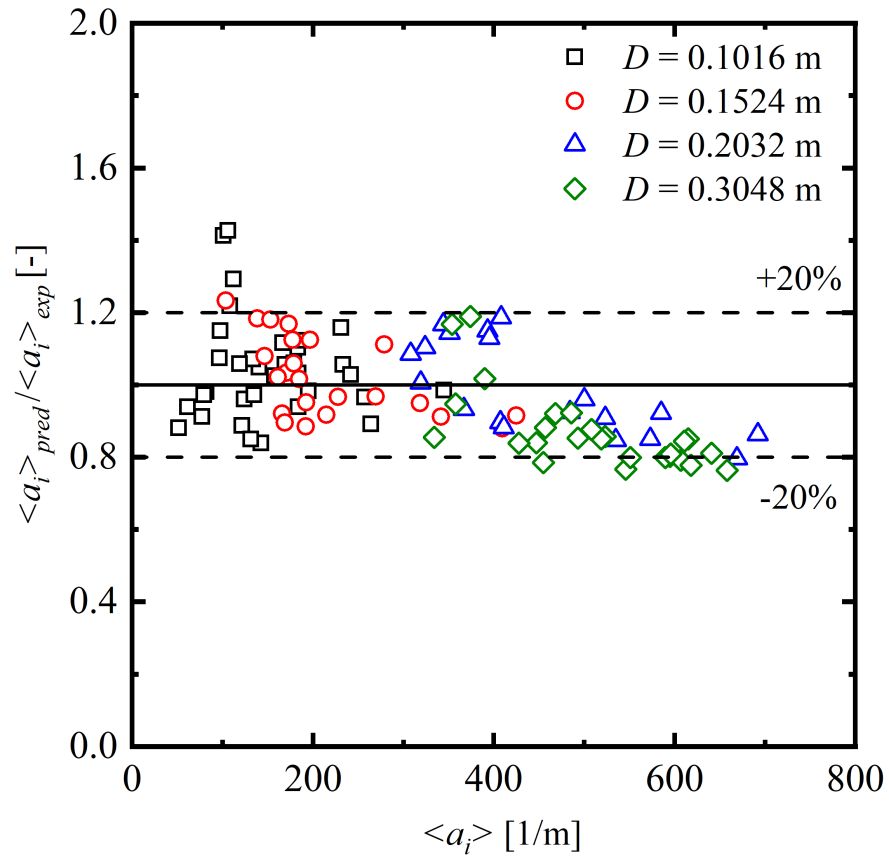
Figure 5.3. Model performance for IAC predictions in large diameter pipes.
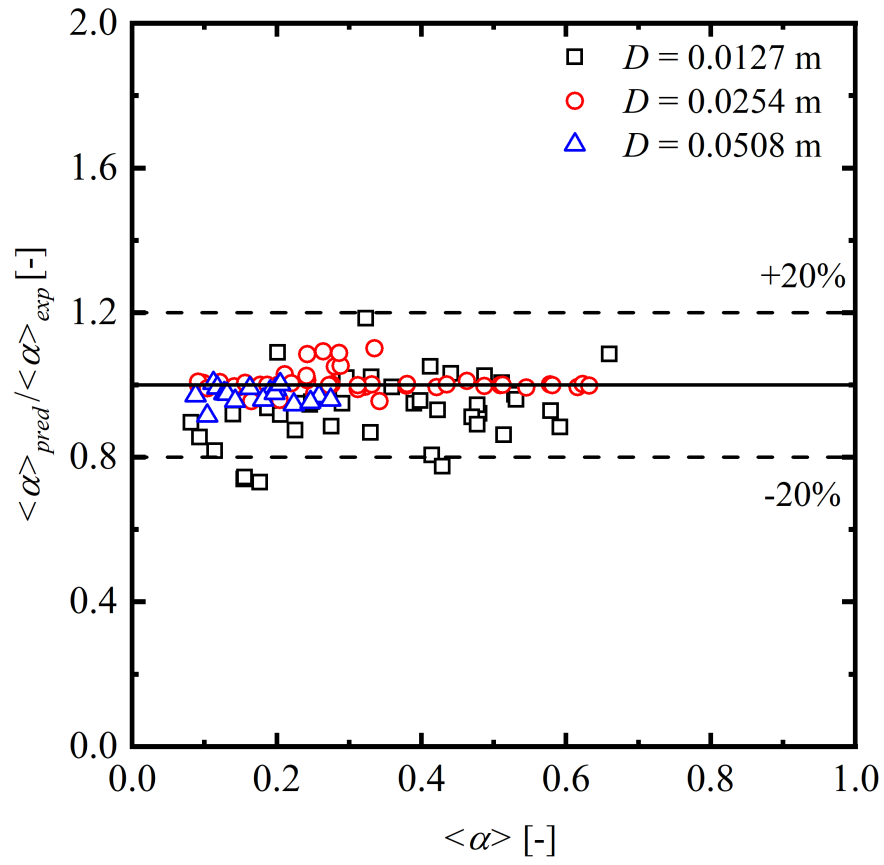
Figure 5.4. Model performance for void fraction predictions in small diameter pipes.
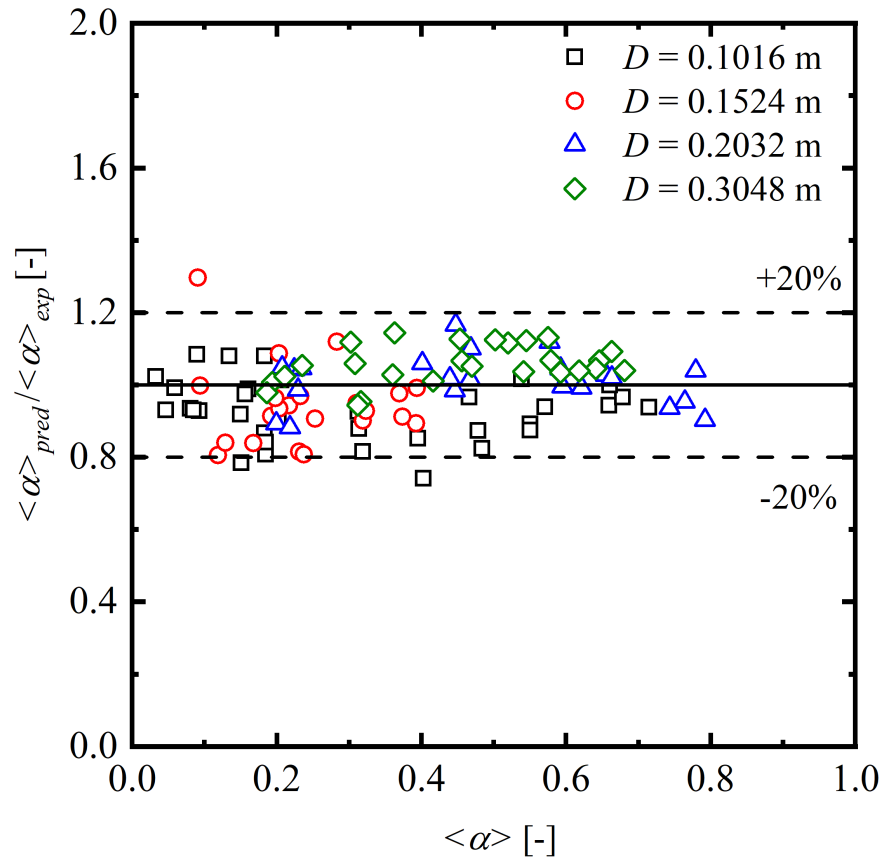
Figure 5.5. Model performance for void fraction predictions in large diameter pipes.

6. SUMMARY AND FUTURE WORK

6.1 Summary of Current Work

Although in the past twenty-five years, extensive studies were performed on the model development of interfacial area transport equation (IATE), it was identified that no universal IATE model is available with high geometrical scalability that can give good predictions on all the dispersed flow regimes and flow regime transitions. The existing models are generally focusing on medium and large flow channels that do not take into account the flow channel size effect on small spherical bubbles, thus, they are not suitable for small flow channels. A throughout understanding of the flow channel geometry on interfacial characteristics is essentially needed to fully realize the advantage of two-group IATE as a dynamic closure model for the two-fluid model. The primary objective of this study is to develop models for IATE to extend its predicting capabilities for small flow channels. With the newly-derived models, the IATE should be able to make good predictions for all dispersed and transition flows on all size circular flow channels. To realize this objective, this study sought to address this issue through experimental and theoretical analysis. The contributions of this work are summarized as follows:

6.1.1 Experimental Study of Pipe Diameter Effect on Two-phase Interfacial Characteristics

To investigate the two-phase flow in small diameter pipes and fill the data gap, An adiabatic air-water experiment was conducted on vertical-upward round pipes with an inner diameter of 12.7 mm. 23 flow conditions in total were conducted in the experiment, focusing on the bubbly, slug, and bubbly-to-slug transition flow regime. In each flow condition, the four-sensor conductivity probes were used for the measurements of local time-averaged two-phase flow parameters at a high acquisition frequency. These parameters, including void fraction and interfacial area concentration (IAC), were collected at three axial locations along the test section. For the modeling purpose, the dispersed gas phase, in form of bubbles, is classified into the small bubble (Group-1) and large bubble (Group-2) groups.

Along with experimental data in the existing literature, the wall effect on the interfacial characteristics are analyzed and the major findings and work are:

- Due to the relatively large bubble size in small-D pipes, The wall-peak void fraction distribution in a small-D pipe is not as significant as in a large-D pipe.

- The distribution parameter in the Drift-flux model is modified by considering both void fraction and the relative bubble size.

- Bubbly-to-slug flow regime transition will happen in a smaller void fraction in a small-D pipe, and it can be predicted by defining an effective flow channel area ratio.

- Bubble coalescence mechanism is more dominant in a small-D pipe compared with the bubble disintegration, and the intensity of intergroup transfer between small and large groups of bubble can be higher in a small-D pipe.

- Two geometrical parameters, void fraction and relative bubble diameter, are identified as the influential parameters to the intergroup transfer.

6.1.2 Development of a Generalized Interfacial Area Transport Equation for Circular Pipes

The mechanistic models for bubble interaction source/sink terms of the two-group IATE for circular pipes were developed. To apply the existing IATE models for medium and large diameter pipes to the modeling for small diameter pipes, the wall effect on the interfacial parameters and bubble dynamics are identified and properly modeled. The significance of the types of bubble interactions is further discussed based on the experimental analysis. In small diameter pipes, due to the weak turbulence, random collision and turbulent impact are not strong bubble interaction mechanisms. While the overall bubble coalescence becomes stronger, wake entrainment that is not directly related to the flow turbulence (instead it is related to the bubble-enhanced turbulence) is the dominant coalescence mechanism for the small pipes. While in the transition regime from one-group to two-groups, namely bubbly-to-slug transition regime, the wake entrainment becomes significantly dominant. When large Group-2 bubbles exist in the flow, the shearing-off and turbulent impact on large bubbles

137

gradually emerge and become significant. These mechanisms are properly modeled based on the previous studies of Wu et al. [3] and Kim [4]. The following contributions were made:

- For bubble interaction for small diameter pipe flow, the inertia subrange assumption may not be valid, and the bubble size can be in the energy-containing subrange scale. For the existing interaction models to be able to apply for small diameter pipe flows, the modeling of turbulence eddy density and velocity should be extended to the energy-containing subrange. A dimensionless function for describing the energy-containing subrange energy spectrum, developed by Pope [58], is reformulated in terms of the bubble size, $f\left(D_b^*\right)$, and applied to existing turbulent-driven interaction models.

- The strong intergroup transfer phenomenon happening in small diameter pipe flows is due to the enhancement of the wake entrainment effect by a small cross-section of the flow channel. It is related to two geometrical parameters, void fraction and relative bubble size to the pipe size. The increase of void fraction can lead to an increase of wake region volume behind the bubble, whereas the bubble size is associated with the wake volume per single bubble. The critical void fraction and bubble size are derived based on the geometrical relations among bubble size, wake region, and flow channel size. A transition function describing the effectiveness of the leading Group-1 bubble is developed in terms of the void fraction and relative bubble size.

- Along with the dimensionless function for turbulent eddy, the random collision model is modified to include the wall constraints on the bubble random motion in the radial direction.

- Theoretically in a small diameter pipe, a large bubble disintegration is not caused by the surface instability due to the small pipe size. Instead, it is because of the turbulent impact mechanism. The Group-2 turbulent impact model is derived based on Wu's and Kim's model [3], [4].

- The shearing-off model is revised based on Fu's model [8] which has unit inconsistency. The relative velocity at the rim of the large bubble is modified by considering the relative distance between the bubble and the pipe wall.

138

6.1.3 Evaluation of Newly Developed Interfacial Area Transport Model

The newly developed model is evaluated based on a comprehensive database for circular pipe flow with their inner diameter from 12.7 mm to 304.8 mm. These data are collected under similar experimental configurations by independent researchers. The evaluation result shows that the newly developed IATE models can give good predictions. Overall, the average absolute relative errors for the total IAC and void fraction less than 15%. The drastic intergroup transfer that happened in 12.7mm and 25.4mm test cases are predicted fairly well by the newly-derived models.

6.2 Recommendation for Future Work

The possible work to advance the topics related to the current study are summarized as follows:

- Besides the flow channel geometry, the entrance effect on the interfacial structure and interfacial area transport is also critically important. While the entrance effect has been well studied in the past, it is not well considered by the IATE models. In the experimental part, the entrance effect is highly determined by the design of two-phase flow injection systems, and the injector design can vary in different ways even if for the same design purposes. Another issue is how to physically add the entrance effect on the IATE bubble interaction models.

- Turbulence is fundamental to the bubble interactions, and it should be well modeled associated with the bubble interactions. The analysis of turbulence in the continuous phase requires the measurements of the continuous phase as support. Compared with the amount of experimental data for the dispersed phase, the amount of data for the continuous phase is still small.

- The current IATE is based on the deterministic assumption, that is, the next stage of the two-phase flow is determined based on the current stage. This assumption can be approximately accurate when the population of the target is large so that the real-world, probabilistic phenomena can be statistically modeled by the deterministic

models, similar to the Monte-Carlo method. However, the bubble interaction process is inherently a probabilistic process, which is the reason why there are many probabilistic correcting factors included in the models. In this sense, a probabilistic approach can be used for the modeling of interfacial area transport, in replace of the current form of the bubble interaction models.

REFERENCES

[1] M. Ishii and G. Kocamustafaogullari, "Two-phase flow models and their limitations," in *Advances in Two-Phase Flow and Heat Transfer*, Springer, 1983, pp. 1–14.

[2] G. Kocamustafaogullari and M. Ishii, "Foundation of the interfacial area transport equation and its closure relations," *International Journal of Heat and Mass Transfer*, vol. 38, no. 3, pp. 481–493, 1995.

[3] Q. Wu, S. Kim, M. Ishii, and S. Beus, "One-group interfacial area transport in vertical bubbly flow," *International Journal of Heat and Mass Transfer*, vol. 41, no. 8-9, pp. 1103–1112, 1998.

[4] S. Kim, "Interfacial area transport equation and measurement of local interfacial characteristics.," 1999.

[5] T. Hibiki and M. Ishii, "Experimental study on interfacial area transport in bubbly two-phase flows," *International Journal of Heat and Mass Transfer*, vol. 42, no. 16, pp. 3019–3035, 1999.

[6] X. Sun, "Two-group interfacial area transport equation for a confined test section," 2001.

[7] T. R. Smith, "Two-group interfacial area transport equation in large diameter pipes.," 2004.

[8] X. Fu and M. Ishii, "Two-group interfacial area transport in vertical air–water flow: I. mechanistic model," *Nuclear Engineering and Design*, vol. 219, no. 2, pp. 143–168, 2003.

[9] I. Kataoka, M. Ishii, and A. Serizawa, "Local formulation and measurements of interfacial area concentration in two-phase flow," *International Journal of Multiphase Flow*, vol. 12, no. 4, pp. 505–529, 1986.

[10] S. Revankar and M. Ishii, "Theory and measurement of local interfacial area using a four sensor probe in two-phase flow," *International journal of heat and mass transfer*, vol. 36, no. 12, pp. 2997–3007, 1993.

[11] S. Kim, X. Fu, X. Wang, and M. Ishii, "Development of the miniaturized four-sensor conductivity probe and the signal processing scheme," *International journal of heat and mass transfer*, vol. 43, no. 22, pp. 4101–4118, 2000.

[12] H. Goda, S. Kim, Y. Mi, J. P. Finch, M. Ishii, and J. Uhle, "Flow regime identification of co-current downward two-phase flow with neural network approach," in *International Conference on Nuclear Engineering*, vol. 35979, 2002, pp. 71–78.

[13] M. Ishii and S. Kim, "Development of one-group and two-group interfacial area transport equation," *Nuclear science and engineering*, vol. 146, no. 3, pp. 257–273, 2004.

[14] T. S. Worosz, "Interfacial area transport equation for bubbly to cap-bubbly transition flows," 2015.

[15] B. Ozar, "Interfacial area transport of steam-water two-phase flow in a vertical annulus at elevated pressures," Ph.D. dissertation, Purdue University, 2009.

[16] T. Hibiki and M. Ishii, "Two-group interfacial area transport equations at bubbly-to-slug flow transition," *Nuclear Engineering and Design*, vol. 202, no. 1, pp. 39–76, 2000.

[17] P. Vernier and J. Delhaye, "General two-phase flow equations applied to the thermo-hydrodynamics of boiling nuclear reactor," *Energie primaire*, vol. 4, no. 1, pp. 3–43, 1968.

[18] M. Ishii, "Thermo-fluid dynamic theory of two-phase flow," *NASA Sti/recon Technical Report A*, vol. 75, 1975.

[19] M. Ishii and K. Mishima, "Two-fluid model and hydrodynamic constitutive relations," *Nuclear Engineering and design*, vol. 82, no. 2-3, pp. 107–126, 1984.

[20] T. Hibiki and M. Ishii, "Interfacial area concentration of bubbly flow systems," *Chemical Engineering Science*, vol. 57, no. 18, pp. 3967–3977, 2002.

[21] X. Sun, S. Kim, M. Ishii, and S. G. Beus, "Model evaluation of two-group interfacial area transport equation for confined upward flow," *Nuclear engineering and design*, vol. 230, no. 1-3, pp. 27–47, 2004.

[22] G. Besagni, F. Inzoli, and T. Ziegenhein, "Two-phase bubble columns: A comprehensive review," *ChemEngineering*, vol. 2, no. 2, p. 13, 2018.

[23] G. Kocamustafaogullari and M. Ishii, "Interfacial area and nucleation site density in boiling systems," *International Journal of Heat and Mass Transfer*, vol. 26, no. 9, pp. 1377–1387, 1983.

[24] H.-S. Park, T.-H. Lee, T. Hibiki, W.-P. Baek, and M. Ishii, "Modeling of the condensation sink term in an interfacial area transport equation," *International journal of heat and mass transfer*, vol. 50, no. 25-26, pp. 5041–5053, 2007.

[25] Z. Dang, Y. Zhao, G. Wang, J. Du, and M. Ishii, "Two-phase interfacial area characteristics and transport under the transition from subcooled boiling to saturated boiling flows," *Applied Thermal Engineering*, vol. 184, p. 116 138, 2021.

[26] L. Florschuetz and B. Chao, "On the mechanics of vapor bubble collapse," 1965.

[27] J.-M. Le Corre, E. Hervieu, M. Ishii, and J.-M. Delhaye, "Benchmarking and improvements of measurement techniques for local-time-averaged two-phase flow parameters," *Experiments in fluids*, vol. 35, no. 5, pp. 448–458, 2003.

[28] H.-M. Prasser, A. Böttger, and J. Zschau, "A new electrode-mesh tomograph for gas–liquid flows," *Flow measurement and instrumentation*, vol. 9, no. 2, pp. 111–119, 1998.

[29] A. J. Dave, "Interfacial area transport equation models and validation against high resolution experimental data for small and large diameter vertical pipes.," Ph.D. dissertation, 2016.

[30] C.-H. Lin and T. Hibiki, "Databases of interfacial area concentration in gas–liquid two-phase flow," *Progress in Nuclear Energy*, vol. 74, pp. 91–102, 2014.

[31] Z. Dang, G. Wang, P. Ju, X. Yang, R. Bean, M. Ishii, S. Bajorek, and M. Bernard, "Experimental study of interfacial characteristics of vertical upward air-water two-phase flow in 25.4 mm id round pipe," *International Journal of Heat and Mass Transfer*, vol. 108, pp. 1825–1838, 2017.

[32] G. Wang, M. Zhang, and M. Ishii, "Flow structure of bubbly to slug transition flow in a small pipe," *International Journal of Heat and Mass Transfer*, vol. 147, p. 118 943, 2020.

[33] G. Wang, Q. Zhu, Z. Dang, X. Yang, and M. Ishii, "Prediction of interfacial area concentration in a small diameter round pipe," *International Journal of Heat and Mass Transfer*, vol. 130, pp. 252–265, 2019.

[34] Z. Dang, G. Wang, and M. Ishii, "Two-phase interfacial structure of bubbly-to-slug transition flows in a 12.7 mm id vertical tube," *International Journal of Heat and Mass Transfer*, vol. 165, p. 120 556, 2021.

[35] L. Neal and S. Bankoff, "A high resolution resistivity probe for determination of local void properties in gas-liquid flow," *AIChE Journal*, vol. 9, no. 4, pp. 490–494, 1963.

[36] X. Shen, Y. Saito, K. Mishima, and H. Nakamura, "Methodological improvement of an intrusive four-sensor probe for the multi-dimensional two-phase flow measurement," *International journal of multiphase flow*, vol. 31, no. 5, pp. 593–617, 2005.

[37] S. Revankar and M. Ishii, "Local interfacial area measurement in bubbly flow," *International journal of heat and mass transfer*, vol. 35, no. 4, pp. 913–925, 1992.

[38] J. P. Schlegel, S. Miwa, M. Griffiths, T. Hibiki, and M. Ishii, "Development of impedance void meter for evaluation of flow symmetry," *Annals of Nuclear Energy*, vol. 63, pp. 525–532, 2014.

[39] Y. Mi, M. Ishii, and L. Tsoukalas, "Flow regime identification methodology with neural networks and two-phase flow models," *Nuclear engineering and design*, vol. 204, no. 1-3, pp. 87–100, 2001.

[40] J. P. Schlegel, P. Sawant, S. Paranjape, B. Ozar, T. Hibiki, and M. Ishii, "Void fraction and flow regime in adiabatic upward two-phase flow in large diameter vertical pipes," *Nuclear Engineering and Design*, vol. 239, no. 12, pp. 2864–2874, 2009.

[41] Z. Dang, Y. Zhao, G. Wang, P. Ju, Q. Zhu, X. Yang, R. Bean, and M. Ishii, "Investigation of the effect of the electrode distance on the impedance void meter performance in the two-phase flow measurement," *Experimental Thermal and Fluid Science*, vol. 101, pp. 283–295, 2019.

[42] K. Mishima and M. Ishii, "Flow regime transition criteria for upward two-phase flow in vertical tubes," *International Journal of Heat and Mass Transfer*, vol. 27, no. 5, pp. 723–737, 1984.

[43] G. Wang, M. Zhang, Z. Dang, and M. Ishii, "Axial interfacial area transport and flow structure development in vertical upward bubbly and slug flow," *International Journal of Heat and Mass Transfer*, vol. 169, p. 120 919, 2021.

[44] F. Liang-Shih and K. Tsuchiya, *Bubble wake dynamics in liquids and liquid-solid suspensions*. Butterworth-Heinemann, 2013.

[45] W. L. Shew and J.-F. Pinton, "Dynamical model of bubble path instability," *Physical review letters*, vol. 97, no. 14, p. 144 508, 2006.

[46] T. Miyahara, K. Tsuchiya, and L.-S. Fan, "Wake properties of a single gas bubble in three-dimensional liquid-solid fluidized bed," *International journal of multiphase flow*, vol. 14, no. 6, pp. 749–763, 1988.

[47] H. Tsuge, "The motion of single gas bubbles rising in various liquids," *Kagaku Kogaku*, vol. 35, pp. 65–71, 1971.

[48] T. Takamasa, T. Goto, T. Hibiki, and M. Ishii, "Experimental study of interfacial area transport of bubbly flow in small-diameter tube," *International journal of multiphase flow*, vol. 29, no. 3, pp. 395–409, 2003.

[49] C. Grossetete, "Experimental investigation and preliminary numerical simulations of void profile development in a vertical cylindrical pipe," in *Proc. 2nd Int. Conf. on Multiphase Flow'95-Kyoto, Kyoto, Japan, Apr. 3-7, 1995*, 1995.

[50] M. Ishii, "One-dimensional drift-flux model and constitutive equations for relative motion between phases in various two-phase flow regimes," Argonne National Lab., Ill.(USA), Tech. Rep., 1977.

[51] T. Hibiki and M. Ishii, "Distribution parameter and drift velocity of drift-flux model in bubbly flow," *International Journal of Heat and Mass Transfer*, vol. 45, no. 4, pp. 707–721, 2002.

[52] T. Hibiki, S. Hogsett, and M. Ishii, "Local measurement of interfacial area, interfacial velocity and liquid turbulence in two-phase flow," *Nuclear engineering and design*, vol. 184, no. 2-3, pp. 287–304, 1998.

[53] R. Clift, J. R. Grace, and M. E. Weber, *Bubbles, drops, and particles*. Courier Corporation, 2005.

[54] D. Azbel and I. Athanasios, "A mechanism of liquid entrainment," *Handbook of Fluids in Motion*, pp. 453–482, 1983.

[55] M. J. Prince and H. W. Blanch, "Bubble coalescence and break-up in air-sparged bubble columns," *AIChE journal*, vol. 36, no. 10, pp. 1485–1499, 1990.

[56] T. Hibiki and M. Ishii, "Development of one-group interfacial area transport equation in bubbly flow systems," *International Journal of Heat and Mass Transfer*, vol. 45, no. 11, pp. 2351–2372, 2002.

[57] A. N. Kolmogorov, "Dissipation of energy in the locally isotropic turbulence," *Proceedings of the Royal Society of London. Series A: Mathematical and Physical Sciences*, vol. 434, no. 1890, pp. 15–17, 1991.

[58] S. B. Pope, *Turbulent flows*, 2001.

[59] J. P. Schlegel, "Multidimensional two-phase flow structure in systems with large diameter," Ph.D. dissertation, Purdue University, 2012.

[60] T. Hibiki, M. Ishii, and Z. Xiao, "Axial interfacial area transport of vertical bubbly flows," *International Journal of Heat and Mass Transfer*, vol. 44, no. 10, pp. 1869–1888, 2001.

[61] H. Schlichting, *Boundary-layer theory*. McGraw-Hill, New York, USA, 1979.

[62] T. Hibiki, T. Takamasa, and M. Ishii, "Interfacial area transport of bubbly flow in a small diameter pipe," *Journal of Nuclear Science and Technology*, vol. 38, no. 8, pp. 614–620, 2001.

[63] M. Ishii and T. Chawla, "Local drag laws in dispersed two-phase flow," *Nasa Sti/Recon Technical Report N*, vol. 80, 1979.

[64] C. S. Brooks, S. S. Paranjape, B. Ozar, T. Hibiki, and M. Ishii, "Two-group drift-flux model for closure of the modified two-fluid model," *International journal of heat and fluid flow*, vol. 37, pp. 196–208, 2012.

[65] R. Moissis and P. Griffith, "Entrance effects in a two-phase slug flow," 1962.

[66] G. Evans, G. Jameson, and B. Atkinson, "Prediction of the bubble size generated by a plunging liquid jet bubble column," *Chemical engineering science*, vol. 47, no. 13-14, pp. 3265–3272, 1992.

[67] J. Miller, M. Ishii, and S. Revankar, "An experimental analysis of larger sphrical cap bubbles rising in an extend liquid," Purdue University, IN (USA), Tech. Rep., 1993.

[68] Y. Sato and K. Sekoguchi, "Liquid velocity distribution in two-phase bubble flow," *International Journal of Multiphase Flow*, vol. 2, no. 1, pp. 79–95, 1975.

[69] J. P. Schlegel, T. Hibiki, and M. Ishii, "Two-group modeling of interfacial area transport in large diameter channels," *Nuclear Engineering and Design*, vol. 293, pp. 75–86, 2015.

A. Evaluation Results with Newly Developed IATE Model

Pipe diameter:12.7 mm; $\langle j_f \rangle : 0.33$ m/s; $\langle j_{g,0} \rangle : 0.078$ m/s.
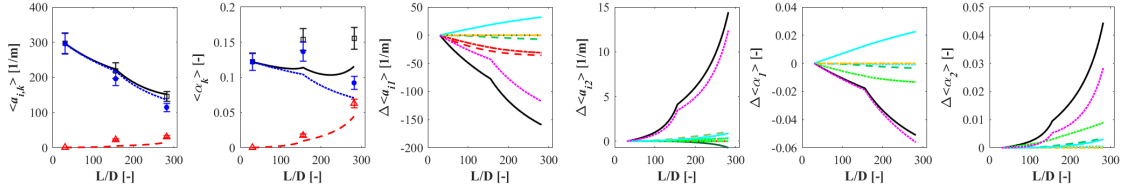
Pipe diameter:12.7 mm; $\langle j_f \rangle : 0.36$ m/s; $\langle j_{g,0} \rangle : 0.156$ m/s.
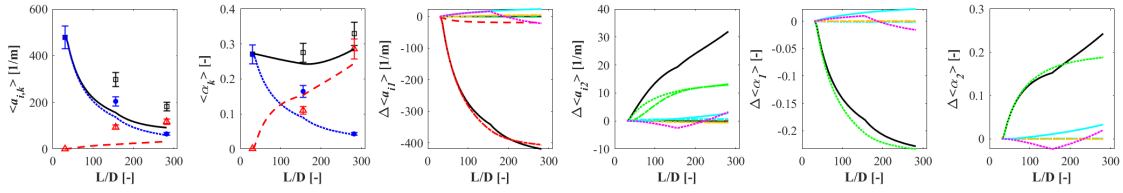
Pipe diameter:12.7 mm; $\langle j_f \rangle : 0.38$ m/s; $\langle j_{g,0} \rangle : 0.308$ m/s.
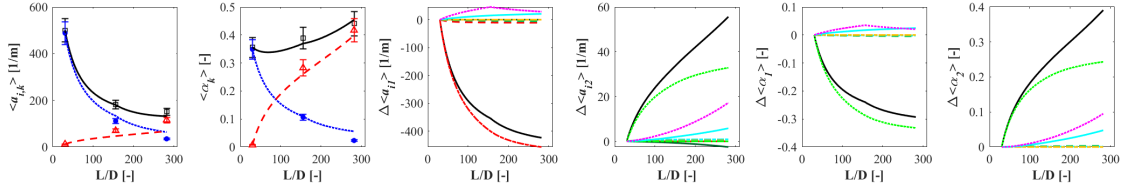

Pipe diameter:12.7 mm; $\langle j_f \rangle : 0.35$ m/s; $\langle j_{g,0} \rangle : 0.462$ m/s.
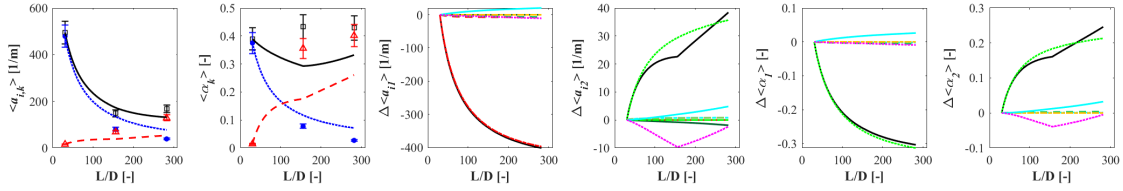
Pipe diameter:12.7 mm; $\langle j_f \rangle : 0.31$ m/s; $\langle j_{g,0} \rangle : 0.772$ m/s.
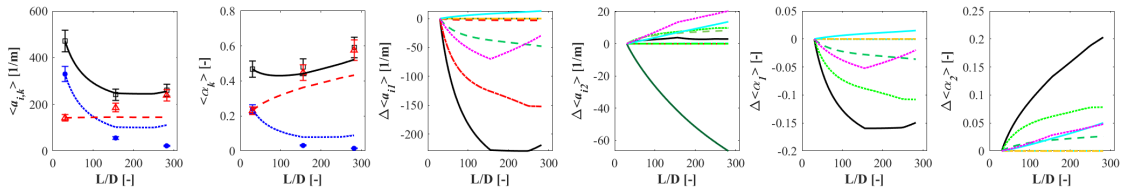
Pipe diameter:12.7 mm; $\langle j_f \rangle$: 0.53 m/s; $\langle j_{g,0} \rangle$: 0.151 m/s.
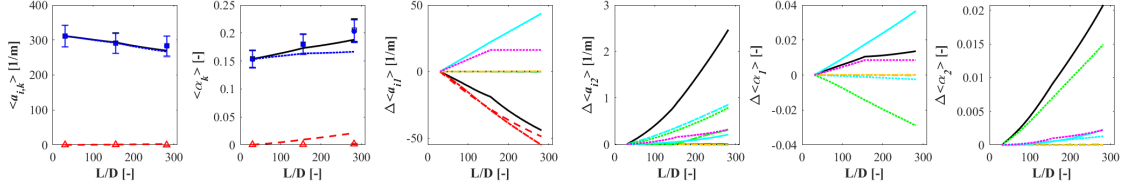
Pipe diameter:12.7 mm; $\langle j_f \rangle$: 0.51 m/s; $\langle j_{g,0} \rangle$: 0.339 m/s.
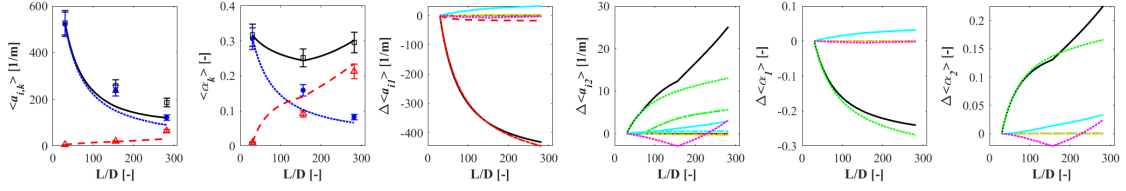
Pipe diameter:12.7 mm; $\langle j_f \rangle$: 0.51 m/s; $\langle j_{g,0} \rangle$: 0.475 m/s.
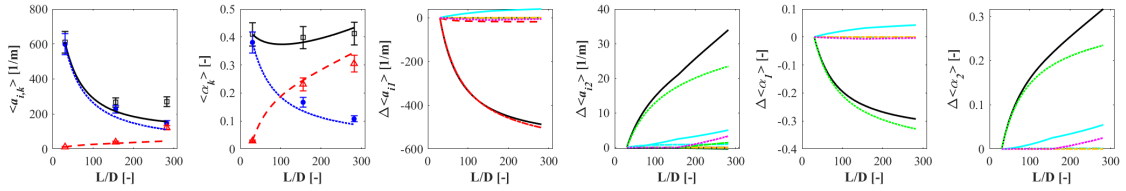
Pipe diameter:12.7 mm; $\langle j_f \rangle$: 0.54 m/s; $\langle j_{g,0} \rangle$: 0.679 m/s.
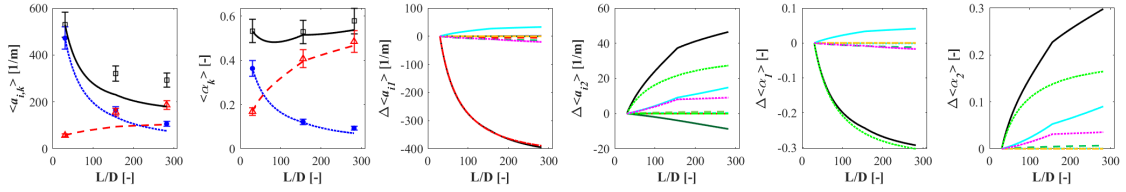
Pipe diameter:12.7 mm; $\langle j_f \rangle$: 0.53 m/s; $\langle j_{g,0} \rangle$: 0.966 m/s.

148
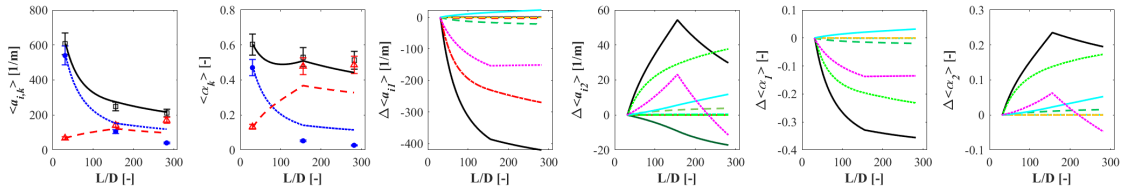
Pipe diameter:12.7 mm; $\langle j_f \rangle$: 0.99 m/s; $\langle j_{g,0} \rangle$: 0.161 m/s.
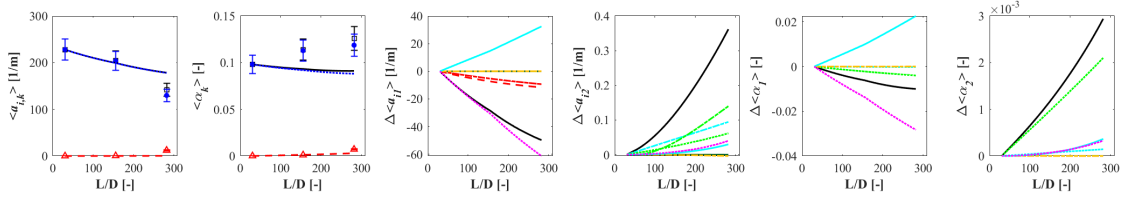

Pipe diameter:12.7 mm; $\langle j_f \rangle$: 0.95 m/s; $\langle j_{g,0} \rangle$: 0.270 m/s.
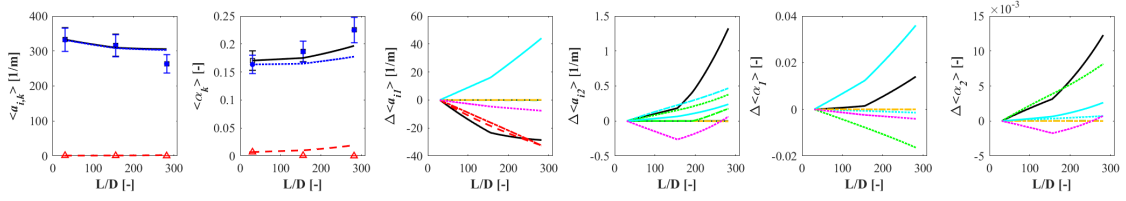
Pipe diameter:12.7 mm; $\langle j_f \rangle$: 0.97 m/s; $\langle j_{g,0} \rangle$: 0.463 m/s.
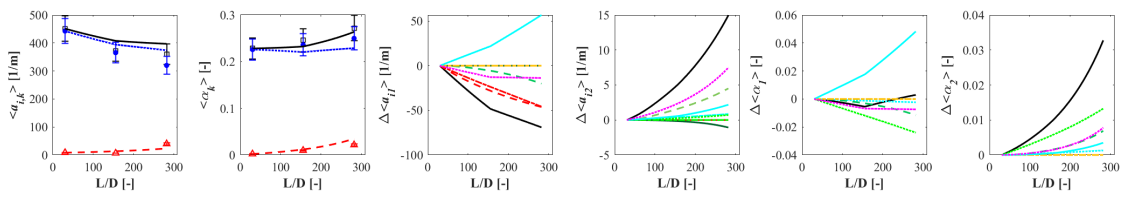
Pipe diameter:12.7 mm; $\langle j_f \rangle$: 0.96 m/s; $\langle j_{g,0} \rangle$: 0.610 m/s.
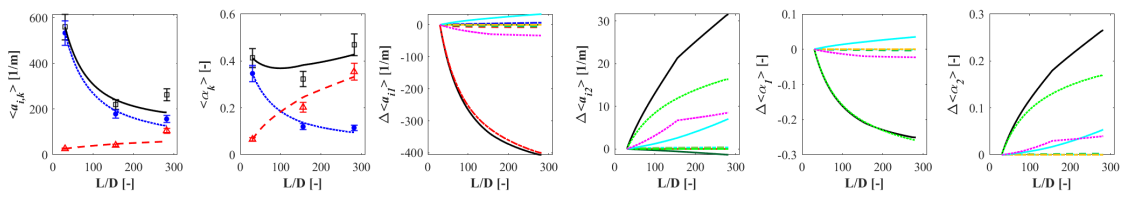
Pipe diameter:12.7 mm; $\langle j_f \rangle$: 0.98 m/s; $\langle j_{g,0} \rangle$: 0.966 m/s.
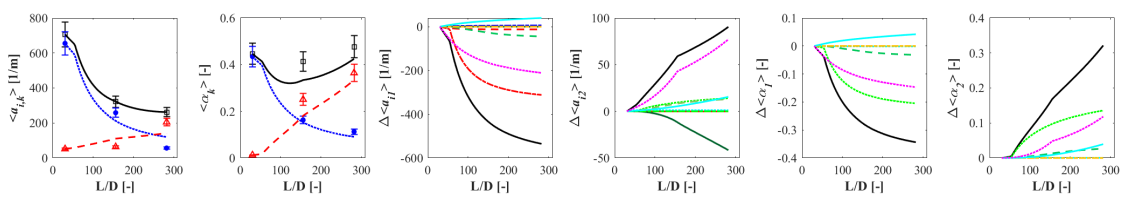
Pipe diameter:12.7 mm; $\langle j_f \rangle$: 0.99 m/s; $\langle j_{g,0} \rangle$: 1.235 m/s.
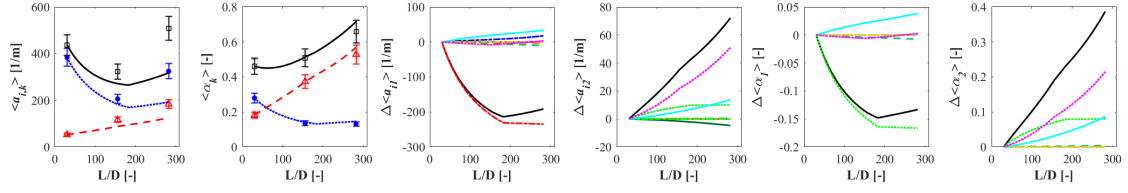
Pipe diameter:12.7 mm; $\langle j_f \rangle$: 1.98 m/s; $\langle j_{g,0} \rangle$: 0.335 m/s.
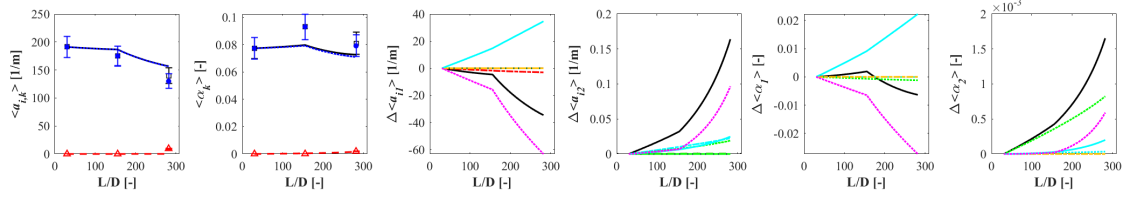
Pipe diameter:12.7 mm; $\langle j_f \rangle$: 1.95 m/s; $\langle j_{g,0} \rangle$: 0.502 m/s.
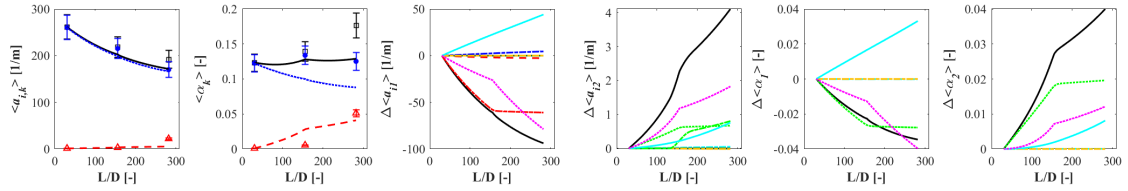
Pipe diameter:12.7 mm; $\langle j_f \rangle$: 2.00 m/s; $\langle j_{g,0} \rangle$: 0.669 m/s.
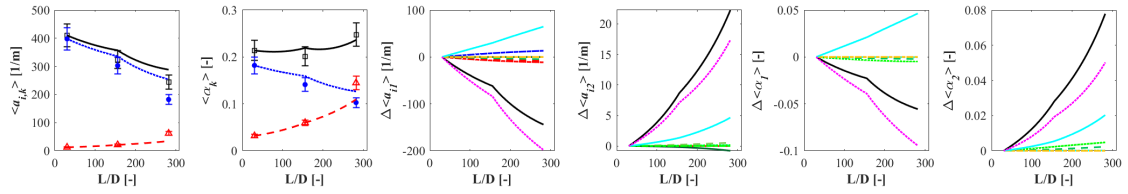
Pipe diameter:12.7 mm; $\langle j_f \rangle$: 1.98 m/s; $\langle j_{g,0} \rangle$: 0.837 m/s.
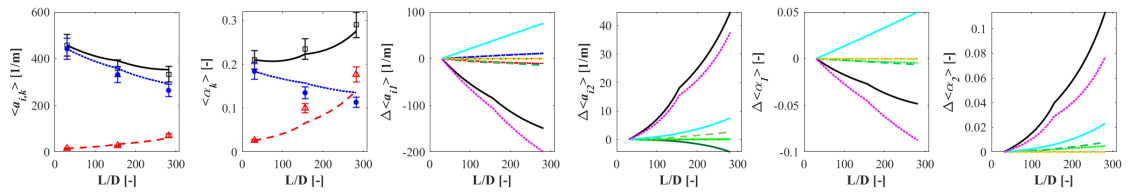
Pipe diameter:12.7 mm; $\langle j_f \rangle$: 1.98 m/s; $\langle j_{g,0} \rangle$: 1.088 m/s.
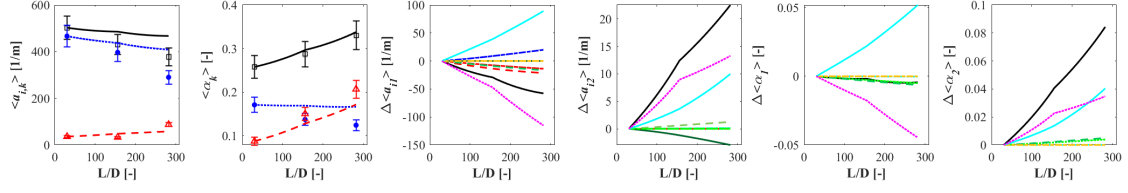
Pipe diameter:12.7 mm; $\langle j_f \rangle$: 1.99 m/s; $\langle j_{g,0} \rangle$: 1.689 m/s.
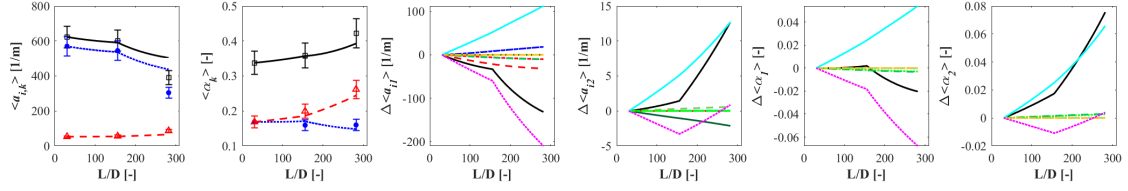
Pipe diameter:12.7 mm; $\langle j_f \rangle$: 2.00 m/s; $\langle j_{g,0} \rangle$: 2.301 m/s.
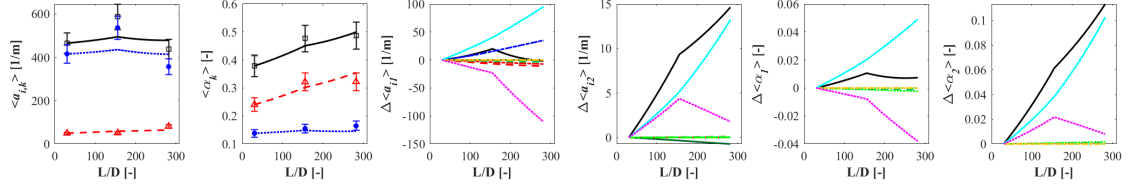
Pipe diameter:25.4 mm; $\langle j_f \rangle$: 0.50 m/s; $\langle j_{g,0} \rangle$: 0.09 m/s.
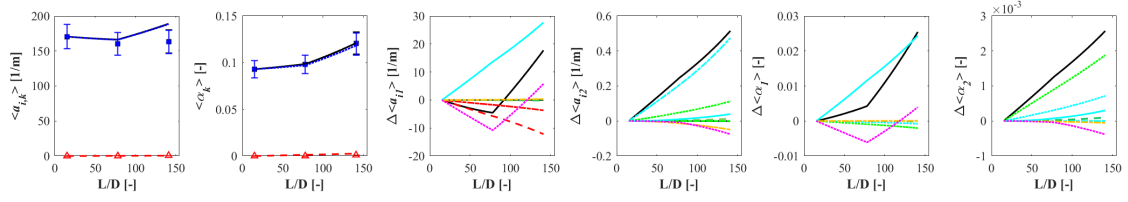
Pipe diameter:25.4 mm; $\langle j_f \rangle$: 0.50 m/s; $\langle j_{g,0} \rangle$: 0.14 m/s.
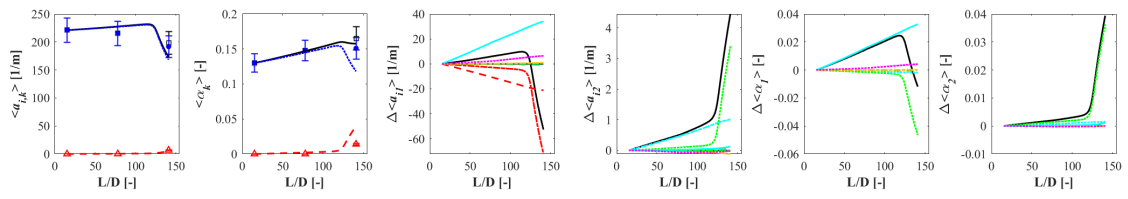
Pipe diameter:25.4 mm; $\langle j_f \rangle$: 0.50 m/s; $\langle j_{g,0} \rangle$: 0.20 m/s.
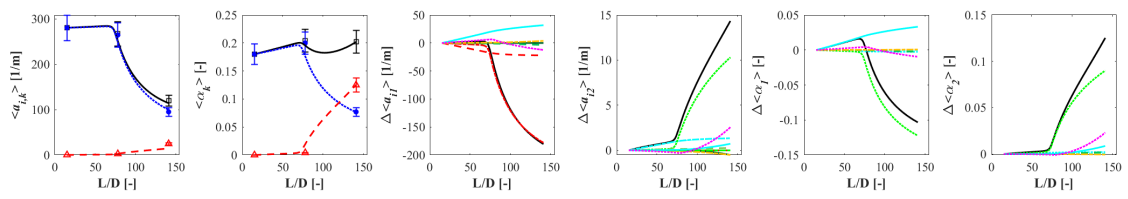
Pipe diameter:25.4 mm; $\langle j_f \rangle$: 0.50 m/s; $\langle j_{g,0} \rangle$: 0.26 m/s.
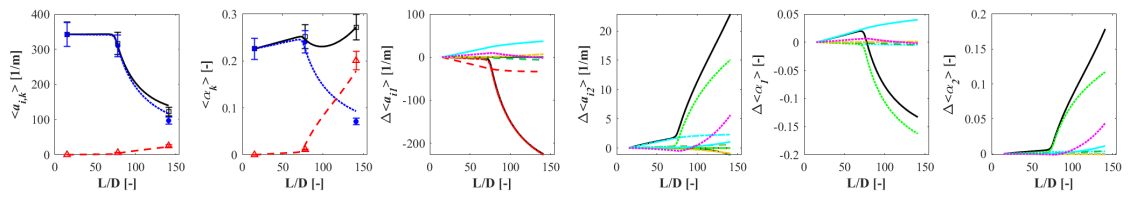
Pipe diameter:25.4 mm; $\langle j_f \rangle$: 0.50 m/s; $\langle j_{g,0} \rangle$: 0.33 m/s.
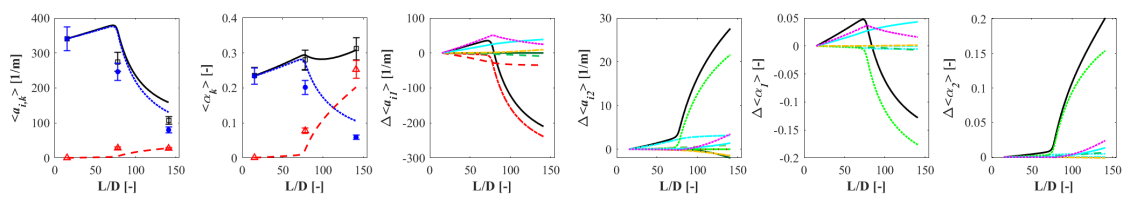
Pipe diameter:25.4 mm; $\langle j_f \rangle$: 0.50 m/s; $\langle j_{g,0} \rangle$: 0.42 m/s.
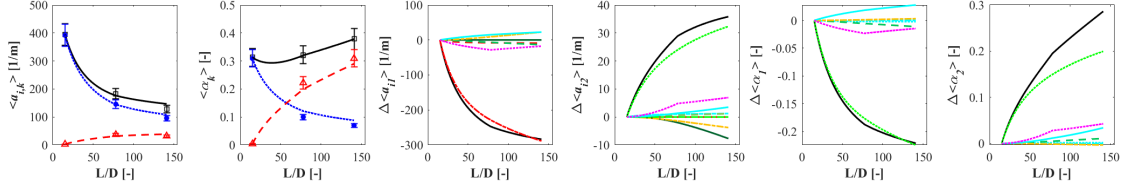
Pipe diameter:25.4 mm; $\langle j_f \rangle$: 0.50 m/s; $\langle j_{g,0} \rangle$: 0.65 m/s.
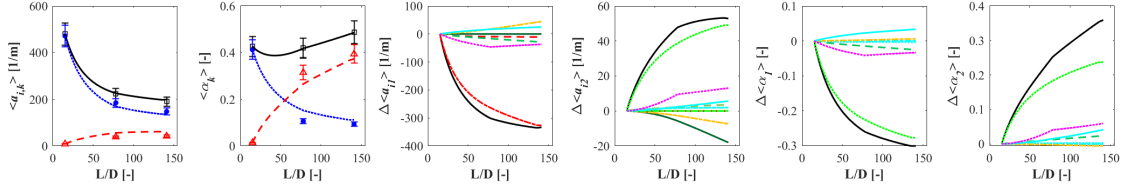
Pipe diameter:25.4 mm; $\langle j_f \rangle$: 0.50 m/s; $\langle j_{g,0} \rangle$: 1.35 m/s.
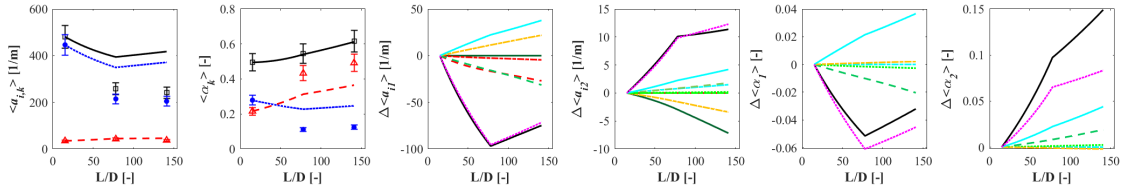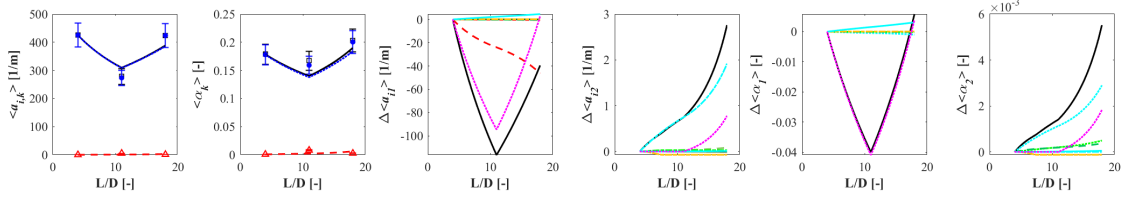

Pipe diameter:25.4 mm; $\langle j_f \rangle$: 1.00 m/s; $\langle j_{g,0} \rangle$: 0.15 m/s.
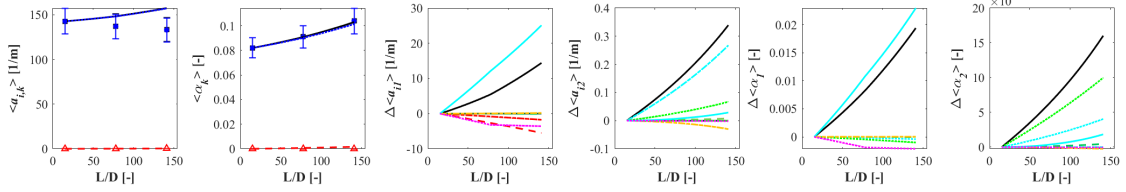
Pipe diameter:25.4 mm; $\langle j_f \rangle$: 1.00 m/s; $\langle j_{g,0} \rangle$: 0.25 m/s.
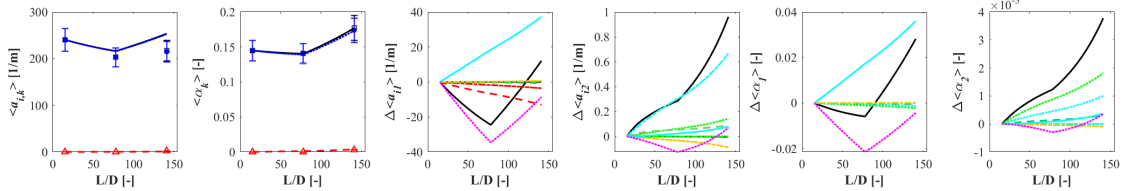
Pipe diameter:25.4 mm; $\langle j_f \rangle$: 1.00 m/s; $\langle j_{g,0} \rangle$: 0.35 m/s.
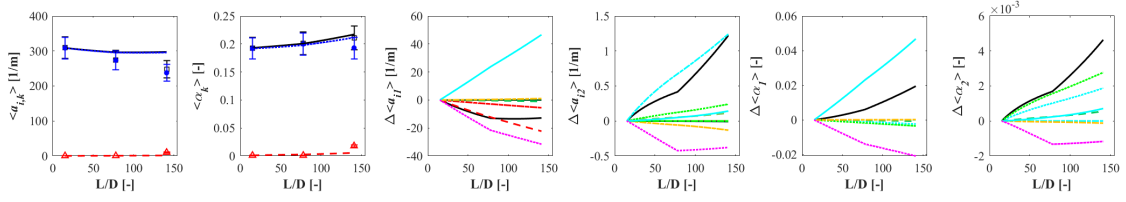
Pipe diameter:25.4 mm; $\langle j_f \rangle$: 1.00 m/s; $\langle j_{g,0} \rangle$: 0.48 m/s.
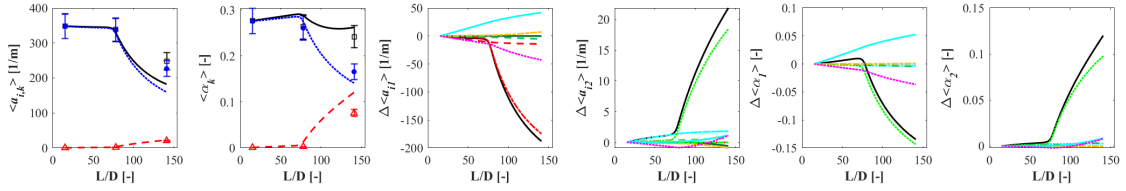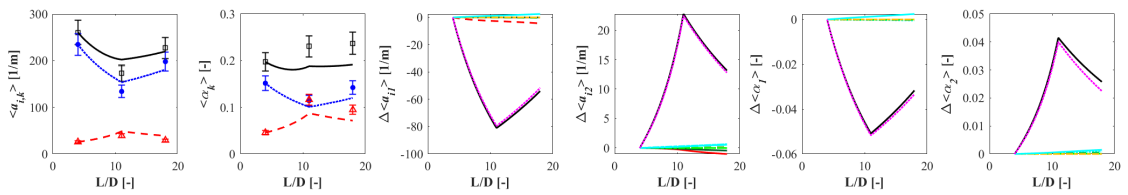

Pipe diameter:25.4 mm; $\langle j_f \rangle$: 1.00 m/s; $\langle j_{g,0} \rangle$: 0.61 m/s.
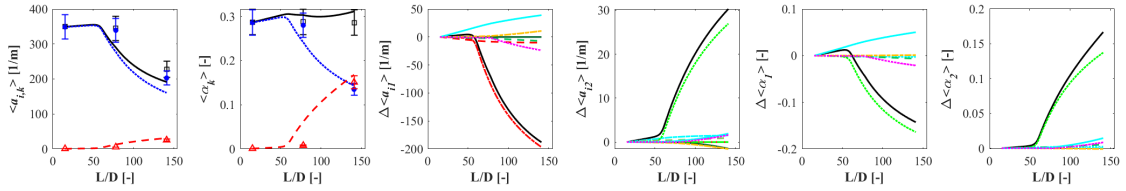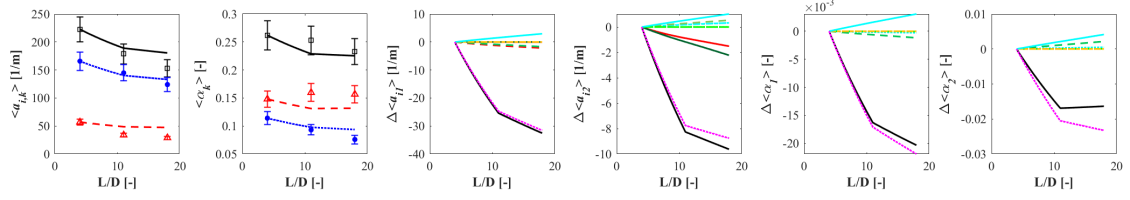

Pipe diameter:25.4 mm; $\langle j_f \rangle$: 1.00 m/s; $\langle j_{g,0} \rangle$: 0.78 m/s.
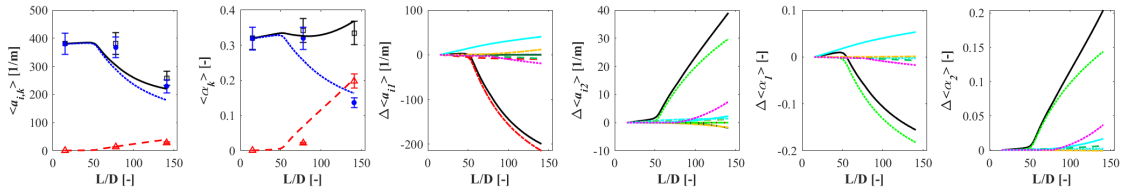
Pipe diameter:25.4 mm; $\langle j_f \rangle$: 1.00 m/s; $\langle j_{g,0} \rangle$: 1.23 m/s.
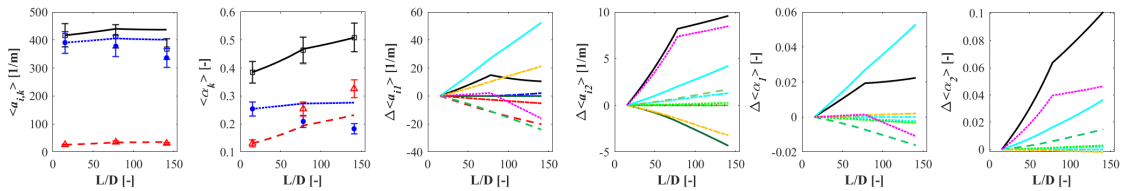
Pipe diameter:25.4 mm; $\langle j_f \rangle$: 1.00 m/s; $\langle j_{g,0} \rangle$: 2.60 m/s.
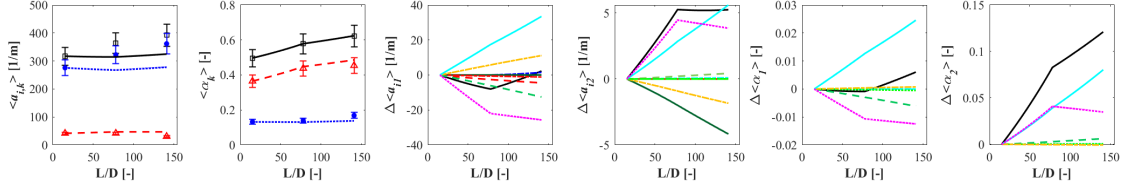
Pipe diameter:25.4 mm; $\langle j_f \rangle$: 2.00 m/s; $\langle j_{g,0} \rangle$: 0.29 m/s.
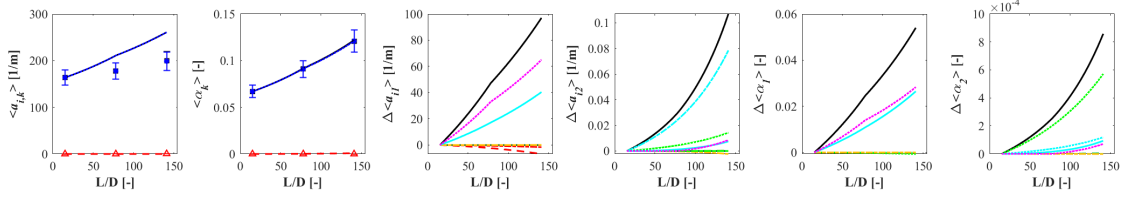

Pipe diameter:25.4 mm; $\langle j_f \rangle$: 2.00 m/s; $\langle j_{g,0} \rangle$: 0.46 m/s.
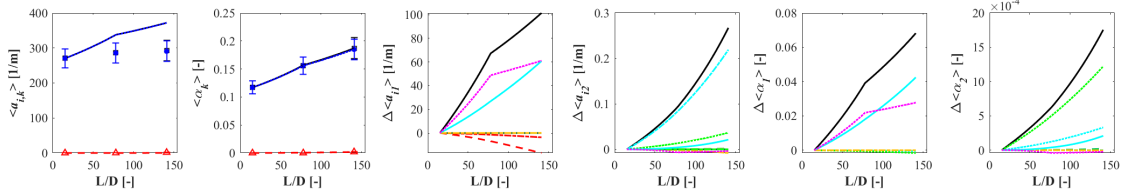
Pipe diameter:25.4 mm; $\langle j_f \rangle$: 2.00 m/s; $\langle j_{g,0} \rangle$: 0.66 m/s.
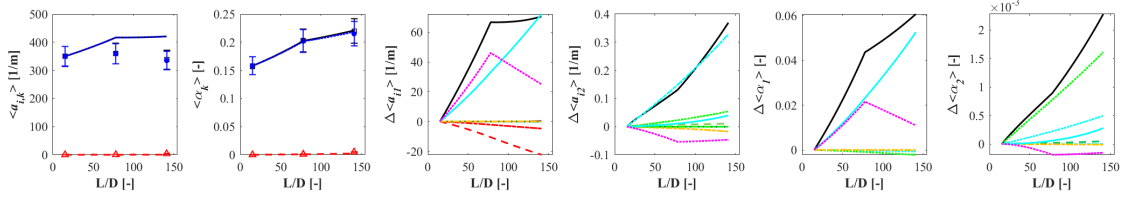
Pipe diameter:25.4 mm; $\langle j_f \rangle$: 2.00 m/s; $\langle j_{g,0} \rangle$: 0.90 m/s.
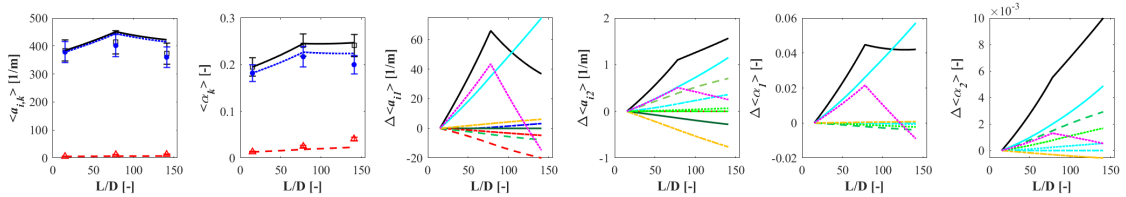
Pipe diameter:25.4 mm; $\langle j_f \rangle$: 2.00 m/s; $\langle j_{g,0} \rangle$: 1.17 m/s.
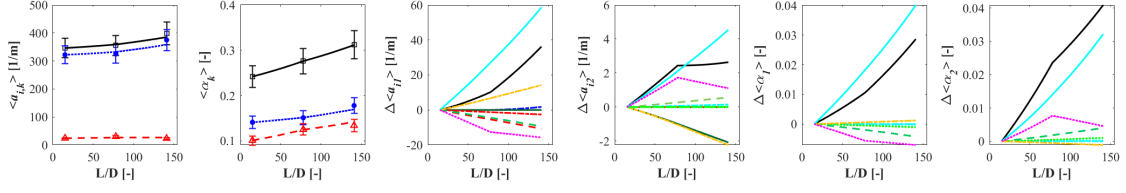
Pipe diameter:25.4 mm; $\langle j_f \rangle$: 2.00 m/s; $\langle j_{g,0} \rangle$: 1.50 m/s.
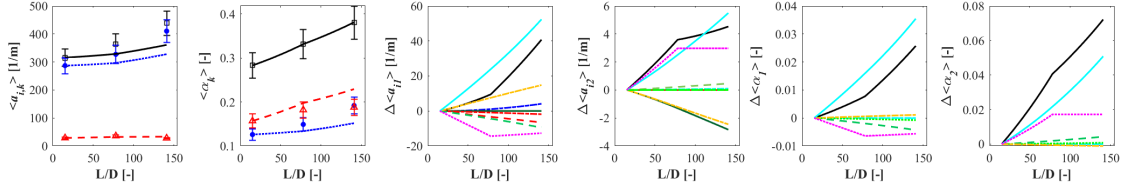
Pipe diameter:25.4 mm; $\langle j_f \rangle$: 2.00 m/s; $\langle j_{g,0} \rangle$: 2.40 m/s.
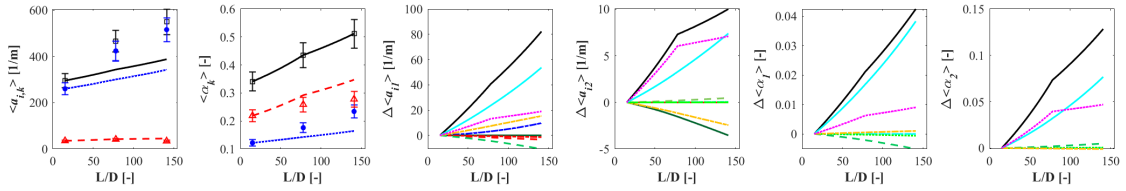
Pipe diameter:25.4 mm; $\langle j_f \rangle$: 2.00 m/s; $\langle j_{g,0} \rangle$: 5.00 m/s.
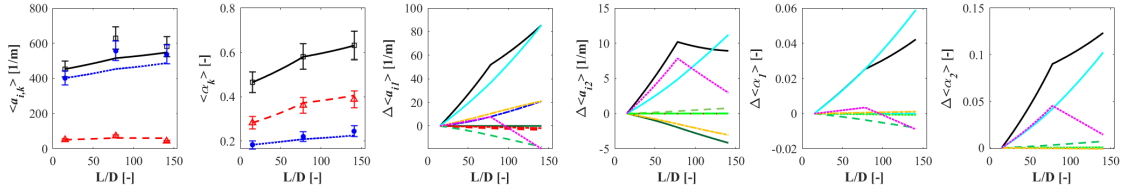
Pipe diameter:50.8 mm; $\langle j_f \rangle$: 2.00 m/s; $\langle j_{g,0} \rangle$: 0.262 m/s.
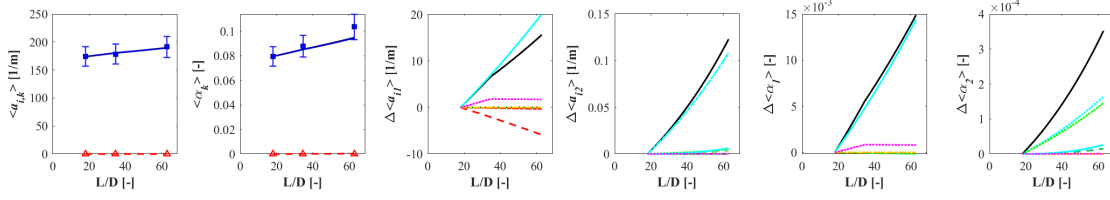
Pipe diameter:50.8 mm; $\langle j_f \rangle$: 2.00 m/s; $\langle j_{g,0} \rangle$: 0.366 m/s.
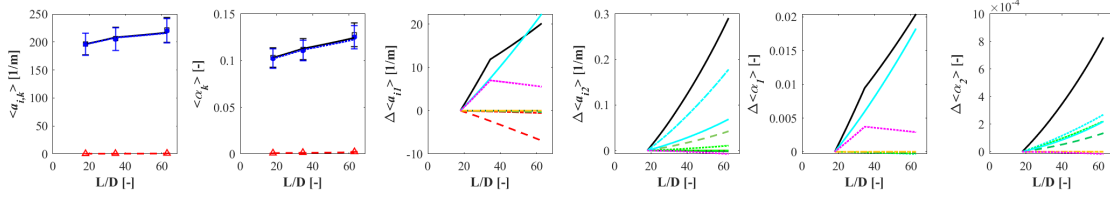
Pipe diameter:50.8 mm; $\langle j_f \rangle$: 2.00 m/s; $\langle j_{g,0} \rangle$: 0.418 m/s.
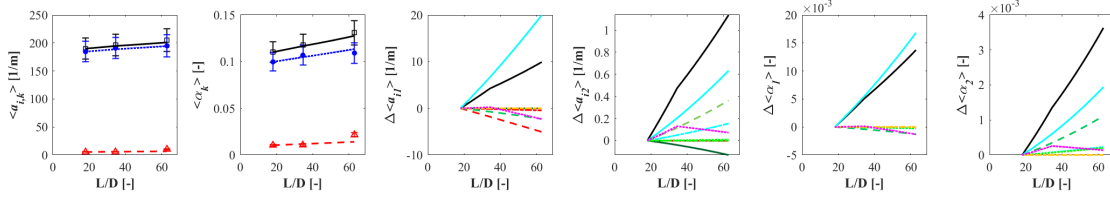
Pipe diameter:50.8 mm; $\langle j_f \rangle$: 2.00 m/s; $\langle j_{g,0} \rangle$: 0.471 m/s.
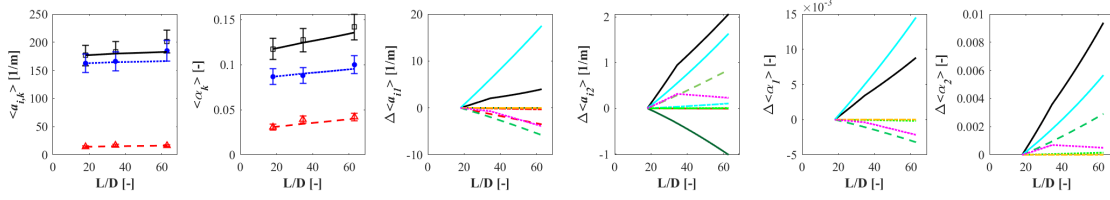
Pipe diameter:50.8 mm; $\langle j_f \rangle$: 2.00 m/s; $\langle j_{g,0} \rangle$: 0.703 m/s.

157
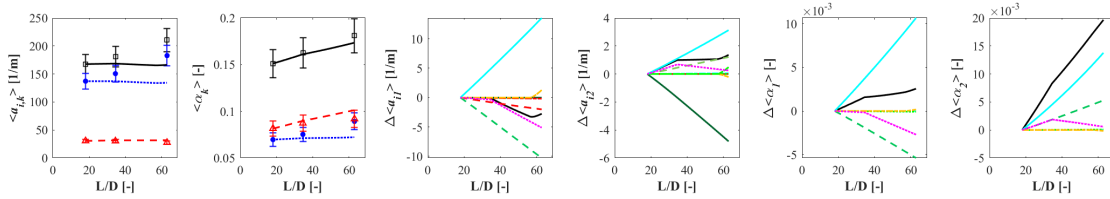
Pipe diameter:50.8 mm; $\langle j_f \rangle$: 2.00 m/s; $\langle j_{g,0} \rangle$: 1.074 m/s.
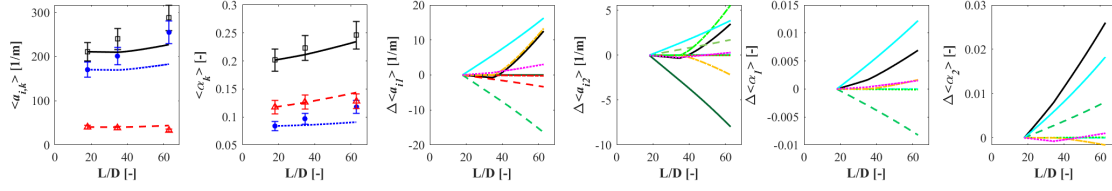
Pipe diameter:50.8 mm; $\langle j_f \rangle$: 1.00 m/s; $\langle j_{g,0} \rangle$: 0.349 m/s.
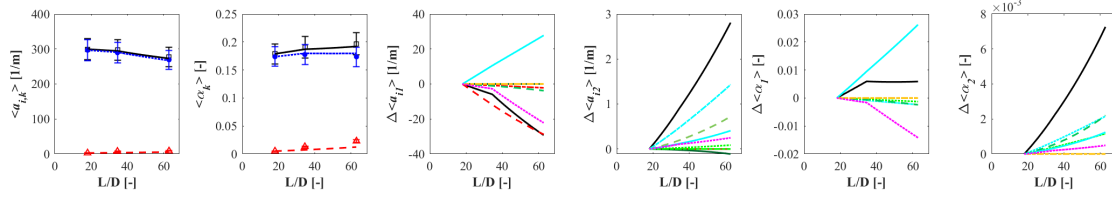
Pipe diameter:50.8 mm; $\langle j_f \rangle$: 1.00 m/s; $\langle j_{g,0} \rangle$: 0.400 m/s.
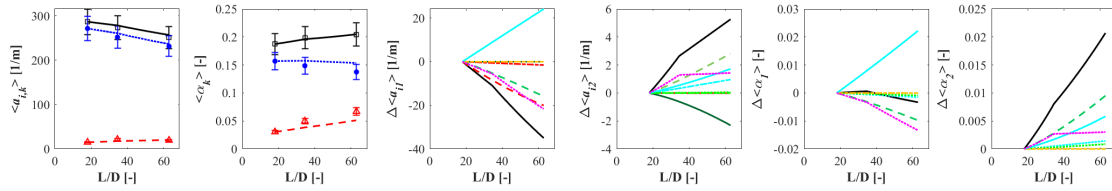
Pipe diameter:50.8 mm; $\langle j_f \rangle$: 1.00 m/s; $\langle j_{g,0} \rangle$: 0.647 m/s.

158
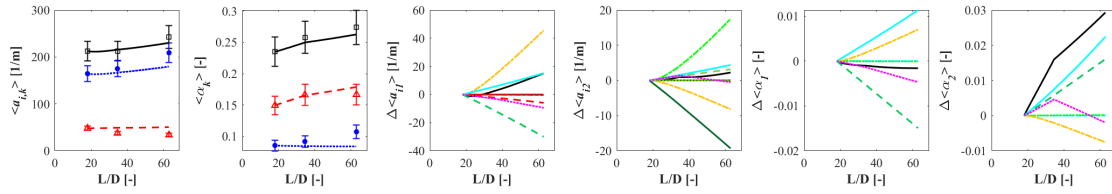
Pipe diameter:101.6 mm; $\langle j_f \rangle$: 0.06 m/s; $\langle j_{g,0} \rangle$: 0.05 m/s.
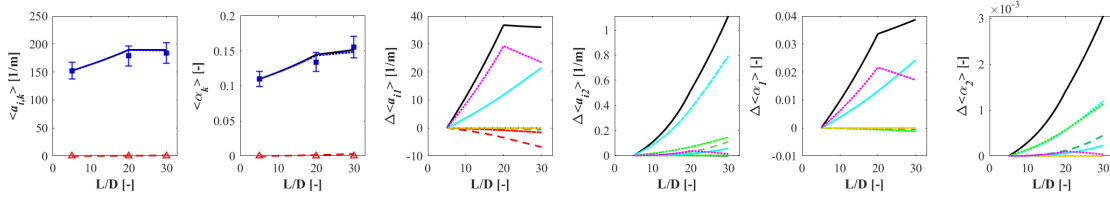
Pipe diameter:101.6 mm; $\langle j_f \rangle$: 0.26 m/s; $\langle j_{g,0} \rangle$: 0.05 m/s.
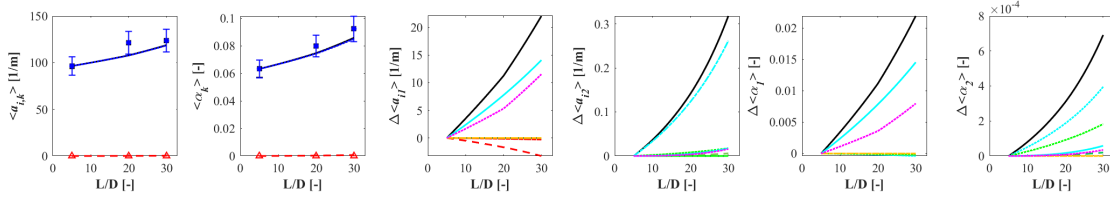
Pipe diameter:101.6 mm; $\langle j_f \rangle$: 1.02 m/s; $\langle j_{g,0} \rangle$: 0.05 m/s.
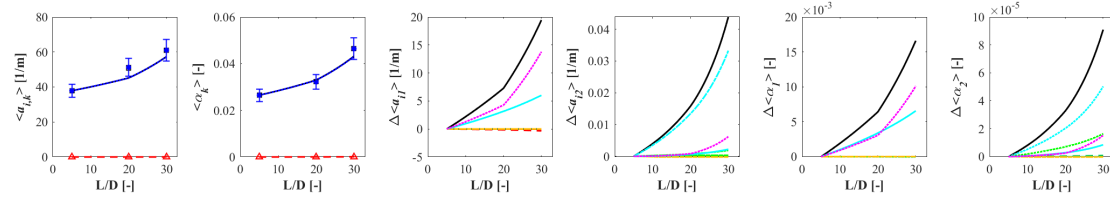
Pipe diameter:101.6 mm; $\langle j_f \rangle$: 1.21 m/s; $\langle j_{g,0} \rangle$: 0.10 m/s.
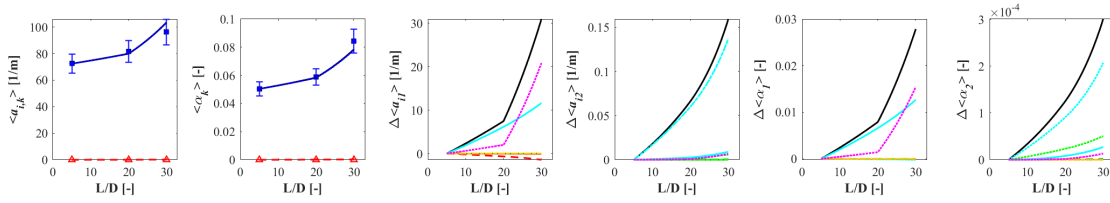
Pipe diameter:101.6 mm; $\langle j_f \rangle$: 0.06 m/s; $\langle j_{g,0} \rangle$: 0.13 m/s.

159
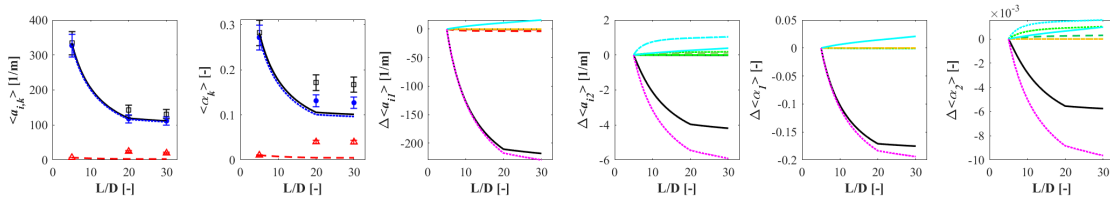
Pipe diameter:101.6 mm; $\langle j_f \rangle$: 0.06 m/s; $\langle j_{g,0} \rangle$: 0.28 m/s.
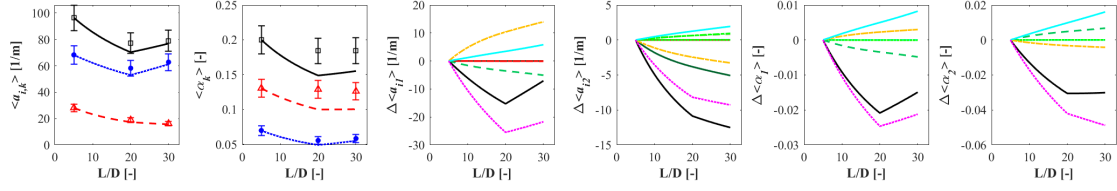
Pipe diameter:101.6 mm; $\langle j_f \rangle$: 0.26 m/s; $\langle j_{g,0} \rangle$: 0.12 m/s.
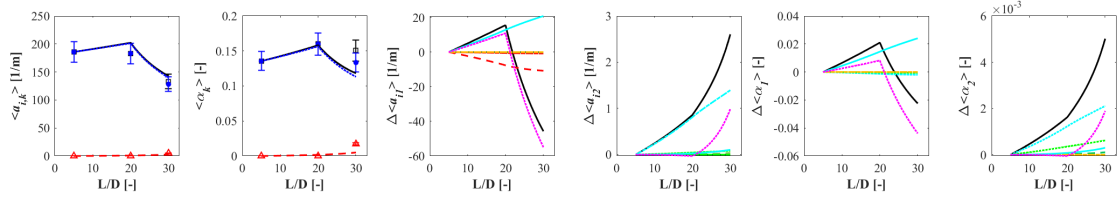
Pipe diameter:101.6 mm; $\langle j_f \rangle$: 0.26 m/s; $\langle j_{g,0} \rangle$: 0.34 m/s.
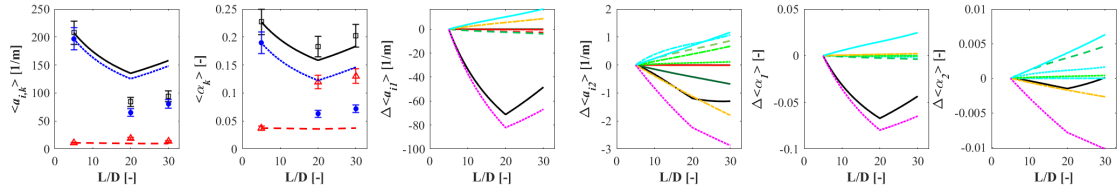

Pipe diameter:101.6 mm; $\langle j_f \rangle$: 1.03 m/s; $\langle j_{g,0} \rangle$: 0.28 m/s.
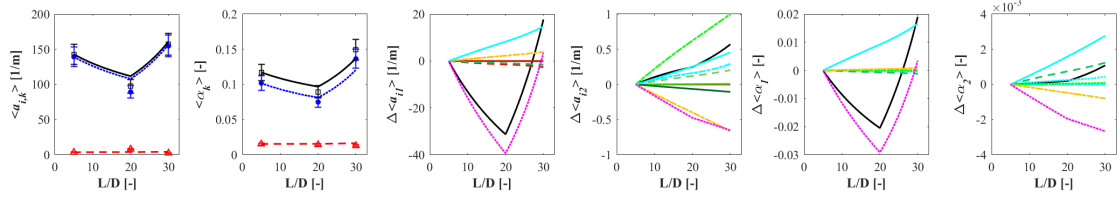
Pipe diameter:101.6 mm; $\langle j_f \rangle$: 1.03 m/s; $\langle j_{g,0} \rangle$: 0.50 m/s.
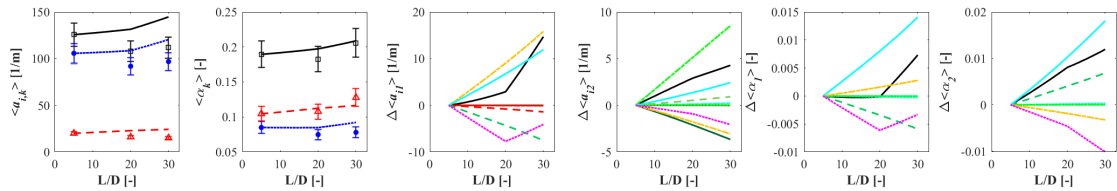
Pipe diameter:101.6 mm; $\langle j_f \rangle$: 0.05 m/s; $\langle j_{g,0} \rangle$: 0.75 m/s.
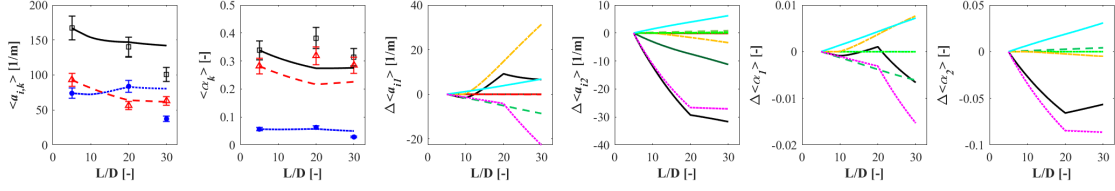
Pipe diameter:101.6 mm; $\langle j_f \rangle$: 0.25 m/s; $\langle j_{g,0} \rangle$: 0.75 m/s.
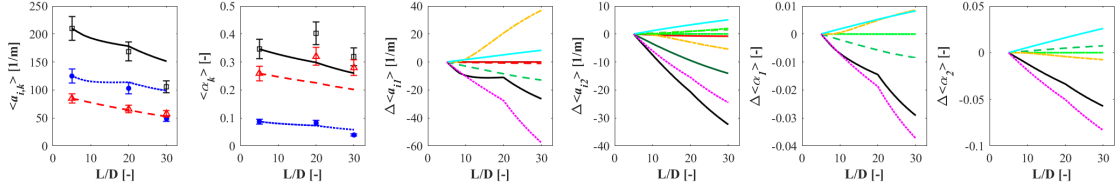
Pipe diameter:101.6 mm; $\langle j_f \rangle$: 1.00 m/s; $\langle j_{g,0} \rangle$: 1.00 m/s.
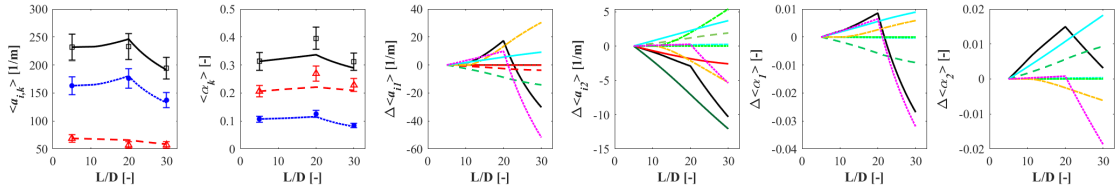
Pipe diameter:101.6 mm; $\langle j_f \rangle$: 0.25 m/s; $\langle j_{g,0} \rangle$: 3.00 m/s.
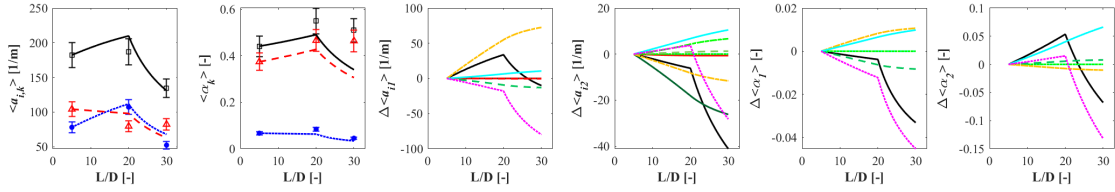
Pipe diameter:101.6 mm; $\langle j_f \rangle$: 0.20 m/s; $\langle j_{g,0} \rangle$: 3.00 m/s.

161
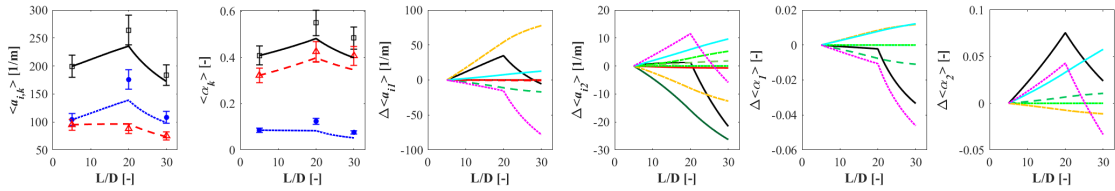
Pipe diameter:101.6 mm; $\langle j_f \rangle$: 0.20 m/s; $\langle j_{g,0} \rangle$: 8.00 m/s.
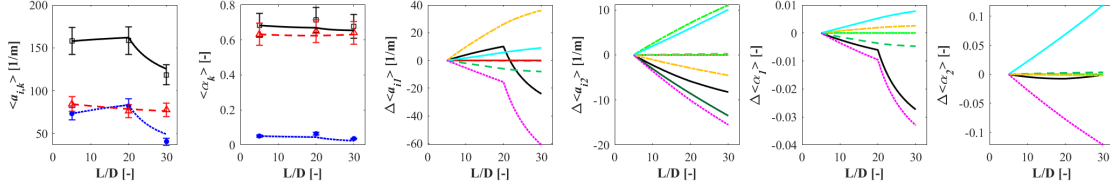
Pipe diameter:101.6 mm; $\langle j_f \rangle$: 1.00 m/s; $\langle j_{g,0} \rangle$: 4.00 m/s.
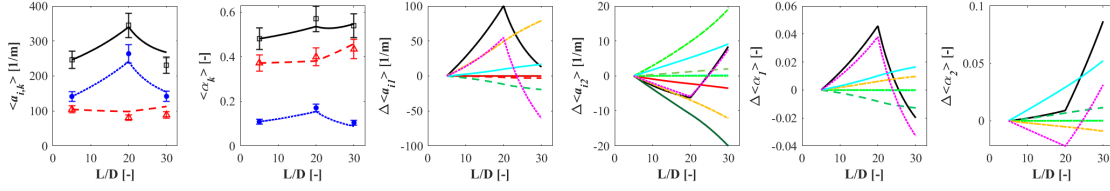
Pipe diameter:101.6 mm; $\langle j_f \rangle$: 1.00 m/s; $\langle j_{g,0} \rangle$: 8.00 m/s.
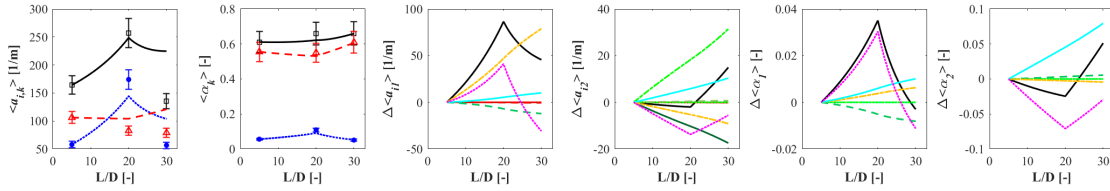
Pipe diameter:101.6 mm; $\langle j_f \rangle$: 2.00 m/s; $\langle j_{g,0} \rangle$: 7.00 m/s.

162
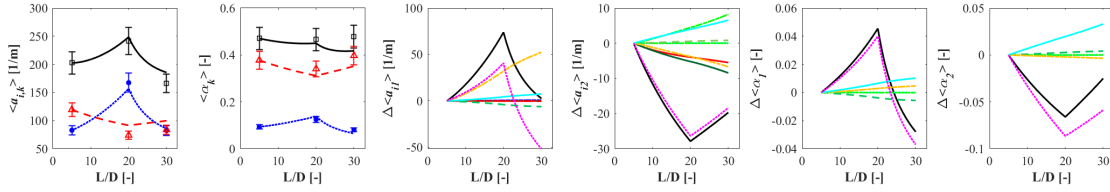
Pipe diameter:152.4 mm; $\langle j_f \rangle : 0.05$ m/s; $\langle j_{g,0} \rangle : 0.04$ m/s.
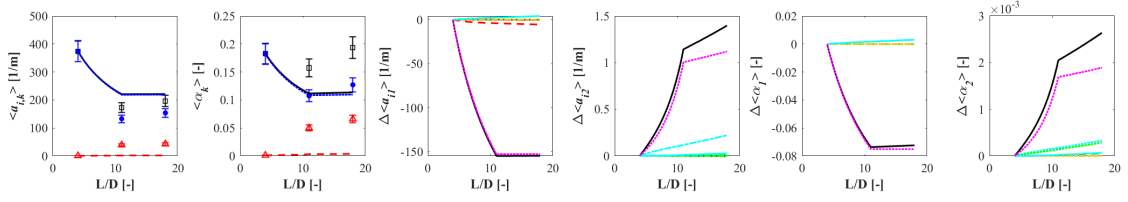
Pipe diameter:152.4 mm; $\langle j_f \rangle : 0.05$ m/s; $\langle j_{g,0} \rangle : 0.07$ m/s.
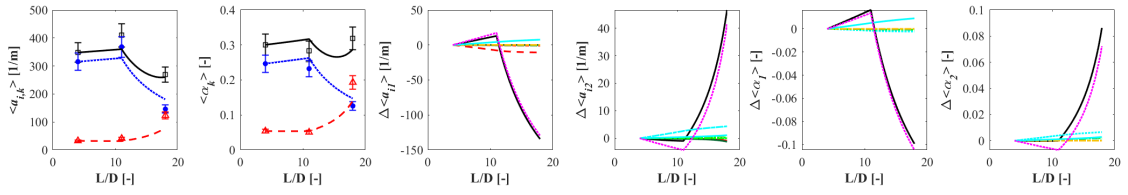
Pipe diameter:152.4 mm; $\langle j_f \rangle : 0.05$ m/s; $\langle j_{g,0} \rangle : 0,15$ m/s.
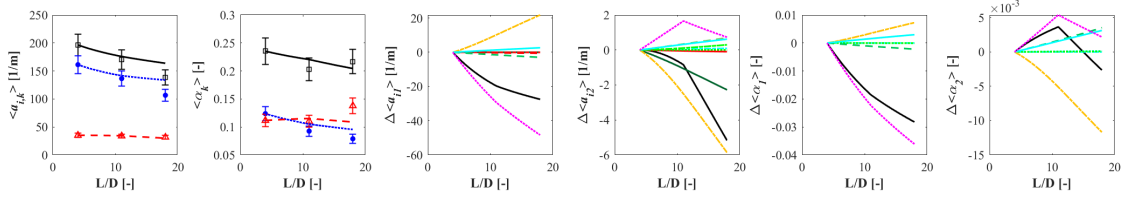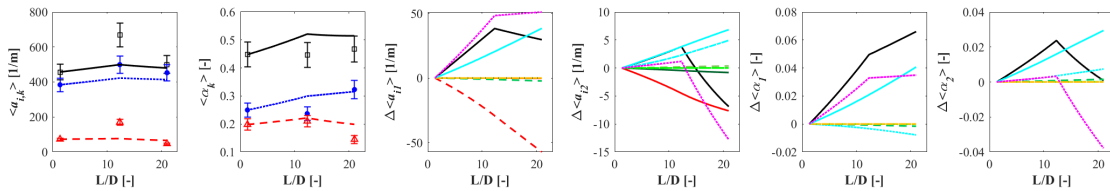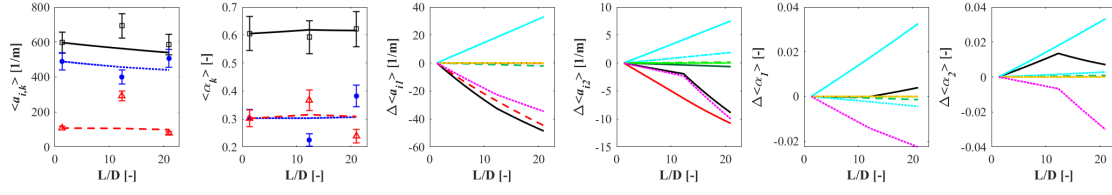
Pipe diameter:152.4 mm; $\langle j_f \rangle : 0.30$ m/s; $\langle j_{g,0} \rangle : 0.07$ m/s.

Pipe diameter:152.4 mm; $\langle j_f \rangle : 0.30$ m/s; $\langle j_{g,0} \rangle : 0.15$ m/s.

163

Pipe diameter:152.4 mm; $\langle j_f \rangle$: 0.30 m/s; $\langle j_{g,0} \rangle$: 0.30 m/s.

Pipe diameter:152.4 mm; $\langle j_f \rangle$: 1.00 m/s; $\langle j_{g,0} \rangle$: 0.10 m/s.
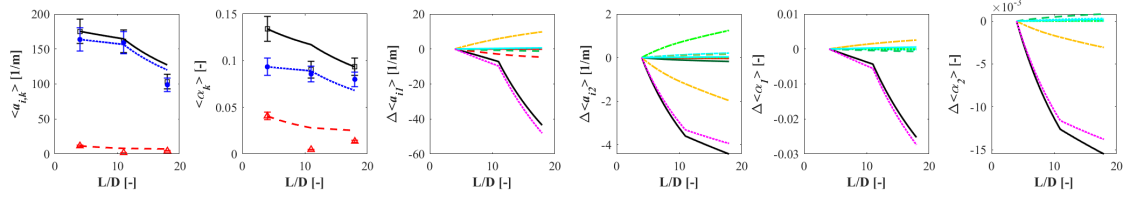
Pipe diameter:152.4 mm; $\langle j_f \rangle$: 1.00 m/s; $\langle j_{g,0} \rangle$: 0.15 m/s.
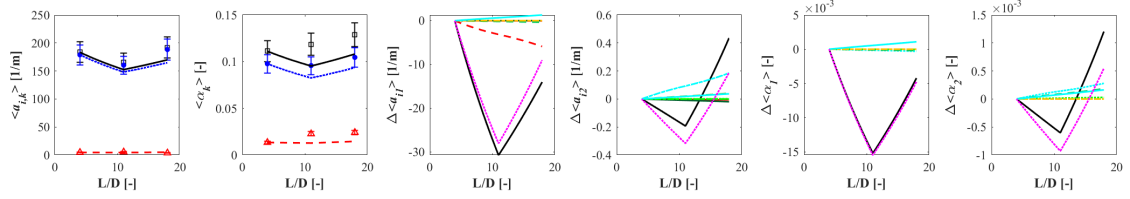
Pipe diameter:152.4 mm; $\langle j_f \rangle$: 1.00 m/s; $\langle j_{g,0} \rangle$: 0.30 m/s.
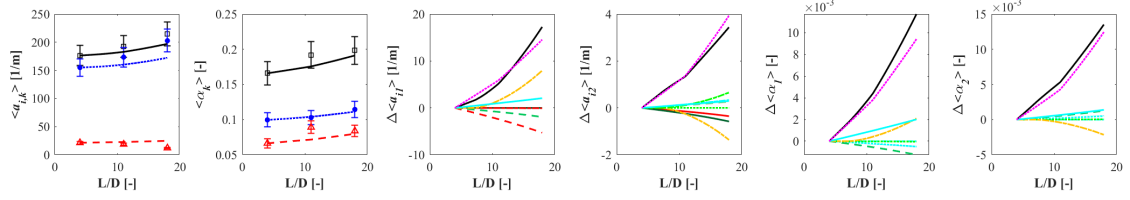
Pipe diameter:152.4 mm; $\langle j_f \rangle$: 0.05 m/s; $\langle j_{g,0} \rangle$: 1.00 m/s.

164
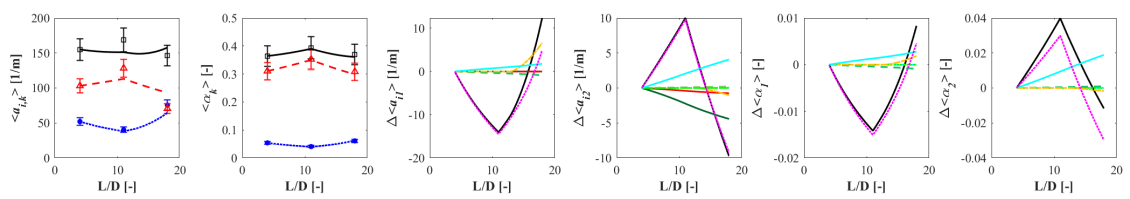
Pipe diameter:152.4 mm; $\langle j_f \rangle : 0.30$ m/s; $\langle j_{g,0} \rangle : 1.00$ m/s.
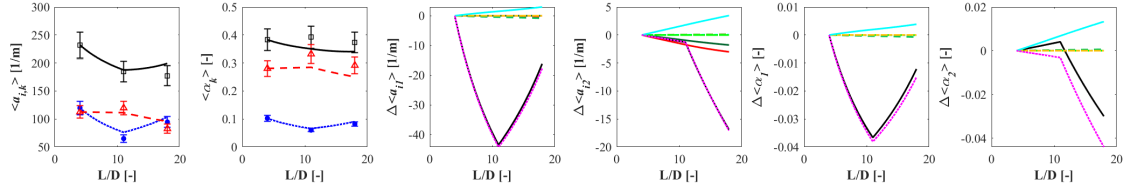
Pipe diameter:152.4 mm; $\langle j_f \rangle : 1.00$ m/s; $\langle j_{g,0} \rangle : 1.00$ m/s.
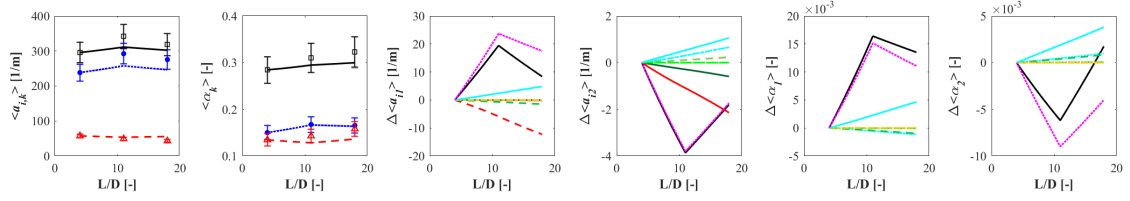
Pipe diameter:203.2 mm; $\langle j_f \rangle$: 0.24 m/s; $\langle j_{g,0} \rangle$: 0.15 m/s.
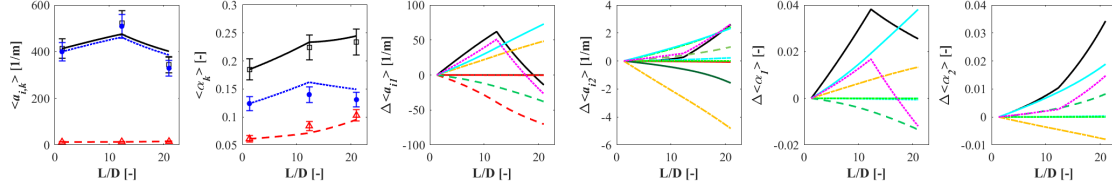
Pipe diameter:203.2 mm; $\langle j_f \rangle$: 0.23 m/s; $\langle j_{g,0} \rangle$: 0.54 m/s.
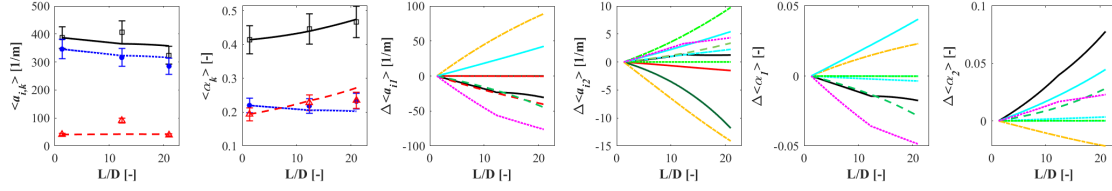
Pipe diameter:203.2 mm; $\langle j_f \rangle$: 0.31 m/s; $\langle j_{g,0} \rangle$: 1.39 m/s.
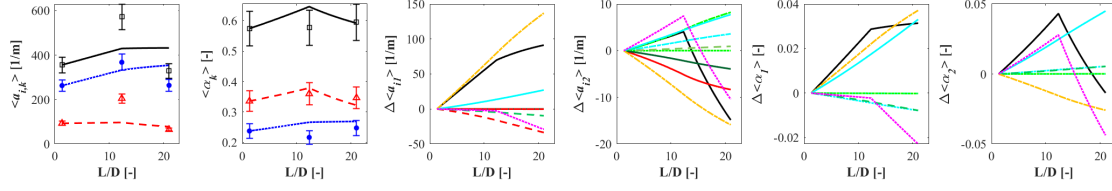

Pipe diameter:203.2 mm; $\langle j_f \rangle$: 0.29 m/s; $\langle j_{g,0} \rangle$: 3.82 m/s.
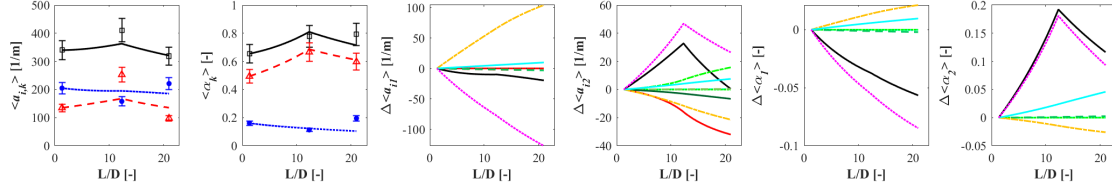
Pipe diameter:203.2 mm; $\langle j_f \rangle$: 0.44 m/s; $\langle j_{g,0} \rangle$: 0.21 m/s.
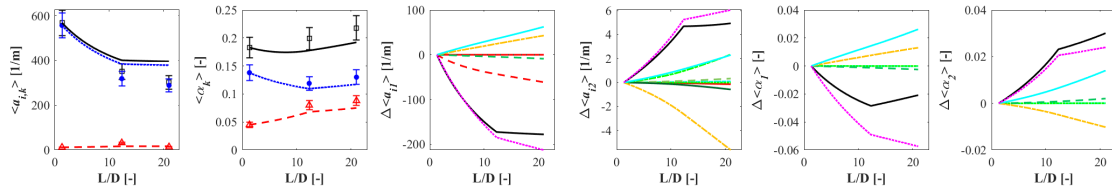
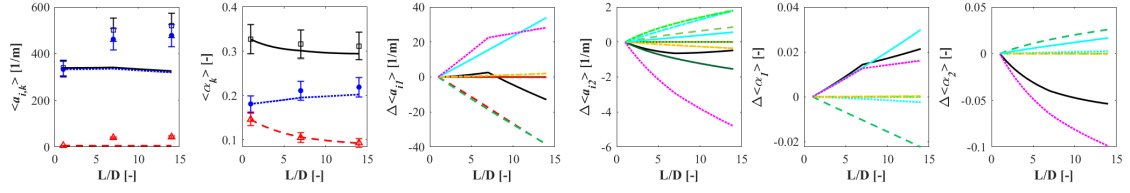Pipe diameter:203.2 mm; $\langle j_f \rangle$: 0.42 m/s; $\langle j_{g,0} \rangle$: 0.67 m/s.
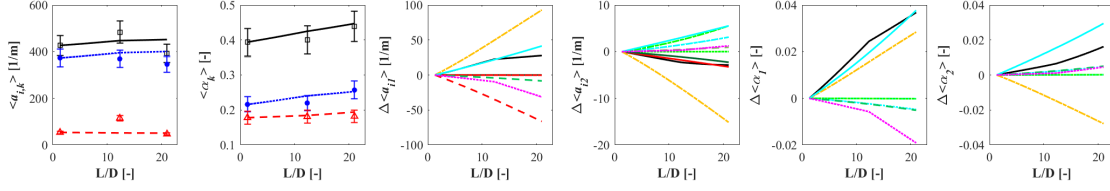
Pipe diameter:203.2 mm; $\langle j_f \rangle$: 0.45 m/s; $\langle j_{g,0} \rangle$: 2.14 m/s.
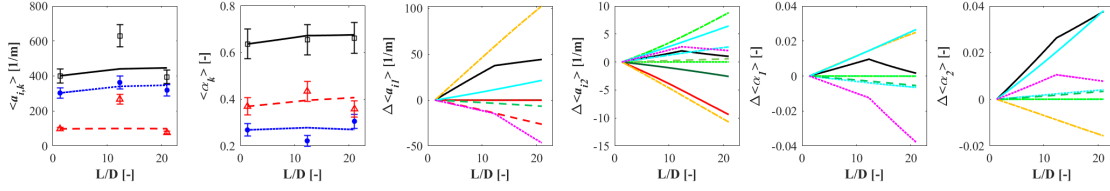
Pipe diameter:203.2 mm; $\langle j_f \rangle$: 0.46 m/s; $\langle j_{g,0} \rangle$: 3.50 m/s.
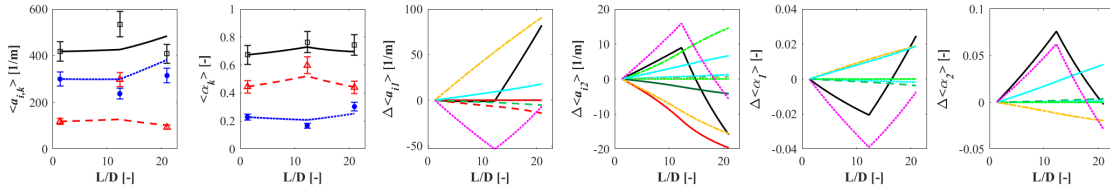
Pipe diameter:203.2 mm; $\langle j_f \rangle$: 0.93 m/s; $\langle j_{g,0} \rangle$: 0.35 m/s.
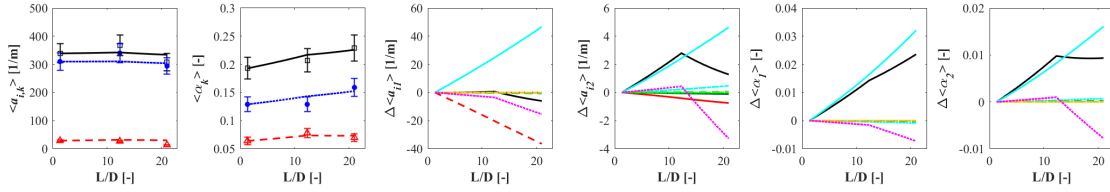
Pipe diameter:203.2 mm; $\langle j_f \rangle$: 0.88 m/s; $\langle j_{g,0} \rangle$: 1.34 m/s.

Pipe diameter:203.2 mm; $\langle j_f \rangle$: 0.93 m/s; $\langle j_{g,0} \rangle$: 2.90 m/s.
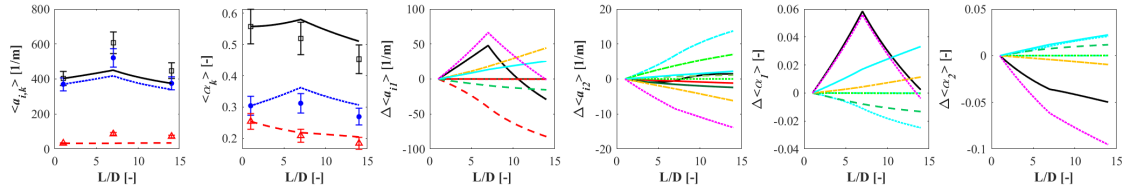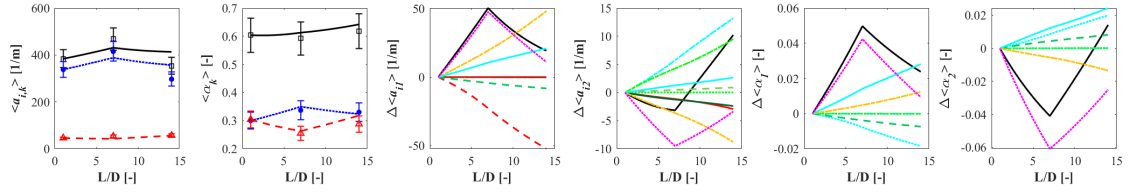
Pipe diameter:304.8 mm; $\langle j_f \rangle$: 0.23 m/s; $\langle j_{g,0} \rangle$: 0.39 m/s.
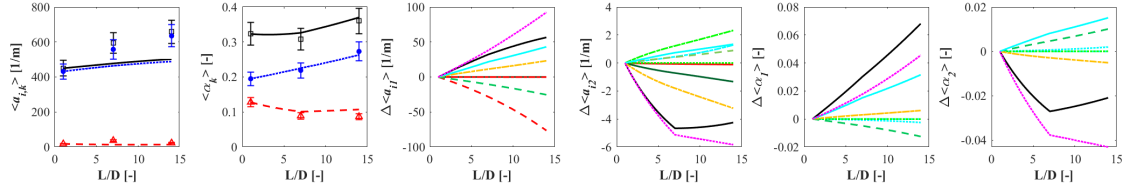
Pipe diameter:304.8 mm; $\langle j_f \rangle$: 0.24 m/s; $\langle j_{g,0} \rangle$: 0.91 m/s.
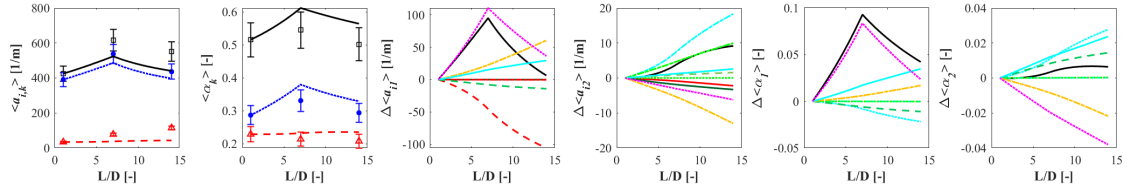
Pipe diameter:304.8 mm; $\langle j_f \rangle$: 0.20 m/s; $\langle j_{g,0} \rangle$: 1.62 m/s.
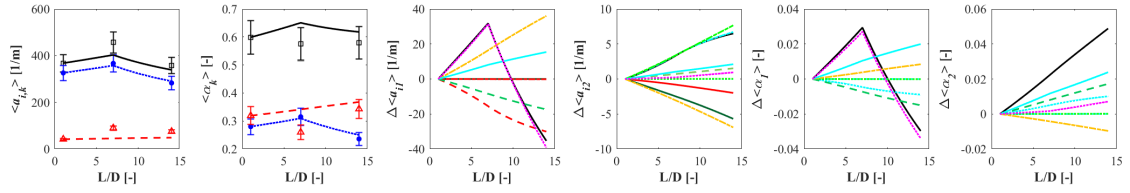
Pipe diameter:304.8 mm; $\langle j_f \rangle$: 0.27 m/s; $\langle j_{g,0} \rangle$: 2.10 m/s.
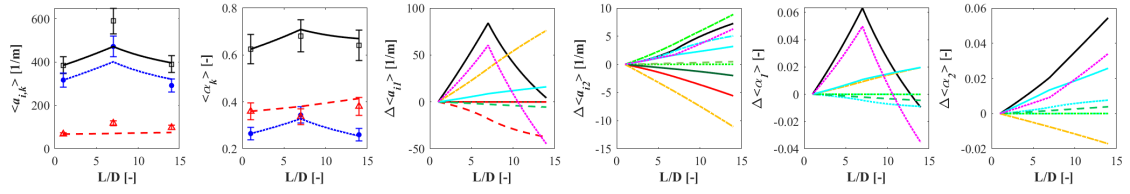
Pipe diameter:304.8 mm; $\langle j_f \rangle$: 0.30 m/s; $\langle j_{g,0} \rangle$: 0.17 m/s.

169
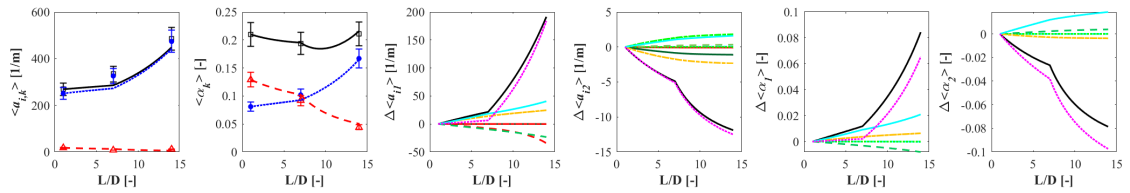
Pipe diameter:304.8 mm; $\langle j_f \rangle$: 0.33 m/s; $\langle j_{g,0} \rangle$: 0.41 m/s.

Pipe diameter:304.8 mm; $\langle j_f \rangle$: 0.36 m/s; $\langle j_{g,0} \rangle$: 0.68 m/s.
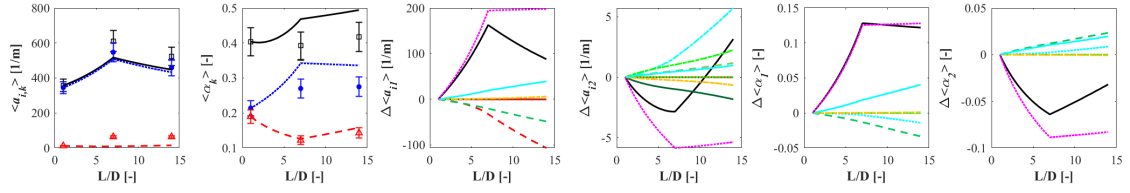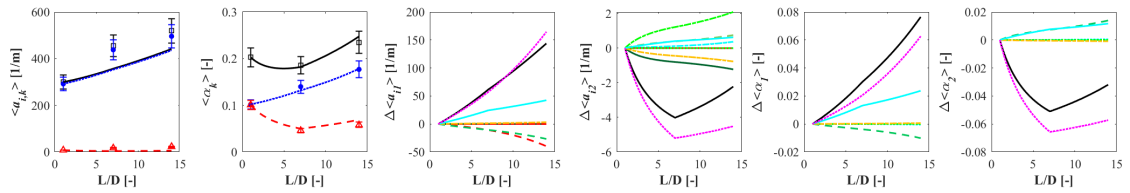
Pipe diameter:304.8 mm; $\langle j_f \rangle$: 0.32 m/s; $\langle j_{g,0} \rangle$: 1.11 m/s.
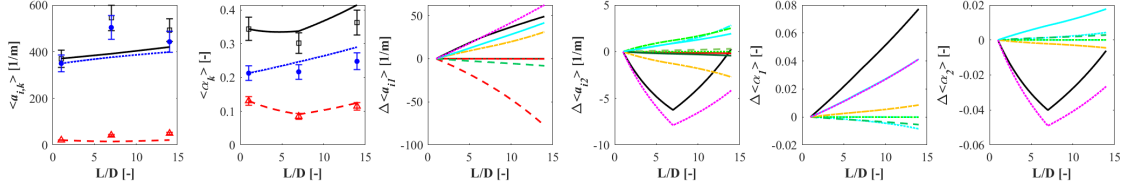
Pipe diameter:304.8 mm; $\langle j_f \rangle$: 0.33 m/s; $\langle j_{g,0} \rangle$: 1.53 m/s.
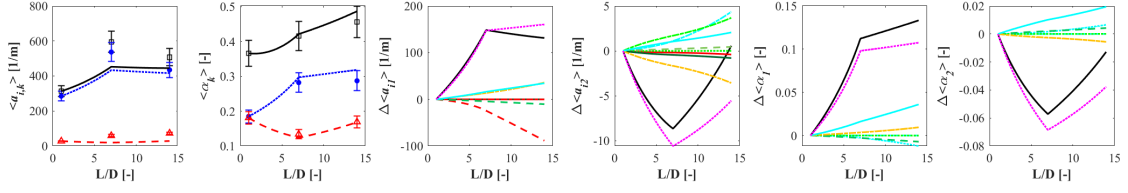
Pipe diameter:304.8 mm; $\langle j_f \rangle$: 0.47 m/s; $\langle j_{g,0} \rangle$: 0.24 m/s.
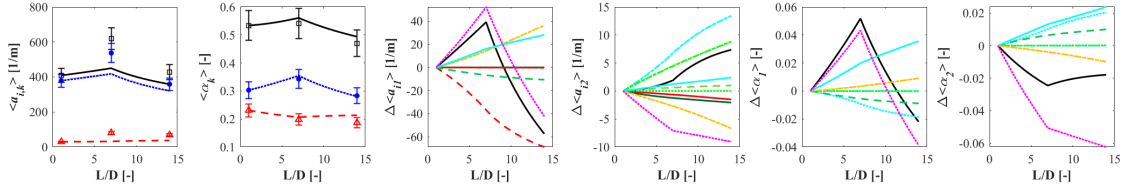

170

Pipe diameter:304.8 mm; $\langle j_f \rangle$: 0.48 m/s; $\langle j_{g,0} \rangle$: 0.48 m/s.
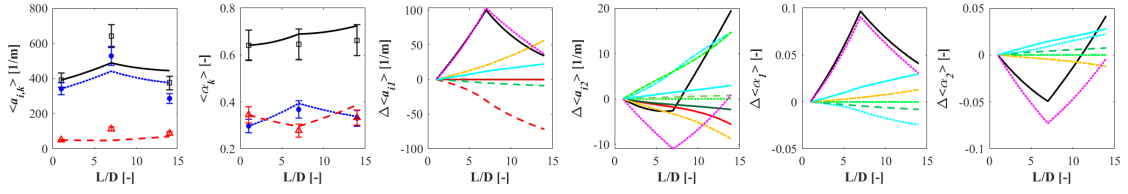
Pipe diameter:304.8 mm; $\langle j_f \rangle$: 0.46 m/s; $\langle j_{g,0} \rangle$: 0.82 m/s.

Pipe diameter:304.8 mm; $\langle j_f \rangle$: 0.46 m/s; $\langle j_{g,0} \rangle$: 1.24 m/s.

Pipe diameter:304.8 mm; $\langle j_f \rangle$: 0.46 m/s; $\langle j_{g,0} \rangle$: 2.10 m/s.

171

VITA

Zhuoran Dang was born and grew up in Fuxin, China on Janunary 15, 1992. He is the only child of Mr. Zili Dang and Mrs. Xiaodong Zhang. After graduating from Fuxin Senior High School in 2010, he went to Zhejiang University for undergraduate study. In 2014, Zhuoran obtained his bachelor degree in Energy and Environment Engineering. Then he come to the United States and began his graduate study and research work at the Thermal Hydraulics and Reactor Safety Laboratory, Purdue University under the guidance of Distinguished Professor Mamoru Ishii. During this period, he involved in several two-phase flow projects, and his thesis topic focused on the development of interfacial area transport models. He was granted a Master's degree in Nuclear Engineering in May 2016, and a Ph.D in Nuclear Engineering in August 2021. During his graduate work, he was awarded the Bilsland dissertation fellowship.